Master's thesis

NTNU
Norwegian University of Science and Technology
Faculty of Natural Sciences
Department of Physics

Edwin Nongba Traore

Characterization of BTO thin films by electron diffraction techniques

Master's thesis in Applied Physics and Mathematics
Supervisor: Randi Holmestad
June 2019

NTNU
Norwegian University of
Science and Technology

Edwin Nongba Traore

Characterization of BTO thin films by electron diffraction techniques

Master's thesis in Applied Physics and Mathematics
Supervisor: Randi Holmestad
June 2019

Norwegian University of Science and Technology
Faculty of Natural Sciences
Department of Physics

NTNU
Norwegian University of
Science and Technology

Preface

This thesis is the conclusion of my MSc in Applied Physics at the Department of Physics of the Norwegian University of Science and Technology (NTNU), Trondheim. The thesis is a result of the collaboration between the Department of Materials Science and Engineering and the Department of Physics at NTNU. The experimental work was carried out at the Department of Physics with Prof. Randi Holmestad, Senior Engineer Ragnhild Sæterli and PhD candidate Inger-Emma Nylund as supervisors.

I would like to thank Randi, Ragnhild and Inger-Emma for their invaluable advice, feedback and encouragement. I would also like to thank Assoc. Prof. Per Erik Vullum for help with FIB specimen preparation and valuable discussions. Furthermore, I would like to thank Senior Engineer Bjørn Soleim for keeping the TEM operational. PhD candidate Kristine Bakken and her research group at the Department of Materials Science and Engineering have my gratitude both for providing the films and for giving valuable insight into their synthesis, properties and structure. Thanks go to PhD Yu-Tsun Shao and PhD Haw-Wen Hsiao from the University of Illinois, Urbana-Champaign for providing the alignment procedure to the diffraction techniques used. Thanks go to Bertrand Schaffer for generously providing a free copy of his scripting ebook. I would also like to thank the TEM group as a whole for providing a friendly and stimulating environment. Finally, I would like to thank my family and friends for love and support.

Trondheim, June 2019

Edwin Nongba Traore

Abstract

Ferroelectric barium titanate (BTO) thin films produced by aqueous chemical solution deposition on strontium titanate (STO) substrates have recently been shown to exhibit an increased in-plane polarization. A domain structure with predominantly in-plane polarization was proposed to account for the observations.

Scanning convergent electron beam diffraction (SCBED) is a novel technique that combines CBED patterns with quantitative data processing. Previous work has shown that the polarization of single crystal BTO can be determined by quantifying the symmetry of CBED patterns. The aim of this thesis was to determine the domain structure of BTO thin films by selected area electron diffraction (SAED) and SCBED.

Two BTO thin films were studied in a transmission electron microscope (TEM). The films were synthesized using a non-toxic aqueous solution for chemical deposition on (100) oriented STO substrates. The films were thermally annealed at 700°C and 1000°C. A focused ion beam was used for preparation of cross-sectional TEM specimens.

The film annealed at 700 °C exhibited polycrystalline growth, and the film annealed at 1000°C exhibited epitaxial growth. By SAED it was shown that the epitaxial thin film consists of multiple domains with small variations in lattice parameter and orientation. The symmetry of CBED patterns was found to not correlate with polarization, due to other sources of asymmetry in the film.

An algorithm using edge-detection and template matching was developed to measure lattice parameters from inter-disc distances in CBED patterns. The algorithm determined the lattice parameter of the single crystal STO substrate with approximately ± 1.5 pm precision, and the lattice parameter of the epitaxial film with approximately ± 3 pm precision. The precision of the algorithm in the epitaxial film was not sufficient to determine the domain structure. The lattice parameters of the domains in the epitaxial film were measured to vary in between the nominal a and c lattice parameters of bulk tetragonal BTO.

Sammendrag

Ferroelektriske tynnfilmer av bariumtitanat (BTO) produsert ved kjemisk løsningsavsetning på substrater av strontiumtitanat (STO) har vist en forbedret polarisasjon i planet til film-substrat grenseflaten. En domenestruktur med overveiende polarisasjon i planet ble foreslått som forklaring på observasjonen.

Skanning-konvergent-elektronstråle-diffraksjon (SCBED) er en ny teknikk der CBED-mønster analyseres ved hjelp av data-prosessering. Tidligere arbeid har vist at polarisasjonen i BTO kan bestemmes utifra symmetrien i CBED-mønster. Målsetningen til dette arbeidet var å bestemme domenestrukturen i BTO tynnfilmer ved begrenset-område elektron-diffraksjon (SAED) og SCBED.

To BTO tynnfilmer ble undersøkt i et transmisjonselektronmikroskop (TEM). Filmene ble laget ved ikke-toksisk kjemisk løsningsavsetning på (100) orientert STO substrat. Filmene ble termisk annealet ved henholdsvis 700°C og 1000°C. En fokusert ionstråle ble brukt for å prepare TEM-prøver.

Filmen annealet ved 700°C viste polykrystallinsk vekst, og filmen annealet ved 1000°C viste epitaksiell vekst. Ved SAED ble det funnet at den epitaksielle filmen består av flere domener med forskjellige gitterparametere og orienteringer. Symmetrien i CBED-mønster ble funnet å ikke korrelere med polarisasjon, da det fantes for mange forstyrrende elementer i filmen.

En algoritme basert på kantdeteksjon ble utviklet for å måle gitterparameteren ut i fra avstander mellom disker i CBED-mønster. Algoritmen bestemte gitterparameterene i det enkrystallinske STO substratet med opptil ± 1.5 pm presisjon, og gitterparameterene i BTO tynnfilmen med opptil ± 3 pm presisjon. Algoritmens presision var ikke tilstrekkelig til å kunne trekke defintive slutninger om domenestrukturen til tynnfilmen. Ved SAED- og CBED-målinger ble gitterparameterene i den epitaksielle filmen funnet til å variere mellom de nominelle verdiene til a og c gitterparamterene i tetragonalt BTO.

Abbreviations

BF **B**right **F**ield

BTO **B**arium **T**itanate - **B**a**T**i**O**$_3$

CBED **C**onvergent **B**eam **E**lectron **D**iffraction

CSD **C**hemical **S**olution **D**eposition

DF **D**ark **F**ield

DM **D**igital **M**icrograph

DP **D**iffraction **P**attern

FEG **F**ield **E**mission **G**un

FIB **F**ocused **I**on **B**eam

HAADF-STEM **H**igh-**A**ngle **A**nnular **D**ark-**F**ield **S**canning **TEM**

OL **O**bjective **L**ens

SADP **S**elected **A**rea **D**iffraction **P**attern

SAED **S**elected **A**rea **E**lectron **D**iffraction

SCBED **S**canning **C**onvergent **B**eam **E**lectron **D**iffraction

SEM **S**canning **E**lectron **M**icroscope/y

STO **S**trontium **T**itanate - **S**r**T**i**O**$_3$

TEM **T**ransmission **E**lectron **M**icroscope/y

ZA **Z**one **A**xis

Contents

Preface i

Abstract iii

Sammendrag v

Abbreviations vi

1 Introduction 1

2 Theory 3
2.1 Crystallography . . . 3
2.1.1 Bravais lattices and unit cells . . . 3
2.1.2 The Reciprocal Lattice . . . 4
2.1.3 Directions and Planes . . . 4
2.1.4 Lattice Systems . . . 5
2.1.5 Dislocations . . . 5
2.2 Diffraction in Crystals . . . 7
2.2.1 Laue Diffraction and the Ewald Sphere . . . 7
2.2.2 Kinematic Theory of Diffraction . . . 9
2.2.3 Dynamical Theory of Diffraction . . . 9
2.3 Transmission Electron Microscopy . . . 11
2.3.1 TEM Operation Modes . . . 11
2.3.2 Convergent Beam Electron Diffraction . . . 14
2.3.3 Symmetry and the Breakdown of Friedel's Law . . . 15
2.4 Material . . . 16
2.4.1 Strontium Titanate . . . 16
2.4.2 Barium Titanite . . . 16
2.4.3 Strain Engineering Ferroelectric Thin Films . . . 17
2.4.4 Domain Formation in Ferroelectric Thin Films . . . 18
2.4.5 Previous Study of the Material System . . . 21
2.5 Image Processing . . . 22
2.5.1 Canny Edge Detection . . . 22
2.5.2 Image Metrics . . . 23
2.5.3 Cross-Correlation and Template Matching . . . 25

3 Method 27
3.1 Thin Film Synthesis . . . 27
3.2 Focused Ion Beam TEM Specimen Preparation . . . 28
3.3 CBED Simulations . . . 29
3.4 TEM Operation Modes . . . 29
3.4.1 Selected Area Electron Diffraction . . . 30
3.4.2 Scanning Convergent Beam Electron Diffraction . . . 31
3.5 Data Processing . . . 32
3.5.1 Symmetry Quantification Program . . . 32
3.5.2 Lattice Parameter Measurement . . . 34
3.5.3 Lattice Parameter Measurement by Algorithm . . . 35

4 Results **37**
4.1 Bright Field Images . . . 37
4.1.1 Polycrystalline Specimen . . . 37
4.1.2 Epitaxial Specimen . . . 38
4.2 Selected Area Diffraction Patterns . . . 40
4.3 Evaluation of Symmetry Quantification . . . 42
4.4 Simulated CBED . . . 43
4.4.1 Effect of Beam Misalignment on CBED . . . 46
4.5 CBED from the BTO Film . . . 49
4.6 SCBED from the STO Substrate . . . 50
4.6.1 Symmetry Maps . . . 50
4.6.2 Lattice Parameter Maps . . . 52
4.7 SCBED from the BTO Film . . . 53
4.7.1 Symmetry Maps . . . 53
4.7.2 Lattice Parameter Maps . . . 55

5 Discussion **61**
5.1 Microstructure . . . 61
5.1.1 Bright Field Images . . . 61
5.1.2 Selected Area Diffraction Patterns . . . 61
5.1.3 Convergent Beam Electron Diffraction . . . 62
5.1.4 Domain Structure . . . 63
5.2 Data Acquisition and Processing . . . 64
5.2.1 Quality of Symmetry Quantification . . . 64
5.2.2 Quality of SCBED Acquisition . . . 64
5.2.3 Quality of Manual Measurements . . . 65
5.2.4 Quality of Measurements by Algorithm . . . 67

6 Conclusion **69**

7 Further Work **71**

References **73**

A Additional SCBED Data **79**

B Digital Micrograph Scripts **91**

1 Introduction

The piezoelectric effect was first discovered in 1880 by the French brothers Pierre and Jacques Curie, and describes the phenomena where electric charge accumulates in a material in response to applied mechanical stress [1]. In 1921 it was discovered that a subgroup of piezoelectric materials exhibit spontaneous electric polarization that can be reversed by the application of an external field [2]. The subgroup of piezoelectrics exhibiting such properties is known as ferroelectrics.

From their discovery to the present day, ferroelectric materials underwent a transformation from academic curiosities to objects of industrial interest [3]. As of writing, considerable research is focused on the development of ferroelectric thin films, due to their promising applications in areas such as micro-sensors, electro-optic modulation and solid-state memory [4][5][6].

Barium titanate (BTO) is a ferroelectric that is widely used in capacitors due to its high dielectric constant. Chemical solution deposition (CSD) offers an attractive way of producing BTO thin films due to its relatively low cost and ease of fabrication [7][8].

BTO thin films on (001) strontium titanate (STO) substrates have been produced by CSD at the Department of Material Science and Engineering, NTNU, by Phd Candidate Kristine Bakken. In the fabrication process organic solvents, which are generally irritant or toxic, have been replaced by water. This results in a more benign and cost effective way of fabrication. Previous work on the thin films fabricated by this method show an increased Curie temperature, an enhanced in-plane lattice parameter and enhanced in-plane polarization [9]. It was proposed that these changes were caused by thermal strain due to a mismatch in the thermal expansion coefficient of substrate and film, favoring a domain structure with predominantly in-plane polarization [9].

Modern transmission electron microscopes (TEM) offer the possibility of studying materials at a nanoscale resolution. By use of electron diffraction techniques, highly accurate determination of lattice parameters in crystalline structures are possible. With convergent beam electron diffraction (CBED) it is possible to distinguish between centrosymmetric and non-centrosymmetric unit cells in materials [10]. Previous work has shown that it is possible to distinguish between different domains with different polarization directions in single crystal BTO using a scanning CBED (SCBED) setup [11][12][13].

The first aim of this thesis is to study the microstructure of chemical solution deposited BTO thin films by TEM in order to determine polarization direction and domain structure. The second aim of this thesis is to test the feasibility of the SCBED technique for determining domain structures.

A theoretical background covering crystallography, diffraction, electron microscopy, properties of BTO thin films and image processing is provided in section 2. The experimental procedures of the thin film synthesis, specimen preparation, simulations, TEM operation modes and data processing are detailed in section 3. The results are presented in section 4, followed by a discussion of the results and methods in section 5. Finally, section 6 and 7 offer a conclusion and a proposal for further work.

2 Theory

The physics underlying ferroelectric thin films and transmission electron microscopy (TEM) is advanced and extensive. This section offers an introduction into the fundamental theory on which this thesis is based. First, section 2.1 presents central concepts of crystallography, followed by an introduction to diffraction from crystals in section 2.2. Section 2.3 presents the basic theory and practical applications of the TEM. Section 2.4 presents the structure and functional properties of BTO thin films. Finally, section 2.5 presents image processing techniques.

2.1 Crystallography

The following sections offer a brief introduction to basic concepts in crystallography based on Schwarzenbach [14].

2.1.1 Bravais lattices and unit cells

Solid materials are classified by the way the constituent atoms are arranged in space. If there is no long-range structure, the material is called amorphous. If the atoms are arranged in a highly ordered structure, the material is called crystalline.

A crystal is defined as a periodic structure in space. It is a geometric concept, and can thus be considered without reference to a physical structure. When describing crystals the concept of a Bravais lattice is useful. A Bravais lattice has the property that every point in the lattice has identical surroundings. From this it follows that there is a discrete translational symmetry in the crystal, as translation to another lattice point does not change the surrounding lattice. The translational symmetry operations of the lattice are described by translation through the lattice vector

$$\vec{R}_{n_1 n_2 n_3} = n_1 \cdot \vec{a}_1 + n_2 \cdot \vec{a}_2 + n_3 \cdot \vec{a}_3 \tag{1}$$

where n_1, n_2 and n_3 are integers and $\vec{a}_1$,$\vec{a}_2$ and $\vec{a}_3$ are termed the primitive vectors of the lattice.

The unit cell is a volume that can reproduce the whole lattice through translation. The smallest possible unit cell, containing one lattice point, is termed a primitive unit cell. Figure 1 shows a general unit cell. The atoms that lie in the primitive unit cell of a crystal are termed the basis of the unit cell. The position of atoms with respect to a lattice point is described by the basis coordinate vector $r_j = x_j \cdot \vec{a}_1 + y_j \cdot \vec{a}_2 + z_j \cdot \vec{a}_3$ where $0 \leq x_j, y_j, z_j < 1$. Every atom in a crystal is reached by $\vec{r}$, a combination of the lattice and basis vector $\vec{r} = \vec{R}_{n_1 n_2 n_3} + \vec{r}_j$.

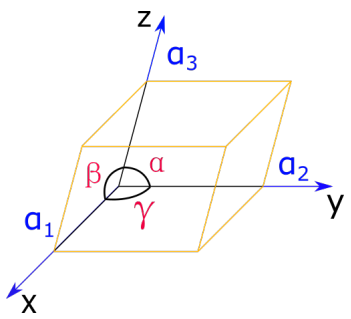

Figure 1: A general unit cell. Figure appropriated from Schwarzenbach [14].

2.1.2 The Reciprocal Lattice

The Fourier transform of a Bravais lattice produces a new lattice, called the reciprocal lattice. The basis of the reciprocal lattice vector is given as

$$\vec{b_1} = 2\pi \frac{\vec{a_2} \times \vec{a_3}}{a_1(\vec{a_2} \times \vec{a_3})} \quad \vec{b_2} = 2\pi \frac{\vec{a_3} \times \vec{a_1}}{\vec{a_2}(\vec{a_3} \times \vec{a_1})} \quad \vec{b_3} = 2\pi \frac{\vec{a_1} \times \vec{a_2}}{\vec{a_3}(\vec{a_1} \times \vec{a_2})} \tag{2}$$

where $\vec{a}_1$,$\vec{a}_2$ and $\vec{a}_3$ are the basis vectors of the Bravais lattice. The reciprocal lattice vector is given as

$$\vec{g}_{hkl} = h \cdot \vec{b}_1 + k \cdot \vec{b}_2 + l \cdot \vec{b}_3 \tag{3}$$

where h, k and l are integers. The concept of the reciprocal lattice is vital to understand diffraction, as will be made clear in later sections.

2.1.3 Directions and Planes

When examining a crystal structure it is often of interest to do this along a high symmetry axis of the crystal. Directions in the crystal are expressed as parallel to the reciprocal lattice vector $\vec{g}_{hkl}$ given in equation 3, where h, k and l are termed Miller indices. In the notation (hkl), Miller indices describe the atomic planes orthogonal to $\vec{g}_{hkl}$. The values of the individual indices are given by the reciprocal of the intersection of the plane and the axes of the unit cell paralellpiped. If the indices have negative values this is denoted by a bar over the index. A set of equal planes is denoted $\{hkl\}$, while a set of equal directions is denoted as $\langle hkl \rangle$. Figure 2 shows an example of a plane and its corresponding Miller indices.

If a given $\vec{R}_{n_1 n_2 n_3}$ lies normal to a plane containing several $\vec{g}_{hkl}$ then

$$\vec{g}_{hkl} \cdot \vec{R}_{n_1 n_2 n_3} = 0 \tag{4}$$

for these $\vec{g}_{hkl}$, and $[n_1 n_2 n_3]$ is termed a zone axis (ZA).

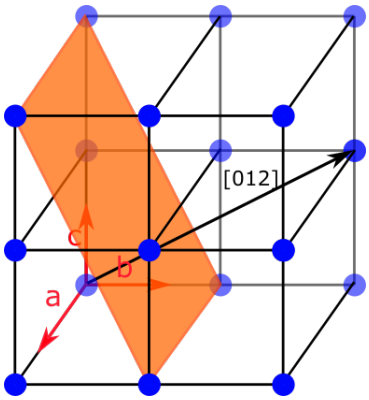

Figure 2: Crystal with highlighted [012] plane and corresponding normal.

2.1.4 Lattice Systems

If two Bravais lattices have isomorphic symmetry groups, the lattices themselves can be considered isomorphic. This reduces the number of distinct Bravais lattices to fourteen in three dimensions. The Bravais lattices can further be divided into seven crystal systems according to their symmetries. In Table 1 the seven crystal systems are presented. The symmetry elements are written in Hermann-Maguine notation [14].

In addition to placing atoms in the corners of the unit cells, it is for some crystal systems possible to place lattice points in the middle or on the faces of the unit cell. This further divides the crystal systems into simple/primitive (P), base-centered (C), body-centered (I) and face-centered (F) lattices. Combining the aforementioned symmetry operations with the possible lattices there are 230 distinct space groups, covering all possible crystalline patterns in three dimensions.

Table 1: The seven crystal systems and the constraints on their cell constants and cell angles. The symmetry elements are written in Hermann-Maguine notation. Table appropriated from Schwarzenbach [14].

Restrictions for:	Cell constants	Cell angles	Maximum Symmetry
triclinic	none	none	$\bar{1}$
monoclinic	none	$\alpha = \gamma = 90$	$2/m$
orthorombic	none	$\alpha = \beta = \gamma = 90$	mmm
tetragonal	$a_1 = a_2$	$\alpha = \beta = \gamma = 90$	$4/mmm$
trigonal	$a_1 = a_2$	$\alpha = \beta = 90, \gamma = 120$	$\bar{3}m$
hexagonal	$a_1 = a_2$	$\alpha = \beta = 90, \gamma = 120$	$6/mmm$
cubic	$a_1 = a_2 = a_3$	$\alpha = \beta = \gamma = 90$	$m\bar{3}m$

2.1.5 Dislocations

The model of a crystal with perfect periodicity can explain some properties of crystalline materials. However, irregularities in the crystal structure have a significant influence in determining the physical properties of a material [15]. Dislocations are an important class of crystal irregularities. When an extra half-plane is present in the crystal lattice, it causes deformation and strain for the surrounding atoms. This is called an edge dislocation. The other fundamental type of dislocation is called a screw dislocation. The two types of dislocations are visualized together in Figure 3. If one traces a square in the lattice around the dislocation, the end position will be different from the start position. The vector from start to finish is termed the Burgers vector of the dislocation. Pure edge and screw dislocations are useful as theoretical tools for understanding. However, real dislocations are usually a mix of the two, and their Burgers vectors the sum of the composites [16].

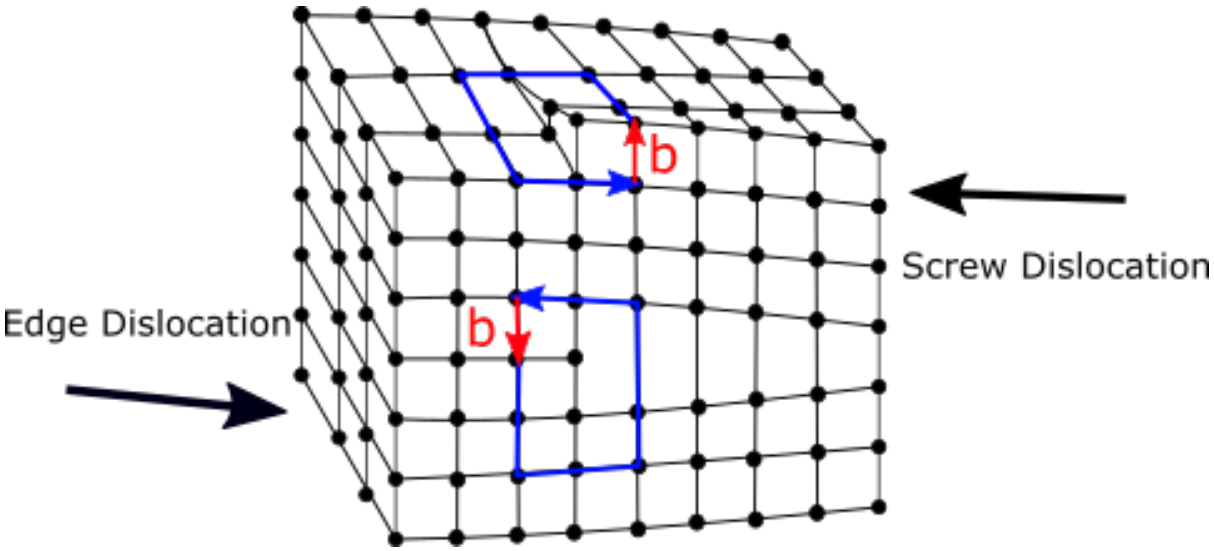

Figure 3: Edge and Screw dislocations in a matrix. The upper dislocation has a Burgers vector perpendicular to the blue plane, and is therefore a screw dislocation. The lower dislocation has a Burgers vector in the plane of the blue loop and is therefore an edge dislocation. Figure based on Callister [16].

2.2 Diffraction in Crystals

Diffraction refers to the various phenomena that occur when waves scatter from obstacles. Theories describing the diffraction of fast electron from crystals can be divided into two categories. Kinematical theory assumes no absorption, refraction and that each electron scatters only once, whereas the more accurate dynamical theories take into account the possibility of multiple scattering events per electron. The kinematical theory is approximately valid when describing the geometry of electron diffraction patterns, but is generally not valid in describing the intensities of the diffracted beams. This section will first introduce the Laue/Bragg conditions for scattering of waves from crystals, followed by the kinematical theory to describe the geometry of electron diffraction patterns. Finally a dynamical theory for accurate calculation of scattering intensities is presented.

2.2.1 Laue Diffraction and the Ewald Sphere

When a wave is incident upon a periodic lattice and scatters, the interference between the lattice sites causes the intensity of the scattered wave to interfere constructively at some scattering angles. The condition for constructive elastic scattering is given by Braggs law

$$2d_{hkl}\sin(\theta) = n\lambda \tag{5}$$

where d_{hkl} is the distance between two lattice planes of the structure, θ is the scattering angle, n is an integer and λ is the wavelength of the electron. A more general formulation is called the Laue condition for diffraction and is given in reciprocal space as

$$\vec{Q} = \vec{k_f} - \vec{k_i} = \vec{g}_{hkl} \tag{6}$$

where $\vec{k_i}$ is the momentum of the incident electron, $\vec{k_f}$ is the momentum of the scattered electron and $\vec{g}_{hkl}$ is a reciprocal lattice vector. A useful construct for finding which reciprocal lattice vectors satisfy the Laue condition is the Ewald sphere. A schematic of the Ewald sphere is shown in Figure 4. The Ewald sphere has a radius equal to the magnitude of the wave-vector of the incident electrons $|\vec{k_i}|$. Wherever the sphere intersects a lattice point the Laue-condition is satisfied, and the family of lattice planes corresponding to the reciprocal lattice vector $\vec{g}_{hkl} = \vec{Q}$ will diffract constructively, producing a diffraction pattern (DP) [14]. The diffraction pattern can be analyzed to determine which zone-axis of the crystal the beam is incident on, and what length the inter-plane distances d_{hkl} are. The radius of the Ewald sphere is large for fast electrons with large momenta, and the sphere therefore intersects many lattice points. The reciprocal lattice points of real crystal volumes are also extended due to the finite size of the crystals. The elongation in reciprocal space is largest in the direction in which the crystal is smallest in real space. The reciprocal lattice points of thin TEM specimens are therefore elongated and called rel-rods [17]. The elongation of the lattice points is shown in Figure 4.

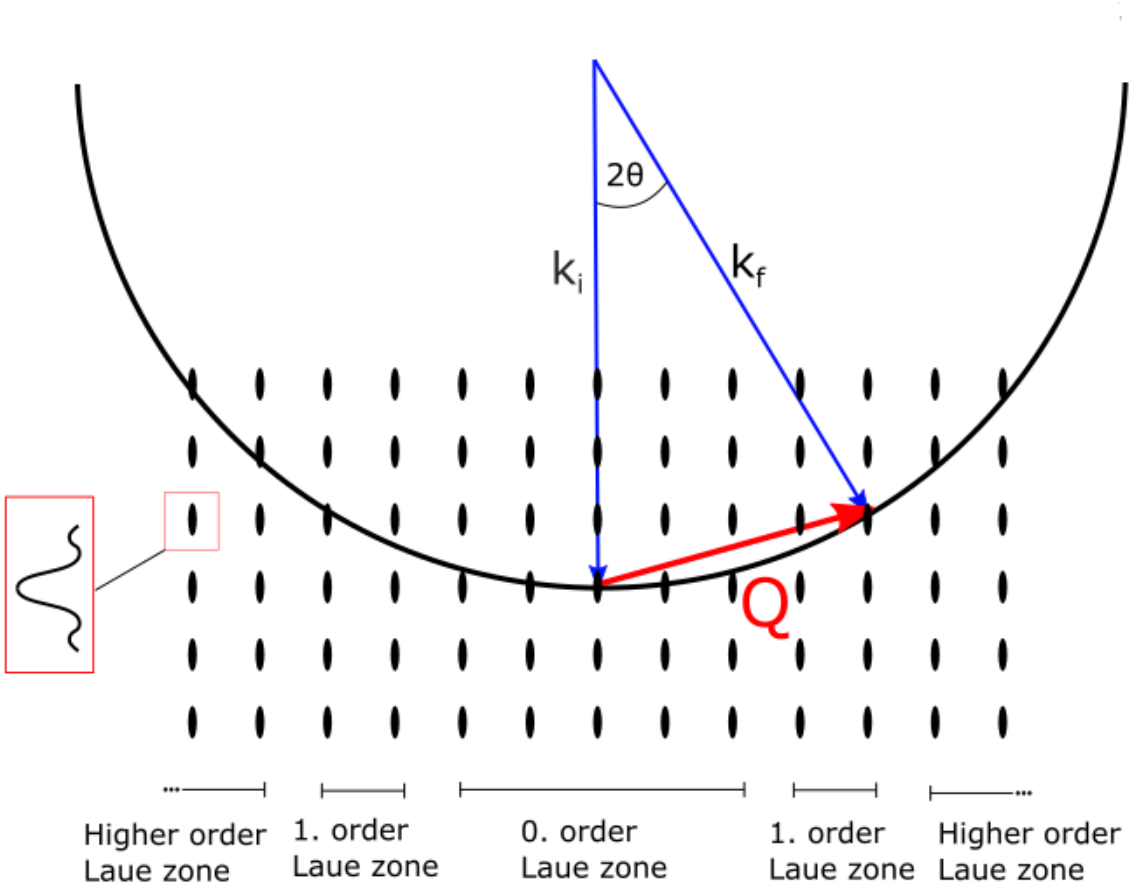

Figure 4: The schematic of the Ewald construction in reciprocal space. Wherever the sphere intersects a point the Laue diffraction condition is met. The reflections are divided into Laue zones by which row of reciprocal lattice points they originate from. The reciprocal lattice points are extended in space due to the finite dimensions of the crystal. Figure appropriated from Williams and Carter [17].

2.2.2 Kinematic Theory of Diffraction

Assuming that scattering of the wave with the specimen is weak, the amplitude of the incident wave can be approximated as constant throughout the specimen volume. This is known as the first order Born approximation [18]. Assuming additionally that absorption and refraction can be neglected, it can be shown that

$$\psi_s(\vec{q}) \propto \mathscr{F}(V(\vec{r})) \tag{7}$$

where $\psi_s(\vec{q})$ is the scattered wave corresponding to the scattering vector $\vec{q}$, and $\mathscr{F}(V(\vec{r}))$ is the Fourier transform of the specimen potential. In electron diffraction the total crystal potential $V(\vec{r})$ is used because the beam electrons interact strongly with both the nucleus and the electrons of the crystal. In a crystal the potential $V(\vec{r})$can be expressed as the convolution of the crystal basis with the Bravais lattice:

$$V(\vec{r}) = f(\vec{r}) * \sum \delta(\vec{r} - \vec{R}_n) \tag{8}$$

where $f(\vec{r})$ is the potential of the basis and $\vec{R}_n$ denotes the Bravais lattice vectors. Using the convolution theorem of Fourier transforms, the scattered wave is given as:

$$\psi_s(q) = \mathscr{F}(f(\vec{r}))\mathscr{F}(\sum \delta(\vec{r} - \vec{R}_n) \tag{9}$$

Friedel's law states that the product of any Fourier transform with its complex conjugate is centrosymmetric [19]. The observed intensity of the scattered wave is given as

$$I(\vec{q}) = \psi_s \psi_s^* \tag{10}$$

and therefore satisfies Friedel's law. According to kinematical diffraction theory, all observed diffraction patterns should therefore exhibit centrosymmetry. As electrons interact strongly with specimens, the kinematical approximation of a single scattering event for 200 kV electrons would require specimens of thicknesses $t < 5$ nm [20]. As typical TEM specimens are an order of magnitude thicker, a theory taking into account multiple scattering events is required to accurately predict electron diffraction patterns.

2.2.3 Dynamical Theory of Diffraction

Several theoretical approaches have been developed to describe the scattering of high energy electrons from crystals [21]. The method presented here was first described by Bethe, and treats the incoming electrons as linear super-positions of Bloch waves [22].

Starting from the Schrodinger's equation for an electron in a crystal potential:

$$\nabla^2\psi(\vec{r}) + \frac{8\pi^2 m|e|}{h^2}[E + V(\vec{r}]\psi(\vec{r}) = 0 \tag{11}$$

where $V(\vec{r})$ is the crystal potential, E is the incident electron accelerating potential, m is the relativistic mass of the electron, e is the electron charge and h is Planck's constant. In Bethe's derivation the crystal potential is expanded into a Fourier series, and the wave-function is expressed as a superposition of Bloch waves. A set of equations is acquired:

$$[K^2 - (\vec{k} + \vec{g})^2]C_g + \sum_{h \neq g} U_{g-h}C_h = 0 \tag{12}$$

where there is one such equation for each reciprocal lattice vector $\vec{g}$ (which represents a reflected beam) considered. In equation 12, U represents the Fourier coefficients of a modified crystal potential, C represents the Bloch wave coefficients of the wave-function, K is a constant related to the electron energy and $\vec{k}$ is the crystal wave vector. The set of equations represented by equation 12 provide an exact solution provided all possible reflections $\vec{g}$ are considered. For practical purposes approximate solutions can be achieved by using a finite number of reflections in calculations. For a detailed derivation and discussion of dynamical diffraction the reader is referred to Humphreys [20].

2.3 Transmission Electron Microscopy

The following sections are based on Williams and Carter [17] and give a brief introduction to transmission electron microscopy.

Transmission electron microscopes (TEMs) operate by many of the same principles as light microscopes. Whereas light microscopes use glass lenses to focus photons, electron microscopes use magnetic coils to focus an electron beam. The motivation behind development of the TEM was a desire to surpass the resolution limit imposed on light microscopes by the wavelength of their radiation. Rayleigh's criterion

$$R_{LIM} \propto \lambda \tag{13}$$

relates a spatial resolution limit R_{LIM} to the wavelength of the probing particle λ. The de Brogile relation gives the wavelength of a particle as

$$\lambda = \frac{\hbar}{p} \tag{14}$$

where $\hbar$ is the reduced Planck's constant and p is the momentum of the particle. From equation 13 and 14 it can be seen that higher momentum of probing particles reduces the resolution limit. It is possible to produce electrons with momentum several orders of magnitude larger than photons, resulting in shorter wavelengths. The high momentum is achieved by accelerating the electron through a column with an applied voltage of 60 to 1200 kV. Taking into account relativistic corrections this gives wavelengths on the order of picometers (m^{-12}). However, the effective spatial resolution in a TEM is around 2 orders of magnitude lower, due to imperfections in the magnetic coil lenses. In a TEM an electron beam is scattered by a specimen. The scattered beam is subsequently focused through a system of magnetic lenses. The image plane of the lens system will show a projection of the specimen in the beam direction. A schematic of a TEM is shown in Figure 5. As electrons interact strongly with materials due to their charge, specimens need to be thin, on the order of 100 nm, to transmit a sufficient electron signal.

2.3.1 TEM Operation Modes

In the back focal plane of the objective lens (OL), all the rays with identical angles when incident on the OL converge. For a collimated electron beam this is equivalent to stating that all electrons scattered a certain direction meet in the back focal plane of the OL. The back focal plane is therefore also called the diffraction plane. By inserting apertures in the diffraction plane it is possible to filter out electrons scattered through certain angles. In the case where an aperture only lets the direct beam through, only electrons transmitted through the specimen without scattering are detected and we have bright field (BF) imaging. BF images have mass-thickness contrast, as the amount of specimen and the scattering cross section of the atoms determines the likelihood of scattering. Regions satisfying the Laue/Bragg criteria scatter more and will be darker in a BF image. This is called diffraction contrast, and is an important contrast mechanism in BF imaging. Conversely, if the direct beam is blocked by an aperture, and only scattered electrons are detected we have dark field (DF) imaging. In a DF image the regions that do not scatter, that is vacuum or thin sections, will be dark.

In Figure 6 a) the beam path for a TEM in imaging mode is shown. An aperture is inserted into the back focal plane, only letting the direct beam through, making this a BF setup. In

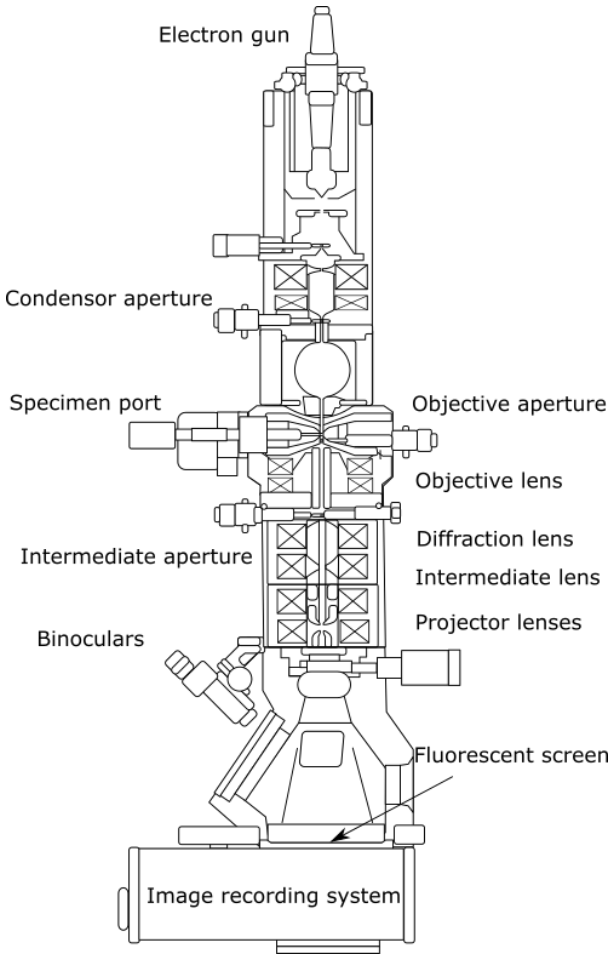

Figure 5: Schematic of a Transmission Electron Microscope. Figure from Wikimedia Commons [23].

Figure 6 b) the diffraction plane is projected onto the viewing screen, producing a diffraction pattern.

Another important TEM mode is selected area electron diffraction (SAED). Figure 6 b) shows the beam path for a TEM in SAED mode. The incident beam is parallel, and the diffraction plane is projected onto the viewing screen. As an aperture is inserted into the image plane, only beams scattered through a particular area of the specimen will be transmitted to the screen.

As the incident beam is parallel, the beam has only one incident direction on the specimen. The diffracting crystal planes can therefore be determined by placing one Ewald sphere in the reciprocal crystal lattice. The observed pattern is called a selected are electron diffraction pattern (SADP). Crystal orientations and lattice parameters can be determined from the SADP.

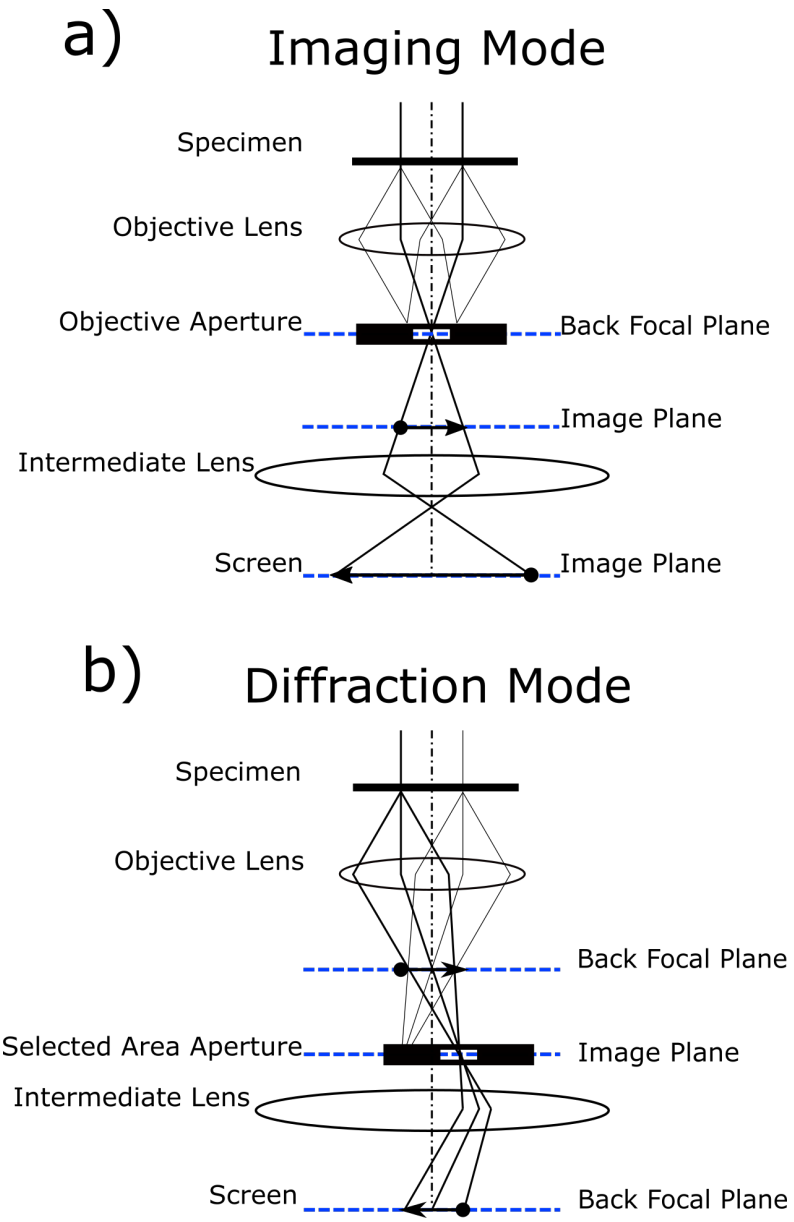

Figure 6: a) Schematic of a TEM in bright field imaging mode. An aperture in the back focal plane blocks electrons scattered more than a certain angle. This creates diffraction and mass-thickness contrast in the image projected on the screen. b) Schematic of a TEM in selected area electron diffraction mode. The aperture blocks out beams not scattered from a particular area in the specimen. The diffraction plane is projected onto the viewing screen, producing a diffraction pattern. Figures are appropriated from Williams and Carter [17].

2.3.2 Convergent Beam Electron Diffraction

Convergent beam electron diffraction (CBED) denotes a techniques in which the electron beam is converged on the specimen, and the resulting diffraction pattern is studied. One of the advantages of CBED over SAED is that the interaction volume of the electron beam is much smaller, offering higher spatial resolution. High spatial resolution combined with a range of incident beam angles causes CBED patterns to contain a wealth of data that is not possible to obtain through SAED [17]. Figure 7 shows a schematic of the CBED setup.

When converging an electron beam a disc is formed in the diffraction plane. As the diffraction plane maps out the angular distribution of the transmitted electrons, the disc shape is controlled by the angular distribution of the incoming electrons. The convergence angle α determines the range of incident beam directions, and therefore also the size of the disc in the diffraction plane. When the beam is converged on a crystalline specimen, the incident electron beam can scatter elastically with the specimen at angles satisfying the Bragg condition (equation 5). The incident convergent beam can be thought of as consisting of several individual beams with different incident angles. As each one of these beams produces a diffraction pattern, the resulting pattern consists of several SADPs side by side, producing discs as shown in Figure 7. The CBED patterns of non-overlapping discs produced by convergence angles $\alpha < \theta_B$ is called a Kossel-Mollenstedt pattern [24]. The minimum convergence angle of the beam can be adjusted by changing the condenser aperture.

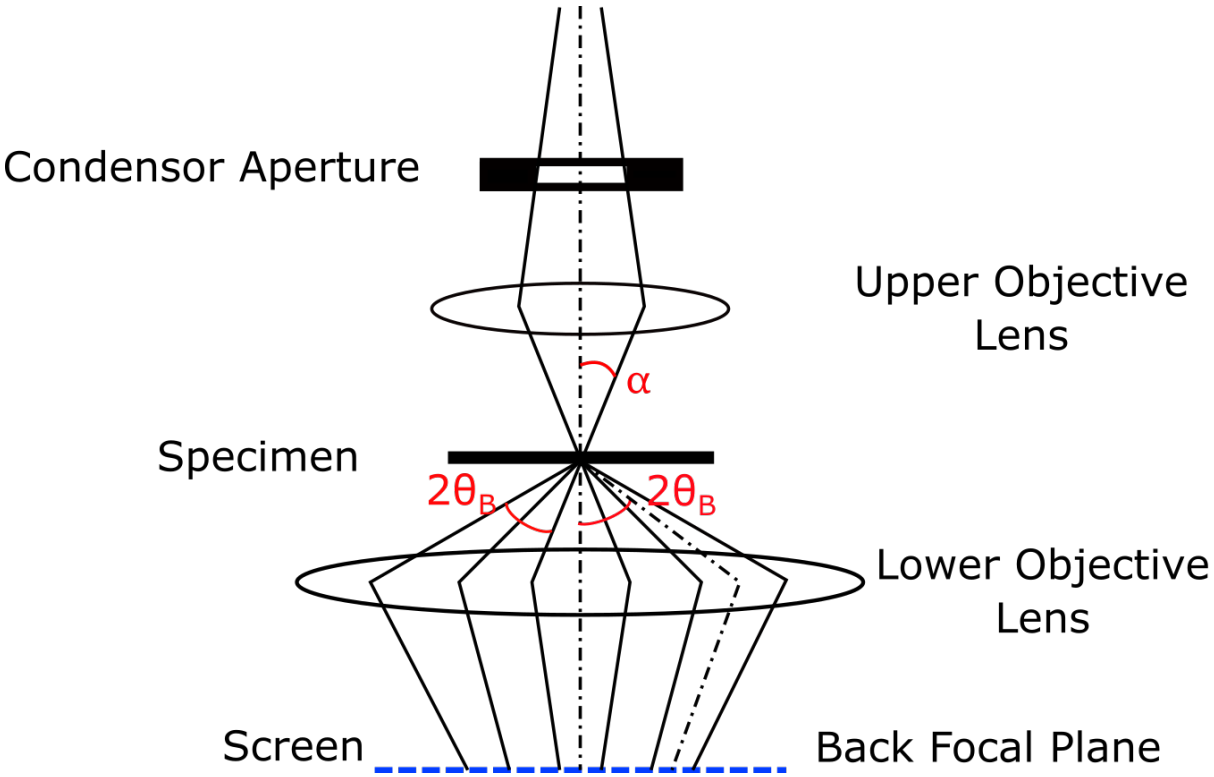

Figure 7: Schematic of beam path in a CBED experiment. The convergence angle is given as α and scattering angle satifying Braggs law is denoted θ_B. Due to the range of incident beam directions, the beam forms discs in the diffraction plane. Figure adapted from Williams and Carter [17].

2.3.3 Symmetry and the Breakdown of Friedel's Law

As stated previously, the kinematical approximation is invalid for all but the thinnest specimens for electron diffraction. Electron diffraction patterns are therefore often observed to break Friedel's law [25]. If the incoming beam is centrosymmetric, then any non-centrosymmetric features in the diffraction pattern can be attributed to the specimen. This opens up the possibility of distinguishing between centrosymmetric and non-centrosymmetric structures using electron diffraction [25].

In practice the extraction of detailed information from the specimen crystal structure by electron diffraction can be very challenging. For example, in SADP the intensities of the spots can not be used to make statements about the specimen symmetry. The reason for this is that the diffraction pattern comes from a relatively large area. That is, there are likely different specimen thicknesses, orientations and crystal imperfections in the probed area contributing to the diffraction pattern. The intensity distribution of the observed pattern can therefore not be directly interpreted as an expression of specimen (a)symmetry, as these other factors also influence the intensity in unknown ways [26].

In CBED the interaction volume is much smaller, increasing the probability that the interaction volume is uniform, free of defects and does not contain multiple crystal domains. Given that the crystal area satisfies these requirements, this would allow interpretation of the intensity distribution of the CBED pattern as an expression of (a)symmetry in the specimen. A crystal structure which is symmetric in the given ZA will produce a CBED pattern with the same symmetry. Therefore, CBED patterns could be used to determine the exact point group of a crystal structure [26]. For example, asymmetry in CBED patterns could be used to determine the polarization direction of a material. Several studies have been conducted correlating asymmetry in CBED patterns to polarization [27][10]. Combining CBED and electron diffraction scanning routines it is possible to create symmetry maps to determine the polarization in a specimen [13][12][11].

2.4 Material

In order to understand the results acquired by TEM, it is necessary to have some understanding of the materials studied. In this thesis the materials characterized were barium titanate (BTO) thin films grown on strontium titanate (STO). First, sections 2.4.1 and 2.4.2 review relevant information regarding STO and BTO. Sections 2.4.3 and 2.4.4 review strain engineering and domain formation in ferroelectric thin films, respectively. Finally section 2.4.5 reviews previous work on the material system investigated in this thesis.

2.4.1 Strontium Titanate

Strontium titanate is an oxide with chemical formula $SrTiO_3$. At room temperature STO is a centrosymmetric paraelectric with a perovskite structure. STO belongs to the cubic crystal system and has space group $Pm\bar{3}m$. The lattice parameter is $a = 3.905$ Å and the angles are $\alpha = \beta = \gamma = 90°$. The atomic coordinates of STO are listed in table 2 [28].

Table 2: Atomic coordinates of STO at room temperature. The space group is $Pm\bar{3}m$ and the lattice parameter is $a = 3.905$ Å [28].

Element	X	Y	Z	Occupation
Sr	0	0	0	1
Ti	$\frac{1}{2}$	$\frac{1}{2}$	$\frac{1}{2}$	1
O	0	$\frac{1}{2}$	$\frac{1}{2}$	1

2.4.2 Barium Titanite

Barium Titanate (BTO) is an oxide with chemical formula $BaTiO_3$. At room temperature BTO is a ferroelectric with a perovskite structure. BTO belongs to the tetragonal crystal system and has space group $P4mm$. The lattice parameters are $a = b = 3.992$ Å and $c = 4.036$ Å with angles $\alpha = \beta = \gamma = 90°$ [29]. The atomic coordinates of BTO are listed in table 3. The ferroelectric properties of the tetragonal phase are caused by displacement of the titanium and oxygen atoms, as shown in Figure 8 a). This displacement gives the unit cell a net dipole-moment, giving the material a net polarization. At around 130°C, bulk BTO undergoes a phase transition from the tetragonal ferroelectric phase to a paraelectric cubic phase [30][31], shown in Figure 8 b). The temperature at which a ferroelectric phase transitions to a non-ferroelectric phase is known as the Curie temperature.

Comparing the ferroelectric and paraelectric phases it is seen that the ferroelectric phase is not centrosymmetric. In the ferroelectric phase a mirror plane orthogonal to the direction of polarization is broken. The mirror plane in question is indicated in Figures 8 a) and b)

Table 3: Atomic coordinates of BTO at room temperature. The space group is $P4mm$ and the lattice parameters are $a = b = 3.992$ Å and $c = 4.036$ Å [29].

Element	X	Y	Z	Occupation
Ba	0	0	0	1
Ti	$\frac{1}{2}$	$\frac{1}{2}$	0.518(2)	1
O	$\frac{1}{2}$	0	$\frac{1}{2}$	1
O	$\frac{1}{2}$	$\frac{1}{2}$	0	1

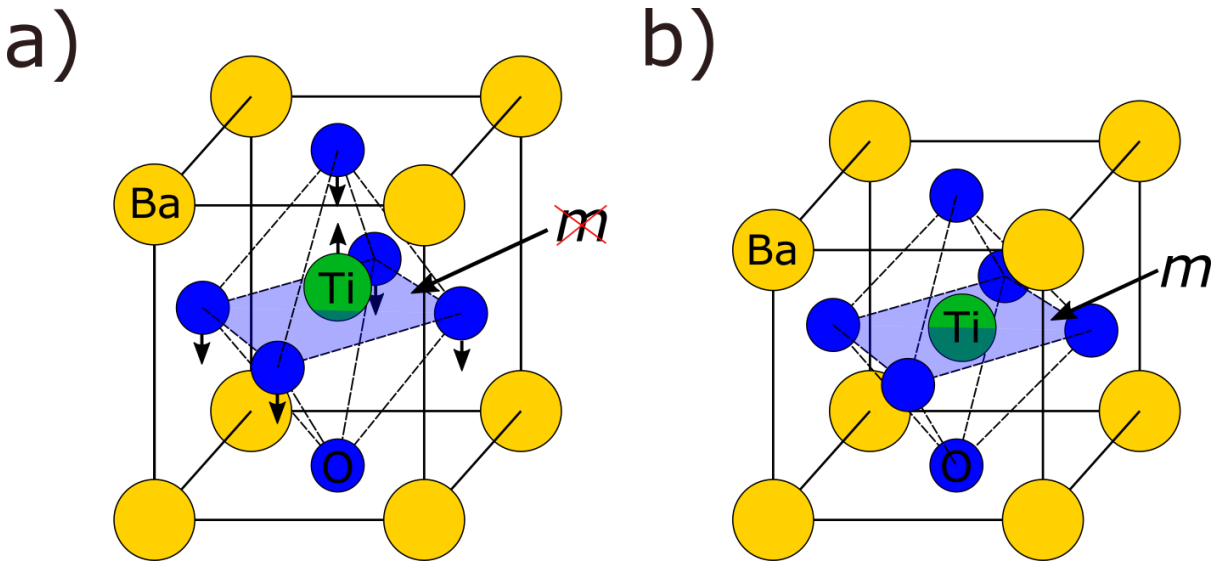

Figure 8: a) At room temperature BTO is in a ferroelectric tetragonal phase, with a displacement of the titanium and oxygen atoms causing a net polarization of the unit cell. The unit cell is not centrosymmetric. b) Over the Curie temperature BTO is in a paraelectric cubic phase of BTO. The unit cell is centrosymmetric.

Due to its high dielectric constant the main industrial application for BTO are capacitors, with annual production exceeding a billion units [3]. BTO is also of interest for applications that seek to utilize the ferroelectric properties of the material, such as optical modulators and ferroelectric memory [32]. Nanoscale thin films of BTO are of research interest, as they could satisfy the size constraints imposed by miniature devices [4][33]. A limiting factor to the application of BTO is the low Curie temperature of about 130°C [30], and there has been an historical research effort to find what factors influence the Curie temperature of BTO [34][35].

2.4.3 Strain Engineering Ferroelectric Thin Films

Large strains can exist in thin films due to differences in lattice parameters and thermal expansion coefficients of the film and substrate materials, as well as from defects in the film-substrate interface [36][37][38]. These strains have the potential to significantly change the properties of thin film BTO compared to bulk BTO. Intentional variation of film growth parameters and substrates offers the possibility to influence film attributes through strain, namely strain engineering. Interfacial strains have been reported to decrease the Curie temperature to 9.5°C [39] and conversely also increase it to up to 500 °C [40][15]. This following section will give a brief overview of how strain in the film-substrate interface is formed and relieved during epitaxial growth.

Two of the main driving forces behind interface strain in the material are the differing lattice parameters and thermal expansion coefficients of substrate and film [41]. These two driving forces determine the energy associated with forming coherent, semi-coherent or incoherent interfaces. Very thin films usually form coherent interfaces, as few film atoms have to be displaced from their bulk-equilibrium positions to achieve coherency. Once the films exceed a certain thickness, called the critical thickness, the energy required to form a coherent boundary is larger than the energy required to form dislocations, and thus a semi-coherent boundary with misfit dislocations is formed [42][43]. These dislocations are called

coherency dislocations, as they preserve the continuity of lattice points across the interface. The periodicity of these dislocations depends on the difference in substrate and film lattice parameter [41][44].

For a 12 nm thin BTO film grown on STO by pulsed laser deposition, it was observed that the in-plane lattice parameter contracts, whereas the out-of-plane lattice parameter extends [42]. Figure 9 a) shows this schematically. For thicker BTO films on STO substrates the formation of arrays of coherency dislocations are observed, as well as an relaxation of the film lattice parameter to the bulk values [42][41]. Figure 9 b) shows a schematic of a relaxed film-interface substrate with a coherency dislocation. From experimental measurements, Suzuki et al. estimate the critical thickness of the BTO films grown by pulsed laser deposition to be approximately 5 nm.

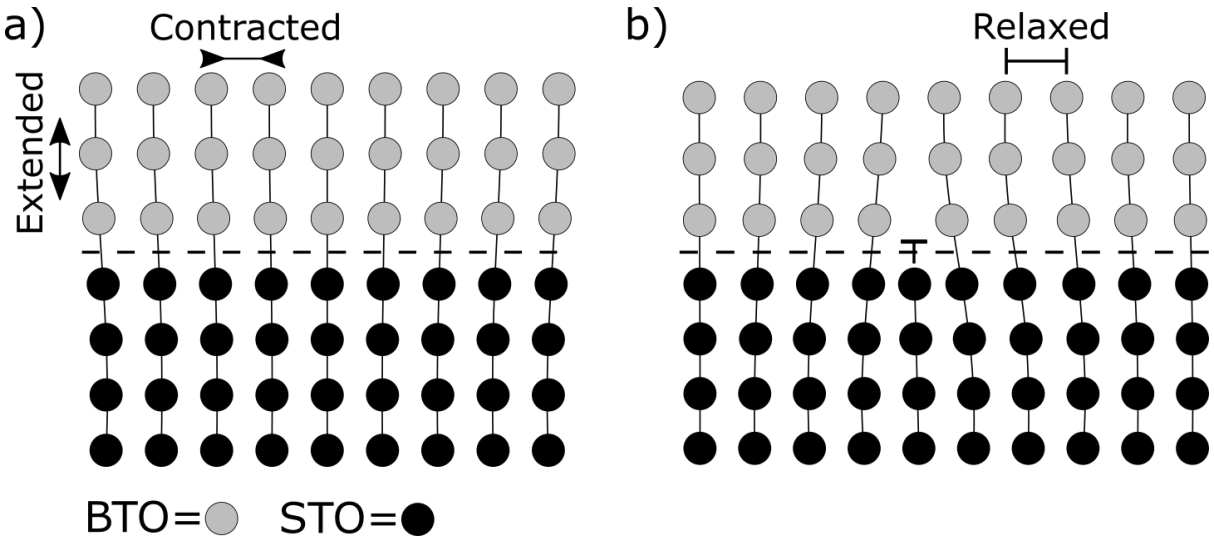

Figure 9: a) Schematic of the results observed by Suzuki et al. [42] from 12 nm BTO films deposited on STO substrates. The in-plane BTO lattice parameter contracts, whereas the out-of-plane lattice parameter extends. b) Schematic of a semi-coherent boundary with coherency dislocations, as observed in thicker BTO films on STO substrates [42]. Compared to a) the film atoms deviate less from their regular lattice sites. Figure adapted from Smallman [44].

2.4.4 Domain Formation in Ferroelectric Thin Films

Below the Curie temperature, a ferroelectric tetragonal material can be clamped onto a cubic substrate in three main ways. The c-axis can be perpendicular to the interface, called a c-domain, or an a-axis can be perpendicular to the interface, called an a-domain. There can be two different types of a-domain in a film, rotated 90° with respect to each other. Figure 10 shows the 3 different configurations in which a tetragonal structure can be fitted onto a cubic substrate [37].

The area separating two domains of different polarization is called a domain wall. In the domain wall the polarization is observed to change gradually from one domain to the next. As the polarization is a result of the atom positions in the unit cell, it follows that the domain wall is a region of varying unit cells. Ferroelectric domain walls can therefore be seen as defects in the crystal structure of the material, producing local variations in symmetry and strain [45]. Figure 11 shows a schematic of a domain wall.

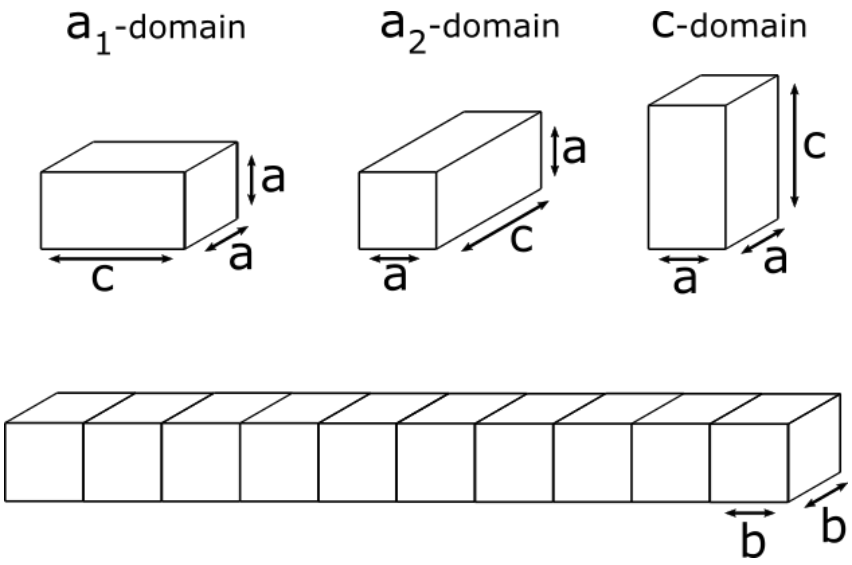

Figure 10: Schematic showing the three standard ways a tetragonal film can grow epitaxially on the (001) face of a cubic substrate. Figure adapted from Speck et al. [37].

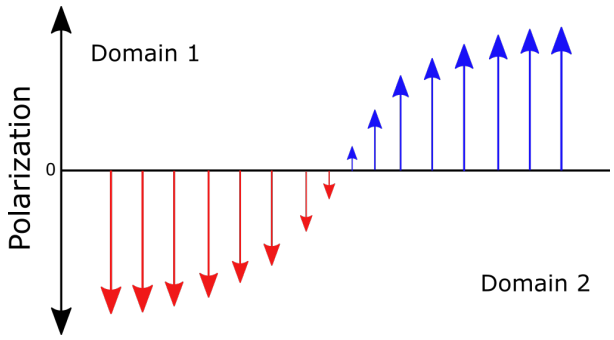

Figure 11: Schematic of a domain wall. The polarization varies gradually from one domain to the next. Ferroelectric domain walls can be seen as defects in the crystal structure of the material, producing local variations in symmetry and strain. Figure appropriated from Lee [46].

The cooling of the film from the annealing temperature will cause any differences in thermal expansion coefficient to induce new strains, at least in films clamped to the substrate. This can induce either a compressive- or tensile-strain in the film, depending on the thermal expansion coefficients of substrate and film. It has been shown that the creation of alternating domain patterns in the film can cause a lowering of the interfacial energy [47]. Alternating a_1, a_2 domain pattern, shown in Figure 12, were observed to form in single crystal BTO films by Luk'yanchuk et al. [48]. The pattern consists of domains with alternating unit cell elongations in the [001] and [010] directions. The domain width was found to be approximately proportional to the square root of the film thickness [48].

Furthermore, it has been shown theoretically that slight rotations of the crystal domains are possible, as their formation can be energetically favorable [49]. The formation of rotated domains in tetragonal ferroelectric thin films on cubic substrates was confirmed experimentally by Speck et al. [37]. Figure 13 shows alternating domains rotated with angles ω with respect to the substrate.

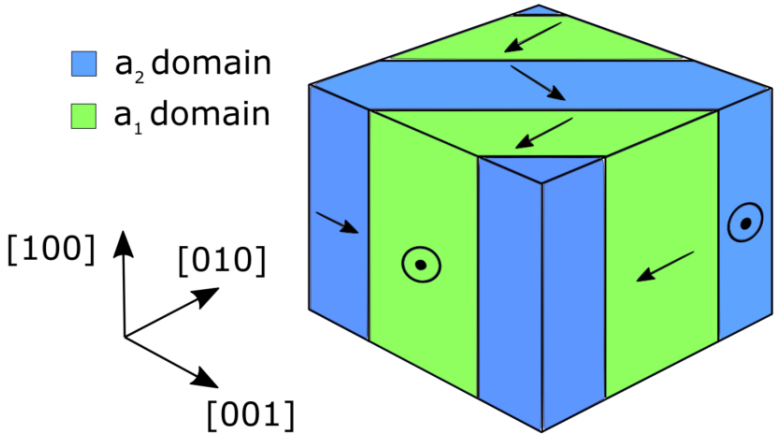

Figure 12: Schematic of the $a_1 - a_2$ domain pattern found in BTO thin films [48]. The pattern arises to minimize stress. Arrows indicate the polarization direction, which is coincident with the lattice elongation. Figure adapted from Raeder et al. [9].

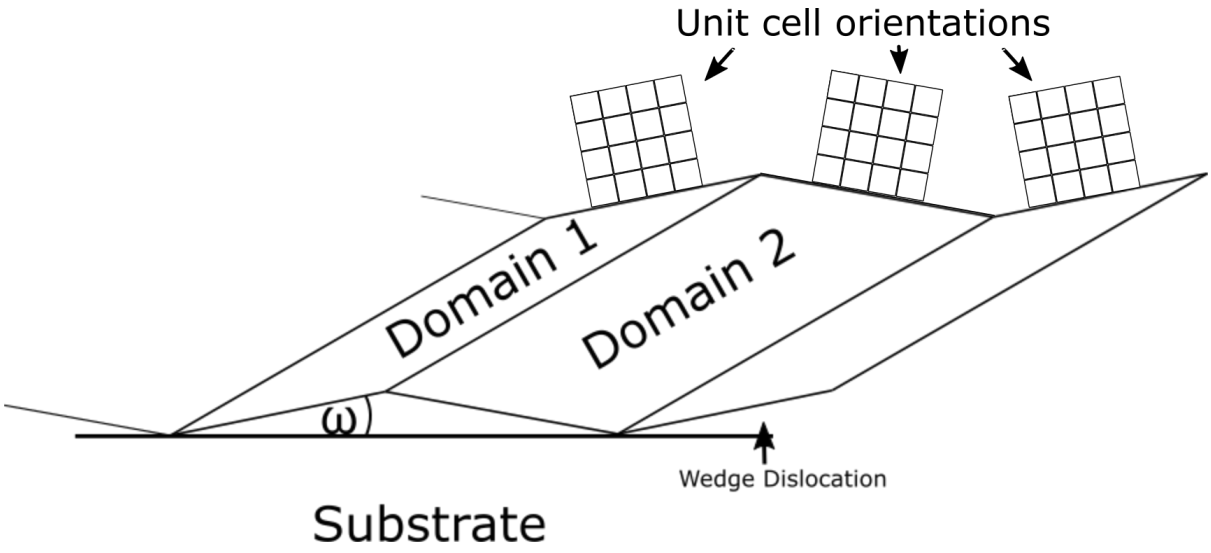

Figure 13: Schematic of alternating domains rotated with respect to the substrate. The misfit induced by the rotation can be characterized as a wedge dislocation, which is itself composed of an array of edge dislocations. Figure adapted from Speck et al. [37].

2.4.5 Previous Study of the Material System

This section reviews previous work on thin film synthesized in a similar way as the thin films characterized in this thesis, by the same group at the Department of Material Science and Engineering, NTNU.

As chemical solution deposition (CSD) offers a cost-effective and scalable way of producing high quality thin films of BTO, it has been the subject of previous research [7][8]. Common for all previous studies is a reliance on organic solvents in the synthesis process, generally irritant or toxic, which complicate the fabrication process.

Raeder et al. [9] for the first time used an aqueous CSD route to produce BTO thin films on single crystal STO substrate. This novel approach to CSD synthesis replaces toxic organic solvents with water, resulting in a more cost-effective and benign fabrication process. The in-plane and out-of-plane lattice parameters of BTO were found to be 4.010 ± 0.013 Å and 4.000 ± 0.007 Å by X-ray diffraction. The higher in-plane lattice parameter was attributed to the lower thermal expansion coefficient of STO, as the expansion differential would cause in-plane strain for a film clamped to the substrate. The in-plane dielectric properties of the film were measured using interdigitated electrodes. Ferroelectric properties were observed up to 160 ± 5°C, and an enhanced in-plane polarization was observed. The enhanced Curie temperature and in-plane polarization were proposed to result from a domain pattern with predominantly in-plane polarization.

The $a_1 - a_2$ domain pattern proposed to account for the observed results is schematically shown in figure 12. This domain pattern has predominantly in-plane polarization. Measurements by Raeder [50] showed that the domain width in an approximately 170 nm thin film was about 58 nm. This is in good agreement with the model proposed by Luk'yanchuk et al. [48].

2.5 Image Processing

The following sections introduce concepts in the field of image processing that were used in this thesis. First, section 2.5.1 introduces the Canny edge detection algorithm. Section 2.5.2 presents metrics to compare and extract information from images. Finally section 2.5.3 gives a short introduction to template matching and its relation to cross-correlation.

2.5.1 Canny Edge Detection

It is often of interest to find the positions of edges in images, as this can convey important information and dramatically reduce the amount of data being processed. In his 1987 landmark paper[51], John Canny specifies a comprehensive set of goals that a good edge detection algorithm should aim to satisfy, and proposes an algorithm that meets the set requirements. The algorithm is now known as the Canny edge detector and has found wide application in various computer vision systems.

The general criteria for edge detection specified by Canny are:

- The algorithm should accurately detect as many edges in the image as possible
- The output edges of the program should be localized at the center of the edges of the original image
- A given edge should only be marked once, and image noise should not create false edges

The proposed algorithm to satisfy these constraints can be broken down to five steps:

- Application of a Gaussian Filter to smooth the image and remove noise
- Computing the intensity gradients of the image
- Identifying the largest gradients as edges
- Applying thresholds to filter out edges caused by noise
- Suppress all weak edges that are not connected to strong edges

Here a strong edge denotes a region where the image has a high intensity gradient, and a weak edge is a region where the image has a low intensity gradient. Since its publication, several improvements to the traditional algorithm have been proposed [52][53][54]. Figure 14 a) and b) show an image before and after application of the Canny edge detector. For more details on the implementation of the Canny edge detector the reader is referred to Canny [51].

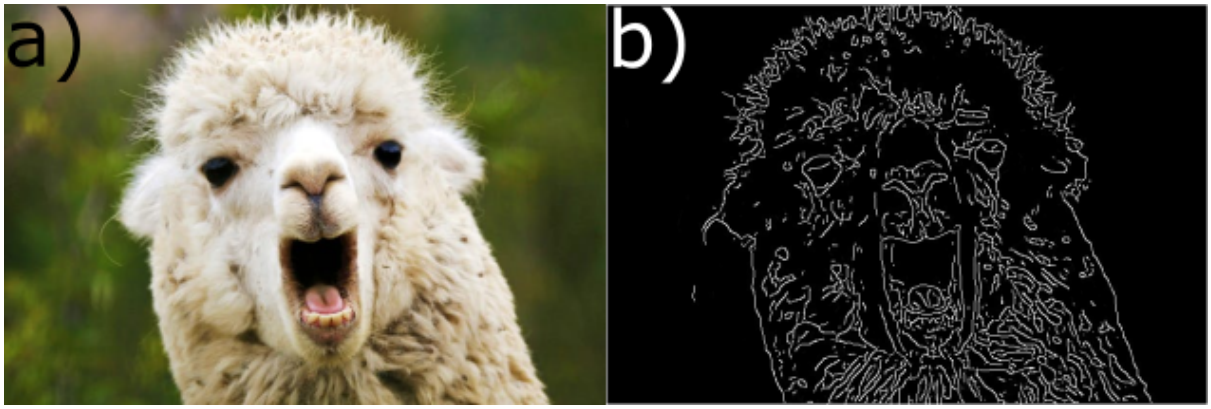

Figure 14: a) An image of a llama [55]. b) An image of a llama after Canny edge detection.

2.5.2 Image Metrics

To determine if an image A is related to an image B by a certain symmetry operation S, a standard approach is to perform the symmetry operation S on image A and then compare the transformed image A_S with image B. If images A and B were indeed related by the symmetry operation S, then A_S and B would be identical. The degree to which A and B are symmetrical is equal to the degree A_S and B are similar. Images can be represented digitally as simple two dimensional functions where a value, the registered intensity, is assigned to each pixel position. The problem of finding the degree to which two images are symmetrical is thus identical to finding the similarity of two functions.

There are several metrics for quantifying the similarity of two functions [56]. A metric used widely is the normalized cross-correlation coefficient [57]

$$\gamma = \frac{\sum_{x,y}\{[I_A(x,y) - \bar{I}_A][I_B(x,y) - \bar{I}_B]\}}{\sqrt{\{\sum_{x,y}[I_A(x,y) - \bar{I}_A]^2\}\{\sum_{x,y}[I_B(x,y) - \bar{I}_B]^2\}}} \tag{15}$$

where $I_A(x,y)$ and $I_B(x,y)$ denote the intensity of image A and image B as a function of the coordinates x and y. $\bar{I}_A$ and $\bar{I}_B$ denote the average pixel intensity of image A and image B respectively. The highest value of γ is 1, at which point I_A and I_B are identical. The cross-correlation coefficient is widely used in digital image processing to quantify the similarity of two images. The average intensity is subtracted, which makes γ less sensitive to differences in background intensity of the compared images.

Specifically for this thesis, the displacement of the intensity maxima of the 000 disc of a CBED pattern from the center of the disc is of interest (as will be evident after section 4.4). To quantify how far the maximum intensity of the 000 disc is from the center of the disc, the metric C is introduced:

$$C = 1 - \frac{|\vec{r}_c - \vec{r}_{max}|}{|r_D|} \tag{16}$$

where $\vec{r}_c$ is the center position of the disc, $\vec{r}_{max}$ is the position of the point of maximum intensity and r_D is the radius of the CBED disc. If the maximum intensity coincides with the center of the disc C equals 1, while a disc with maximum intensity at the edges will give a C of 0. Figure 15 illustrates what values the C of an image will have for different positions of the intensity maxima.

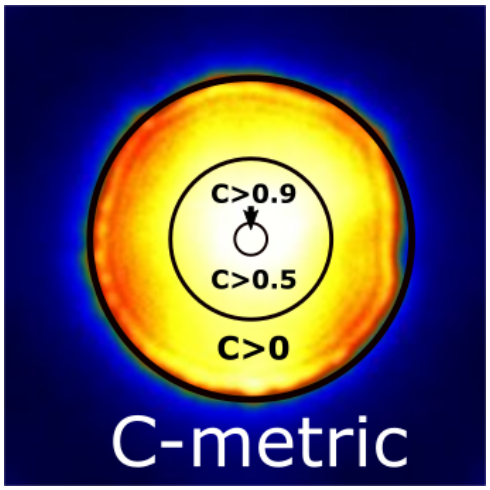

Figure 15: The C metric is introduced to have a quantitative metric of where the intensity maxima of the 000 disc in a CBED pattern is located. If the maximum pixel intensity of is in the middle of the disc, C=1. If the maximum pixel intensity is on the edge of the disc, C=0. The value of C decreases as the maximum intensity moves from the center to the edge. Circles have been drawn around the center to indicate what C would be if the point of maximum intensity is outside the center.

2.5.3 Cross-Correlation and Template Matching

Given two digital images I_1 and I_2, a way to quantify their similarity is calculating the euclidean distance between the images:

$$\Delta^2 = \sum_{x,y} [I_1(x,y) - I_2(x,y)]^2 \tag{17}$$

where we sum over all pixel positions (x,y). Template matching is a technique in digital image processing for identifying sections in an image that are similar to a template. One way of doing this is finding the euclidean distance of the template with respect to the image for all possible template positions. This can be expressed as:

$$\Delta^2(u,v) = \sum_{x,y} [f(x,y) - t(x-u, y-v)]^2 \tag{18}$$

where f is the image function, t is the template and the sum x, y is over the window containing the feature at position (u,v) we want to compare to the template. In the expansion of Δ^2

$$\Delta^2(u,v) = \sum_{x,y} [f^2(x,y) - 2f(x,y)\,t(x-u, y-v) + t^2(x-u, y-v)] \tag{19}$$

the term $\sum t^2(x-u, y-v)$ is constant. Assuming the term $\sum f^2(x,y)$ remains approximately constant, then the remaining term

$$c(u,v) = \sum_{x,y} f(x,y)\,t(x-u, y-v) \tag{20}$$

can be used as an estimate for the similarity of the images. Here c is called the cross-correlation term. Using the Fourier convolution theorem we see that cross-correlation can be expressed as:

$$c(u,v) = \mathscr{F}^{-1}[\mathscr{F}(f)\mathscr{F}^*(t)] \tag{21}$$

where $\mathscr{F}^*(t)$ is the complex conjugate of the Fourier transform of the template. Figure 16 illustrates how a template is compared to sections of the image. The calculated cross-correlation c for each position (u,v) is stored in a cross-correlation map. Positions in the cross-correlation map with high c correspond to sections of the image that are similar to the template. Calculating the cross-correlation of images in the Fourier transform has a lower computational cost than the direct method for almost all images [57]. The normalized cross-correlation coefficient presented in 15 can also be utilized for template matching [58].

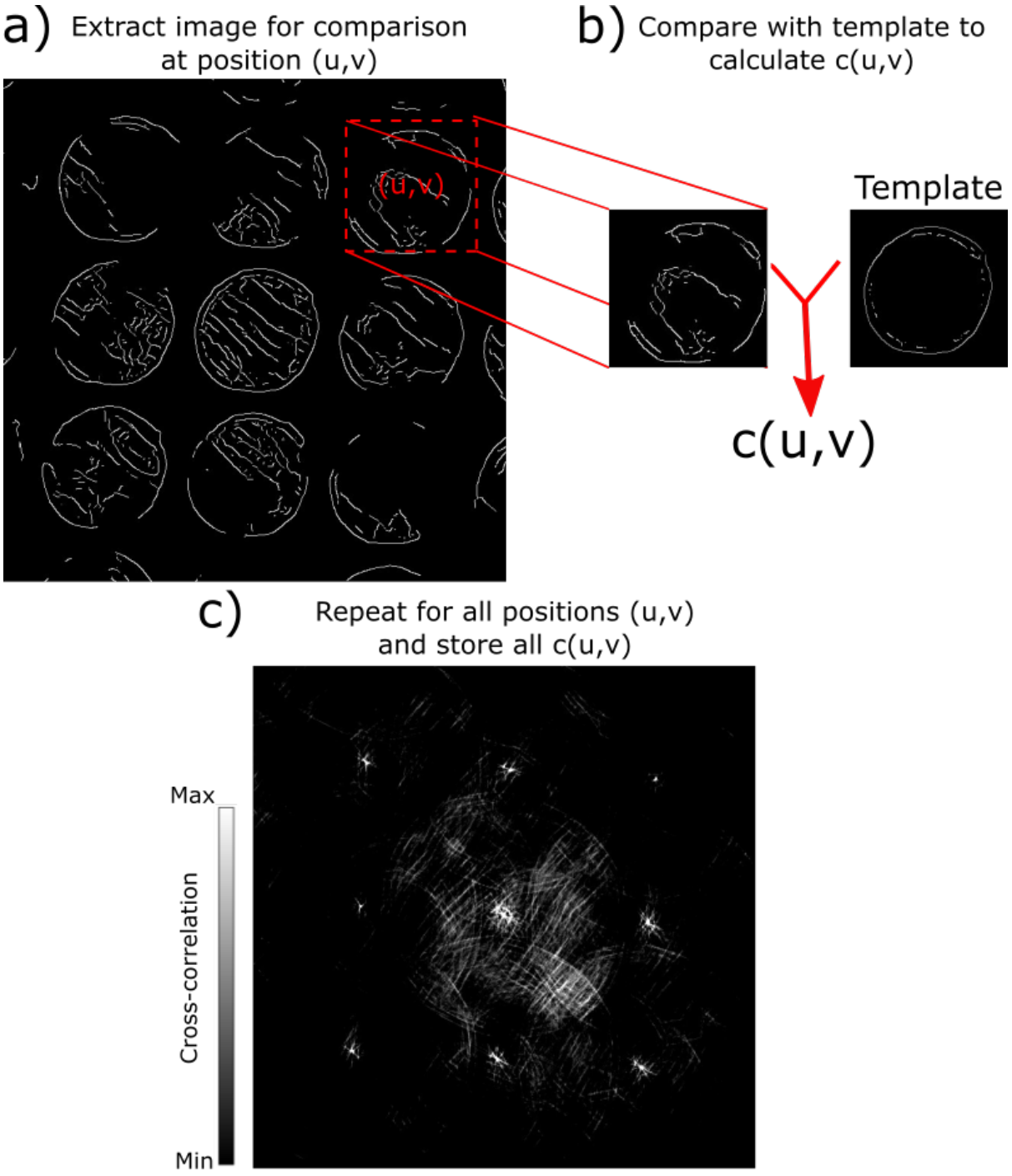

Figure 16: Figure to illustrate template matching. a) A section of the image is extracted. b) The extracted section is compared with the template, and the cross-correlation term c is computed. c) This is repeated for all pixel positions (u,v) until a map of the c is produced.

3 Method

Section 3.1 gives a brief presentation of the synthesis of the material analyzed, followed by a presentation of the specimen preparation procedure in section 3.2. Section 3.3 presents the parameters used in the CBED Bloch wave simulations. Section 3.4 presents the TEM experimental conditions and the techniques used. Finally, section 3.5 presents how the collected data were processed.

3.1 Thin Film Synthesis

The materials studied are BTO thin films grown on single crystal STO substrates. The thin films were synthesized by chemical solution deposition at the Department of Material Science and Engineering, NTNU, by PhD candidate Kristine Bakken. Two specimens were made with different heat treatments. A brief presentation of the deposition technique used is given here.

First, $BaTiO_3$ precursor solution was deposited on (100) single crystal STO (1 cm x 1 cm, Crystal-GMBH). The solution was then spin coated onto the substrates at 3000 rpm.

Spin coating is a procedure by which a small amount of the solution is deposited in the centre of the substrate, which is subsequently rotated at a high speed to spread the solution over the film by centrifugal force. It is not guaranteed that the film evened out perfectly during spin coating, which led to the assumption that the film quality was better closer to the centre of the substrate.

The coated substrates were heated from below for thermal annealing, on a heating setup comparable to a rapid thermal processing furnace [59]. Two films were synthesized, with maximum temperatures 700°C and 1000°C. The heating program was:

1. Heated to 455°C at 1.5°C/s
2. Heated to 588°C at 0.67°C/s
3. Heating to 700°C or 1000°C at 5°C/s
4. Held at max temperature for 5 min
5. The specimens held at 1000°C were cooled to 740°C in 90 seconds
6. The remaining cooling was achieved by turning off the heat

The cycle of deposition, spin-coating and thermal annealing was repeated 6 times to obtain the desired film-thickness [59]. Figure 17 shows a schematic representation of the specimen preparation procedure.

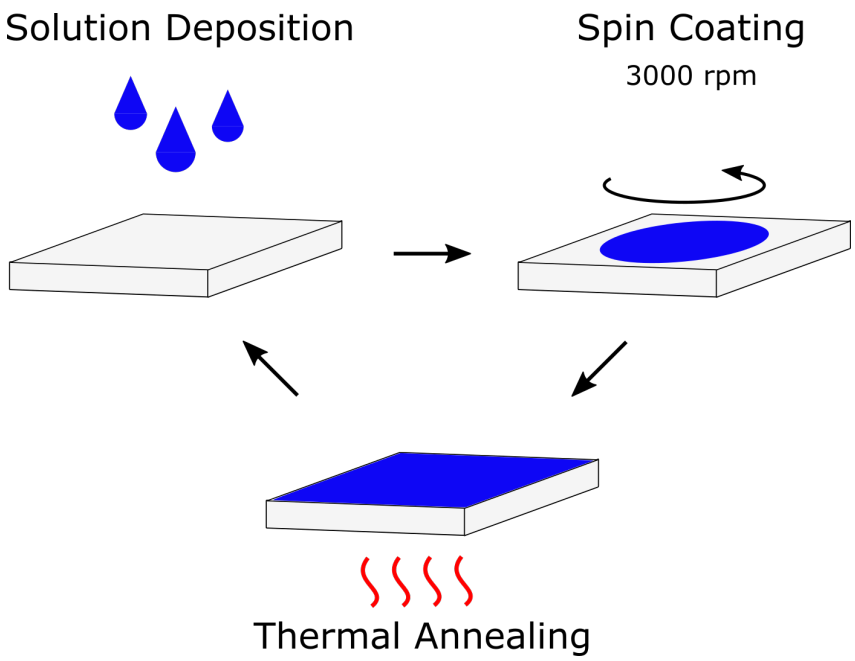

Figure 17: An illustration of the thin film synthesis. The precursor solution is deposited on (100) oriented STO substrates. The substrates with solution are spin coated for full coverage. Finally the substrate with solution is thermally annealed. This process is repeated multiple times until the desired film thickness is achieved. Figure adapted from Toresen [60].

3.2 Focused Ion Beam TEM Specimen Preparation

A FEI Helios NanoLab DualBeam Focused Ion Beam (FIB) at NTNU NanoLab was used to prepare the TEM specimens. The FIB is equipped with both an electron gun for producing scanning electron microscope (SEM) images and a focused ion beam. These beams can be used to sputter away material and to deposit carbon by introducing a precursor gas into the vacuum chamber. The high precision of the focused ion beam milling enables the production of extremely thin specimens suitable for analysis by TEM. Both specimens were prepared by Per Erik Vullum, Senior Researcher at SINTEF Industry. The following section will outline the specimen preparation process.

The specimens were extracted from the rectangular STO wafer with dimensions 1 cm x 1 cm. To avoid charging by the electron beam the wafer was coated with a conductive platinum-palladium layer using a Cressington Sputter Coater Model 208 HR. A section of interest in the middle of the wafer was chosen and carbon was deposited, first with the electron and then with the ion beam to form an additional protective layer. Figure 18 a) shows the area of interest with a protective carbon layer.

Several ditches were dug through the substrate surrounding the film area of interest, leaving the area of interest connected to the substrate by nothing but a thin bridge of material. An Easylift needle was attached to the specimen before cutting the connection to the wafer. The specimen was then mounted on a copper FIB Lift-Out TEM Grid and thinned further by the ion beam. Three film sections with different thicknesses were produced. Measured in the FIB, the specimen thicknesses of the areas were approximately 75, 130 and 250 nm. Figure 18 b) shows an image of the thinned specimen mounted on the TEM grid. The specimen is connected to the TEM grid on both sides.

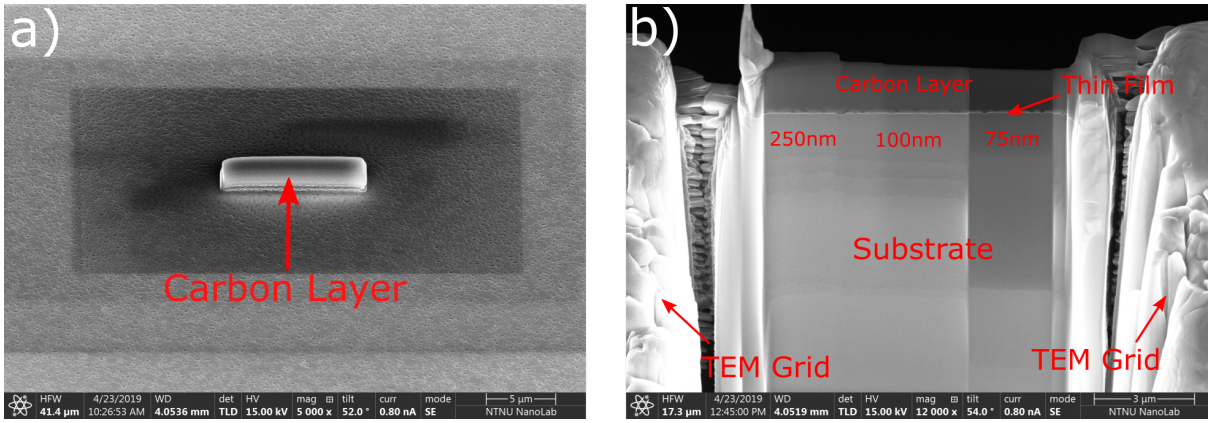

Figure 18: SEM images acquired during specimen preparation, courtesy of SINTEF Senior Researcher Per Erik Vullum. a) A section of the thin-film with protective Pt/Pd and carbon layers. b) Cross sectional view of the TEM specimen prepared with 3 different thicknesses.

3.3 CBED Simulations

The CBED simulations presented in this thesis use a Bloch wave method with the atomic scattering factors of Doyle and Turner [61], 200 kV electron acceleration voltage and a total of 120 strong reflections. Simulations were performed on BTO and STO on the [001] ZA, for different crystal thicknesses and different beam misalignment. The unit cells used in the simulations are presented in section 2.4.2 and section 2.4.1. The simulations were performed in JEMS [62].

3.4 TEM Operation Modes

The TEM used in this thesis is a JEOL JEM-2100F. The instrument is part of the Norwegian Centre of Transmission Electron Microcsopy (NORTEM) infrastructure at the TEM Gemini Centre, NTNU, Trondheim. The electron source of the microscope is a Schottky type tungsten field emission gun (FEG). The operation voltage used in this work was 200 kV. Furthermore, the microscope is equipped with a Gatan 2k Ultrascan bottom mounted CCD camera and uses the Gatan Digital Micrograph software. Specimen holders of the type JEOL Specimen Tilting Beryllium Holder, with the capacity to tilt up to $\pm$ 35° both parallel and orthogonal to its axis, were used in all experiments.

3.4.1 Selected Area Electron Diffraction

SADP of the film were taken using a ≈130 nm diameter aperture. During SADP acquisition only the aperture was moved, while the specimen was stationary. This was done to accurately determine where in the film the diffraction pattern was acquired.

SADP were acquired from the bulk of the STO substrate, providing a reference for the calibration of the diffraction patterns. Figure 19 a) shows a typical diffraction pattern obtained from the BTO film. Figure 19 b) shows the 040 diffraction peaks magnified. The exact distances between peaks were found by drawing line profiles. Figure 19 c) shows an excerpt of a line profile where the BTO and STO peaks are visible.

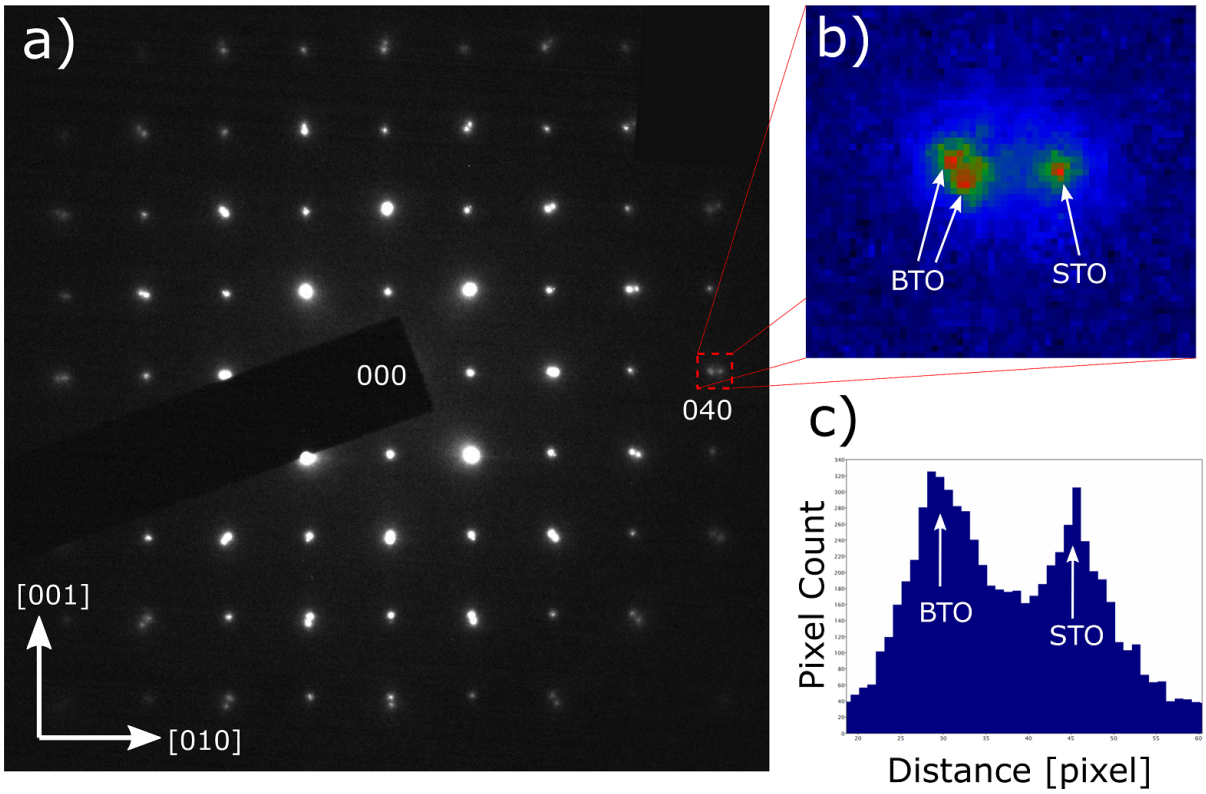

Figure 19: a) A SADP of STO and BTO. b) The 040 diffraction peaks of BTO and STO magnified, with a different color scheme. There is a clear distinction between the peaks. c) The intensity along a line profile, drawn through the BTO and STO peaks. By using line profiles the inter-peak distances could be determined with a few pixels uncertainty.

3.4.2 Scanning Convergent Beam Electron Diffraction

SCBED datasets were obtained on a JEOL-2100F TEM using an alignment procedure inspired by Hsiao [63] and Shao [64], and a scanning program written by Johnstone [65]. First, the beam is aligned with the specimen at the desired position. The scanning program moves the converged electron beam over a predefined specimen area using beam shift, acquiring a CBED pattern at each position. The scan start position is at the center of the scan area. Figure 20 a) shows a schematic of the scanning procedure. Five scans over areas of size 20 nm x 20 nm with step size 1 nm were acquired from the bulk of the film, approximately 30 nm from the film-substrate interface. Another five scans over areas of size 80 nm x 3 nm with step size 1 nm were acquired across the thickness of the film. Figure 20 b) visualizes how the scan areas were placed in the film.

The quality of the scanning procedure was evaluated by examining scanning sets from the STO substrate. Two scans over areas of size 200 nm x 15 nm with 5 nm step size approximately 0.5 μm from the film-substrate interface to test the scanning procedure. Three scans over areas of 8 nm x 8 nm with 1 nm step size were acquired from the STO substrate approximately 0.5 μm from the film-substrate interface to test the lattice parameter measurement algorithm (see section 3.5.3).

The acceleration voltage was 200 kV and the spot size was 0.5 nm. All CBED patterns were taken from a [001] ZA. The beam was tilted on axis with the specimen holder, and final adjustments were made by dark tilt.

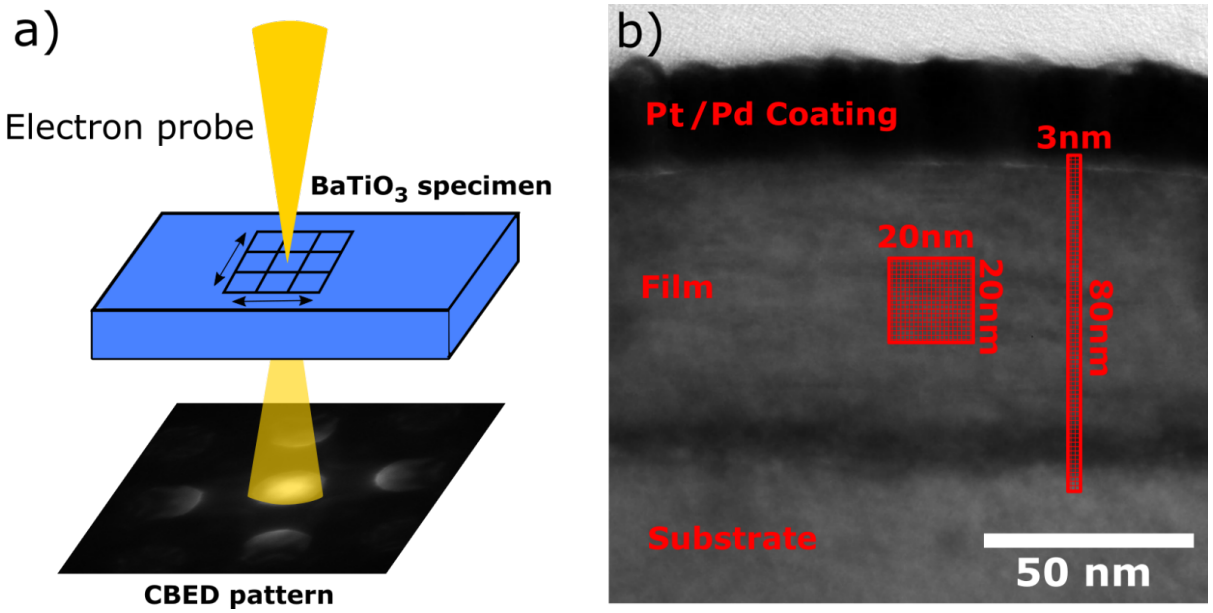

Figure 20: a) The SCBED scanning procedure uses beam shift to move the electron probe through a grid. At each grid point a CBED pattern is acquired. Figure adapted from Tsuda [11]. b) Five scans over areas of size 20 nm x 20 nm with step size 1 nm were performed in the bulk of the film. Another five scans over areas of size 80 nm x 3 nm with step size 1 nm were performed across the thickness of the film.

3.5 Data Processing

3.5.1 Symmetry Quantification Program

Inspired by the work of Kim and Zuo [13] a program was written in Digital Micrograph (DM) to evaluate the symmetry of CBED patterns. The program takes a stack of CBED images as input and evaluates the degree of symmetry of each CBED pattern by comparing pairs of discs on each side of the symmetry axis.

Figure 21 illustrates the process of quantifying the symmetry of a CBED pattern. First two CBED discs are selected about a mirror plane, as shown in Figure 21 a). The discs are rotated such that the mirror plane coincides with the vertical axis. To improve comparison of the selected areas, a circular mask is applied to filter out all intensity that is not contained in the disc. One of the discs is mirrored around the vertical axis. Should the discs be perfectly symmetrical around the given mirror axis the two images are now identical. Any difference in the two images can thus be used to quantify the degree to which they are asymmetrical. The sequence of image processing is visualized in Figure 21 b). The normalized cross-correlation coefficient γ is used to quantify the symmetry. The symmetry of the CBED pattern is evaluated over the symmetry axis parallel to the film-substrate interface, and for the symmetry axis perpendicular to the film-substrate interface. For each symmetry evaluation three pairs of discs are selected and compared, as shown in Figure 22 b) and c). The normalized cross-correlation coefficients for the mirror axis parallel to and perpendicular to the film-substrate interface are denoted $\gamma_{=}$ and $\gamma_{\perp}$, respectively. The process outlined in Figure 22 is repeated for all the patterns in a SCBED dataset. The metrics C, $\gamma_{=}$ and $\gamma_{\perp}$ are then plotted in a map. Examples of these maps are shown in Figures 22 d), e) and f).

The C-metric of each pattern was found by identifying the maximum intensity pixel in the 000 disc and applying equation 16. In the case of multiple maximum pixel values the program selects the first of the maximum pixels it encounters.

The script for producing symmetry maps from Scanning CBED datasets is given in the appendix B.

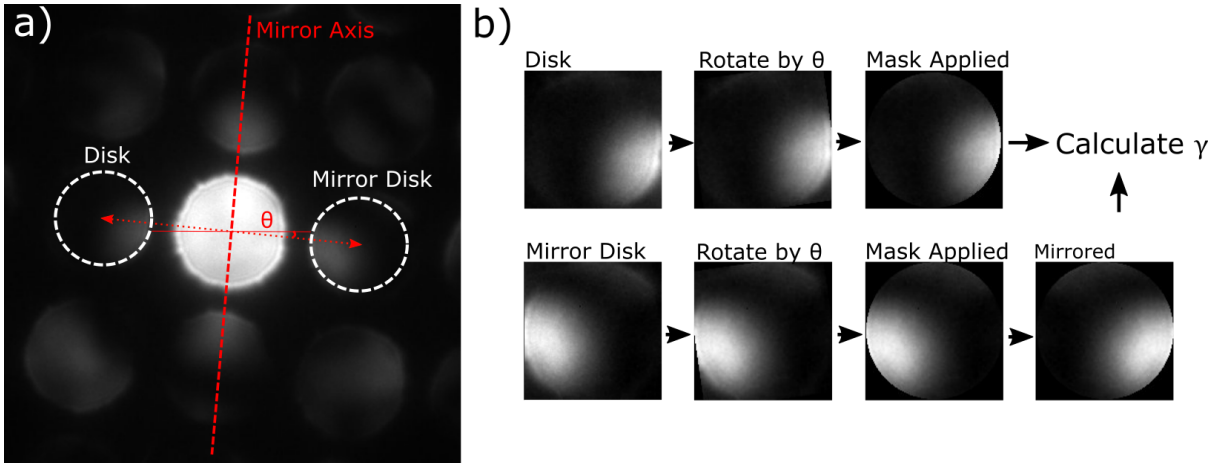

Figure 21: a) A CBED pattern with an indicated symmetry axis and two discs selected. To evaluate the symmetry of the pattern with respect to a mirror axis, corresponding discs on either side of the axis are selected and compared. The angle θ is the angle between the mirror plane and the vertical axis. b) Images outlining the processing steps necessary for acquiring γ values. First a circular mask is applied to the images of the discs, then they are rotated by θ such that the mirror axis is vertical. One of the discs is then mirrored around the vertical axis, and the discs images are compared to calculate γ. Image and procedure is inspired by Kim and Zuo [13].

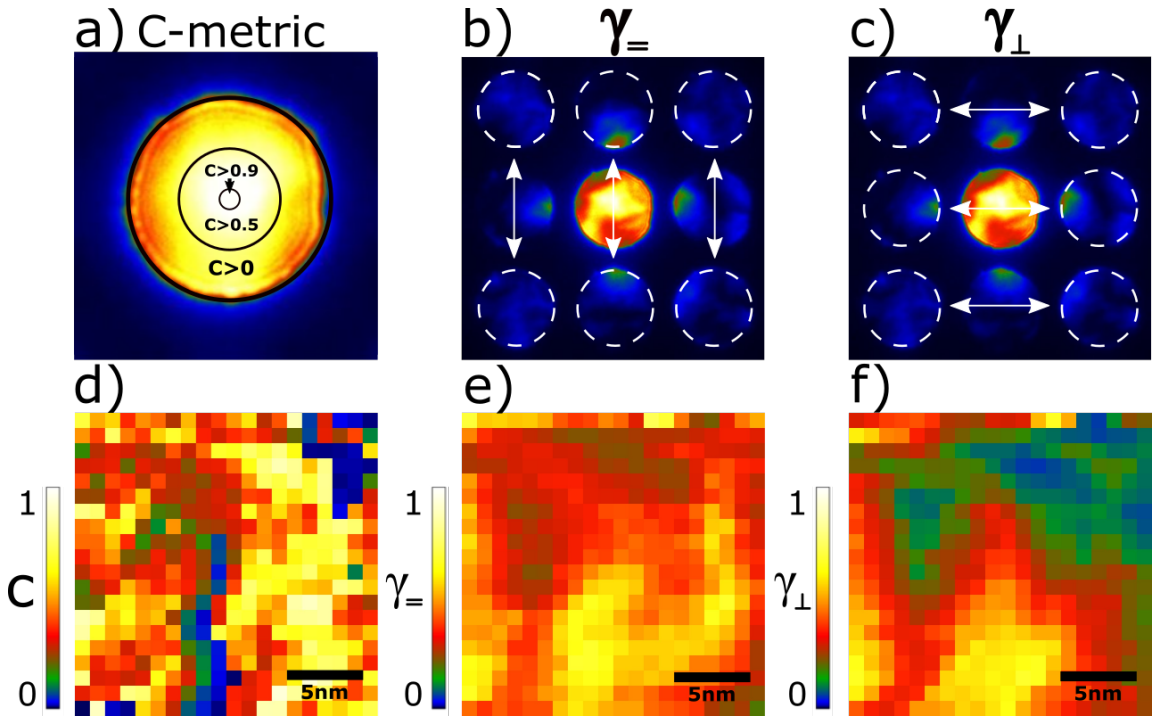

Figure 22: a) The C - metric is calculated for each CBED pattern. b) The metric $\gamma_{=}$ is calculated by comparing three pairs of discs across the symmetry axis parallel to the film/substrate interface. c) The metric $\gamma_{\perp}$ is calculated by comparing three pairs of discs across the symmetry axis perpendicular to the interface. d) After calculating the C-metric for all CBED patterns in the scanning set, a map is constructed, each pixel representing the C-metric of the CBED pattern at that location. e) The symmetry map containing $\gamma_{=}$ values. f) The symmetry map containing $\gamma_{\perp}$ values.

3.5.2 Lattice Parameter Measurement

The lattice parameter is obtained from a CBED pattern by measuring the distance between the centers of the discs. The centers of the CBED discs were identified by fitting circles around the edges of the discs, and finding the center of these circles. Before fitting circles to the CBED discs the images were processed to facilitate accurate fitting.

Figure 23 c) shows an excerpt of a CBED image. The edges of the discs have low contrast, giving a low precision to fitting a circle to the disc. This is mitigated by summing the CBED pattern from adjacent areas, producing a CBED pattern with enhanced edge contrast, as shown in Figure 23 d). The enhanced edge contrast comes at the cost of decreased spatial resolution. The area from which the CBED patterns are summed are selected from the $\gamma_=$ and $\gamma_\perp$ symmetry maps. Figure 23 a) and b) show two such symmetry maps, with the area containing the summed CBED patterns indicated. The summed CBED image is then further processed by application of the Canny Edge detection algorithm. Figure 23 e) shows the pattern after application of the algorithm. The edges of the discs are now clearly defined.

To minimize the error associated with manual fitting the whole pattern was overlaid with a grid with a fixed translation between discs. The grid was required to fit to all CBED discs in the pattern to minimize the measurement error. Figure 24 shows the grid fitted to a CBED pattern. The program Inkscape was used to make the grid and measure the inter-disc distances [66].

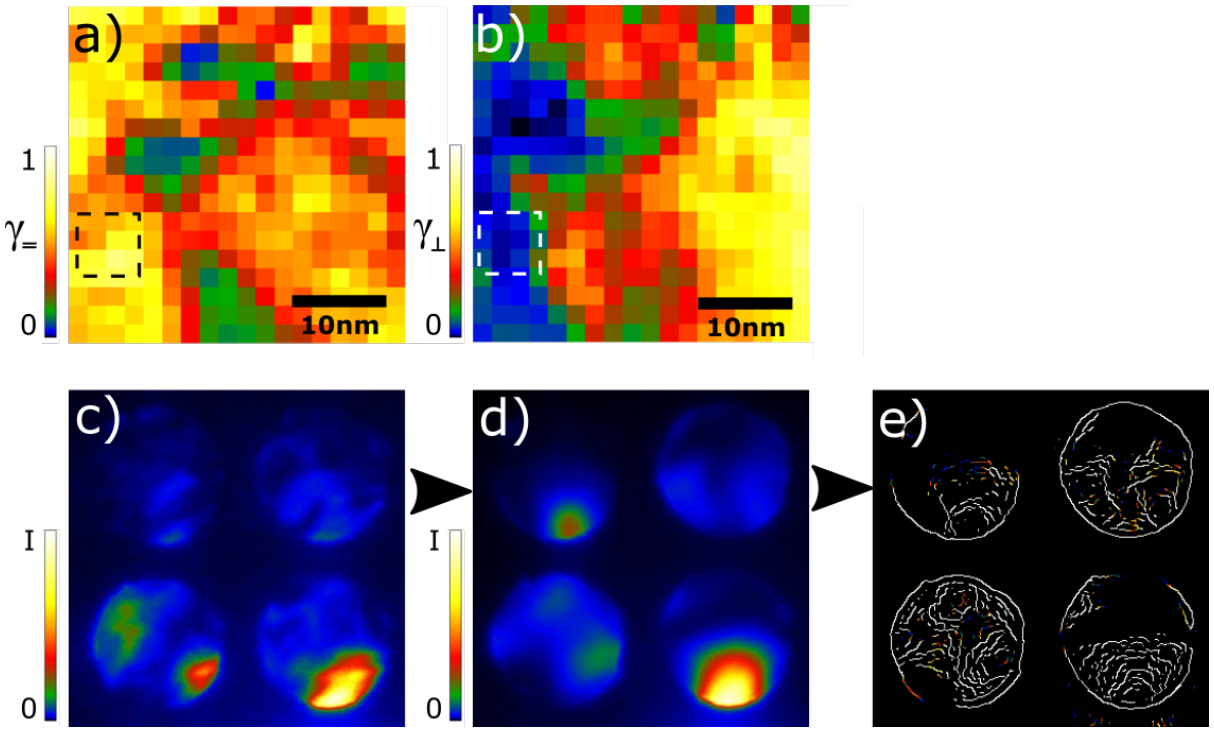

Figure 23: From a) and b), the $\gamma_=$ and $\gamma_\perp$ map evaluated of an area in BTO. An area with stable symmetry metrics is indicated in both maps. c) An excerpt of a single CBED pattern from the area indicated in a) and b). The contrast of the disc edges is poorly defined. d) An excerpt of a CBED pattern produced by summing together all patterns in the area of uniform symmetry as indicated in a) and b). The edges of the discs are better defined than in c). e) The image after application of the Canny edge detection algorithm, the edges of the CBED disc are now visible.

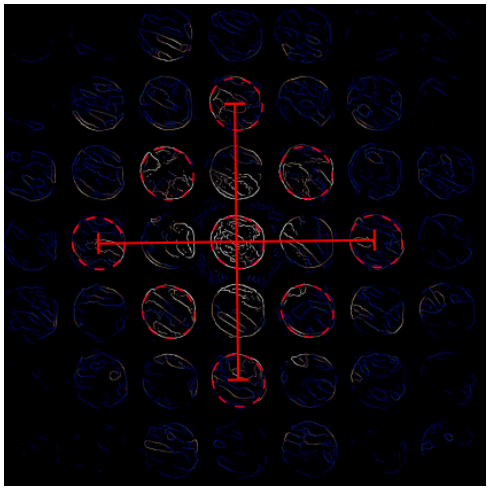

Figure 24: A grid is fitted onto the CBED patterns for higher accuracy measurements. The distance between discs is fixed and a fitting grid will therefore have to fit all the discs. The gamma and brightness values of the image have been enhanced to improve the visibility of the discs further away from the 000 disc.

3.5.3 Lattice Parameter Measurement by Algorithm

As the lattice parameter measurement method detailed in the previous section is labour-intensive, an algorithm to automate the lattice parameter measurements was implemented. This section will outline how the algorithm works.

Figure 25 gives a schematic representation of the main steps for extracting a lattice parameter measurement from a CBED pattern. First the Canny edge algorithm is performed on the CBED pattern (a), producing an image where only edges are outlined (b). The center disc is manually selected from this image, and masks are applied so that only the outer edge of the disc remains. This is the template (c). The template is cross-correlated with the image (b) producing a map of the cross-correlation coefficient (d). The local maxima of image d) correspond to the disc positions, and their positions are therefore stored (f). Masks are applied around each local maxima after selection to ensure that only maxima corresponding to CBED discs are selected (e). For lattice parameter calculation the distances along the [001] and [100] directions are of interest. The relevant distances are filtered out of the set of all inter-maxima distances by imposing several constraints (g). This process is repeated for all maxima (h) and the average distance between points is calculated from the set of distances found. For a scanning CBED set, this process is repeated for each pattern in a scan, and the measured lattice parameters and their standard deviations are output as maps. The template position is selected once and stored, allowing the program to automatically select the 000 disc of each pattern.

Three scans over areas of 8 nm x 8 nm with 1 nm step size were acquired from the substrate approximately 0.5 μm from the film interface to test the algorithm. All subsequent mentions of lattice parameter measurements by algorithm refer to measurements by the algorithm presented in this section. The code is given in appendix B.

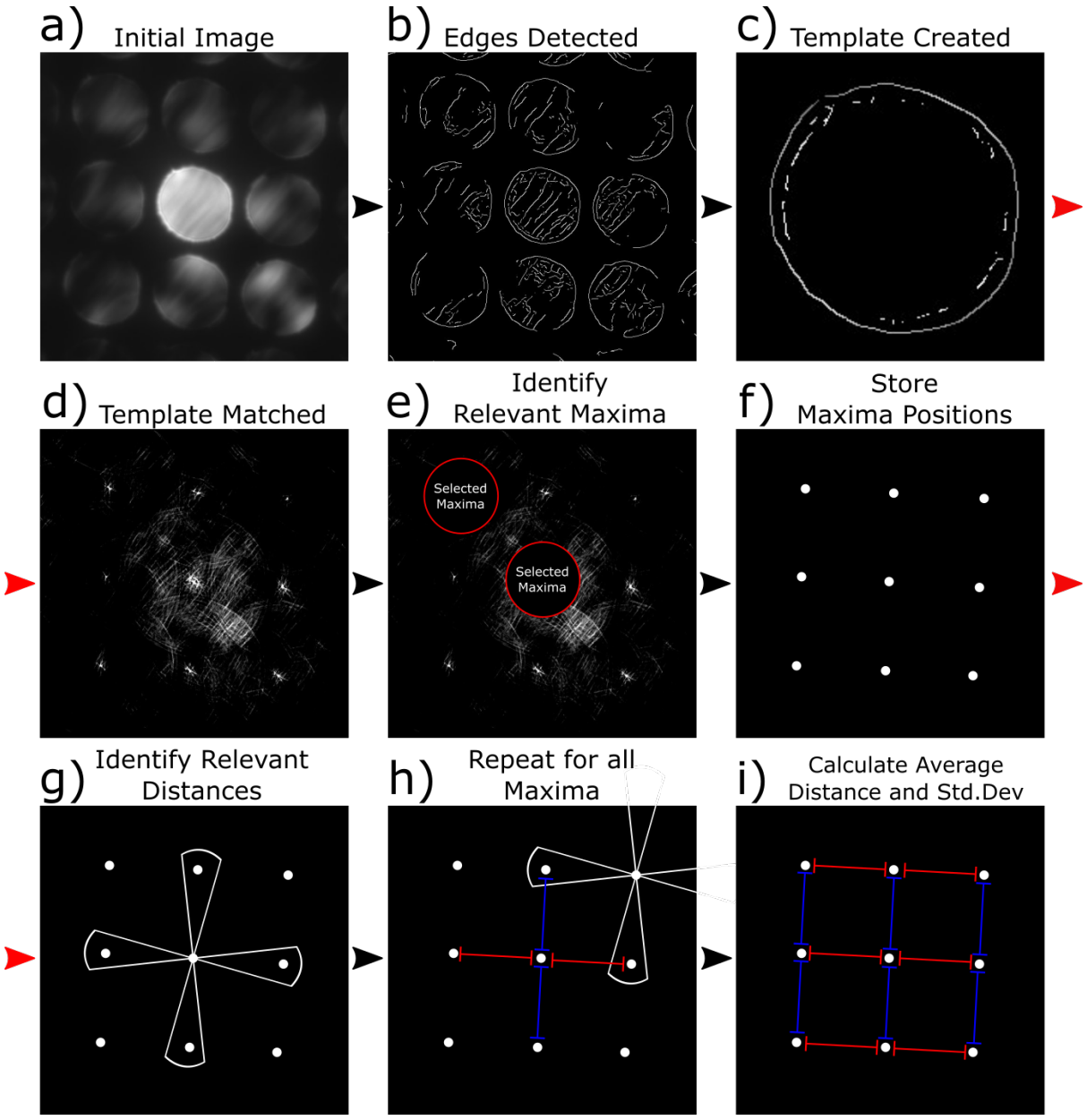

Figure 25: Image detailing the workflow of the algorithm. a) The initial CBED image. b) The initial image after application of the Canny edge detector. c) A template is created by applying masks to the 000 disc. d) The template is cross-correlated with image b) creating a cross-correlation map. e) The maxima corresponding to disc positions are identified. Masks are applied to avoid detecting maxima which do not correspond to CBED discs. f) The maxima positions are stored. g) Constraints are imposed on the inter-maxima distances, and the distances satisfying the constraints are stored. h) The process in g) is repeated for all inter-maxima distances. i) The average distance and the standard deviation of the measurements are calculated.

4 Results

In this section the results are presented. Section 4.1 presents BF images of the films annealed at 700°C and 1000°C. All subsequent results are acquired from the film annealed at 1000°C, as this was the specimen of main interest in this thesis.

Section 4.2 presents SADPs from the film, and the lattice parameters measured by SADP. Section 4.3 presents CBED patterns from the substrate and simulated CBED patterns to evaluate the symmetry quantification program. Section 4.4 presents simulated CBED patterns to show the effect of polarization and deviation from ZA on the symmetry of CBED patterns in single crystal BTO. Section 4.5 presents CBED patterns acquired from the film. Section 4.6 presents SCBED data acquired from the substrate, with the intention to evaluate the scanning procedure and the lattice parameter measurements by the algorithm. Finally, section 4.7 presents the SCBED data acquired from the film.

4.1 Bright Field Images

4.1.1 Polycrystalline Specimen

Figure 26 a) and b) show BF images of the film annealed at 700°C. The film consists of polycrystalline grains, and the average thickness of the film was found to be 55 ± 3 nm. The grains exhibit columnar growth, with most grains stretching from the substrate to the top of the film. The grain widths range from 20-70 nm. However, the main focus of this thesis was the specimen annealed at 1000°C, and the polycrystalline specimen will therefore not be discussed further.

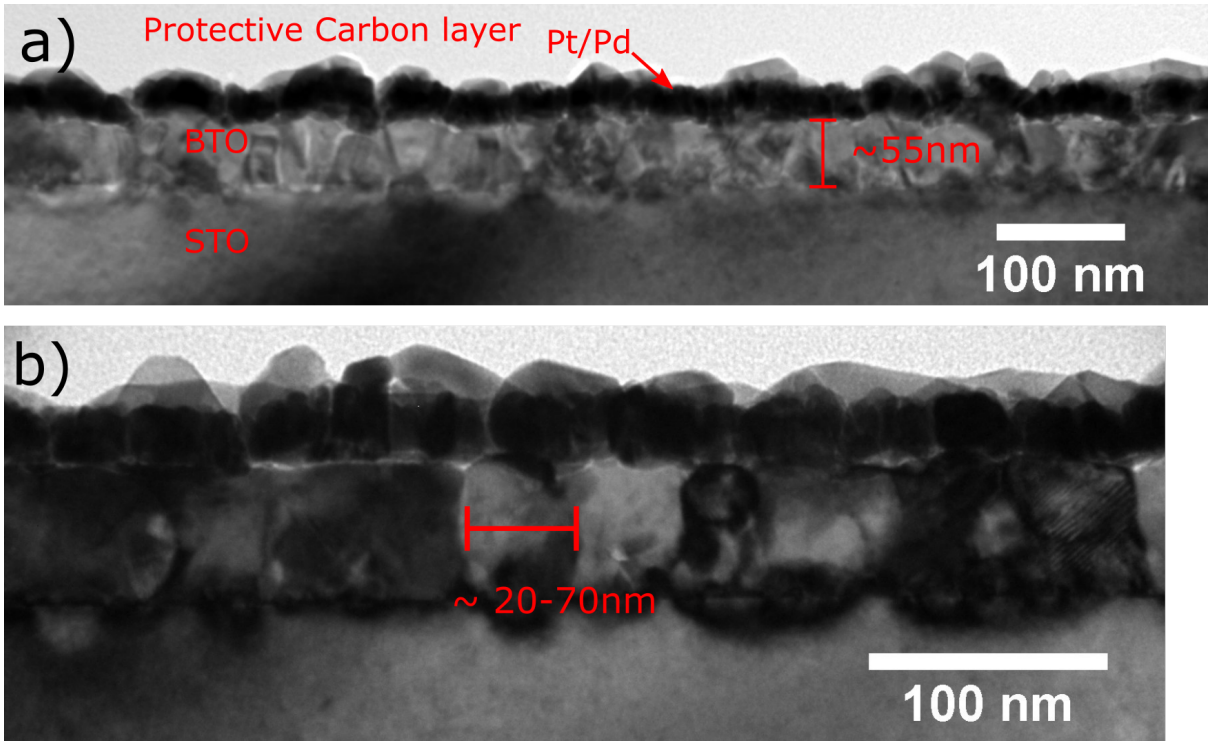

Figure 26: a) A BF of the polycrystalline thin film. The film is approximately 55 nm thick. b) A magnified BF image of the polycrystalline thin film. Most grains extend from the substrate to the top of the film. The grains vary in width from approximately 20-70 nm.

4.1.2 Epitaxial Specimen

Figure 27 shows BF images of the specimen annealed at 1000°C. The film exhibits epitaxial growth on the substrate. Figure 27 a) and b) show the TEM specimen section with thickness ≈ 75 nm and ≈ 130 nm in the beam direction, respectively. The film thickness is 60 ±5 nm. As is indicated in Figure 27, the film does not completely cover the substrate. Holes in the film, exposing the substrate to the Pt/Pd protective layer, were found throughout the film. In both a) and b) lines of contrast can be observed reaching from the substrate to the top of the film. Figure 28 a) shows a high magnification BF image of the film. The lines of contrast

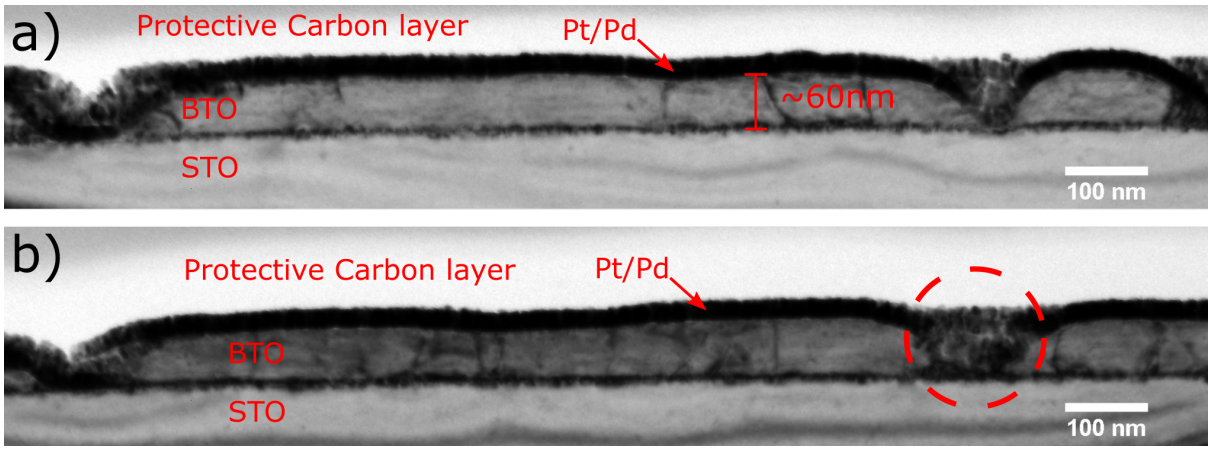

Figure 27: a) A BF image of the ≈ 75 nm thick section of the epitaxial specimen. b) A BF image of the ≈ 130 nm thick section of the epitaxial specimen. Indicated with a red ring is a section where the film is absent from the substrate, thus allowing the Pt/Pd coating to fill in the hole. The thicknesses refer to TEM specimen thickness.

are likely caused by dislocations, and have been indicated as such. Note that the dislocation lines predominantly form perpendicular to the film interface, or at an angle of about 45° with the interface. Spots of dark contrast appear periodically at the interface, with distances between spots ranging from 13 to 20 nm. Figure 28 b) shows a high-angle annular dark-field scanning TEM (HAADF-STEM) image of the interface of another BTO on STO film[1]. From Figure 28 c), which presents b) after applying a mask to the Fourier transform, it is clearly seen that the dislocations at the interface are edge dislocations.

[1]HAADF-STEM images taken by Inger Emma Nylund, from BTO on STO thin films thermally annealed at 1000°C. As the film synthesis was similar to the synthesis of the films studied in this thesis it is likely that the dislocations at the interface observed in Figure 28 a) look like the dislocations shown in Figure 28 b) in HAADF-STEM.

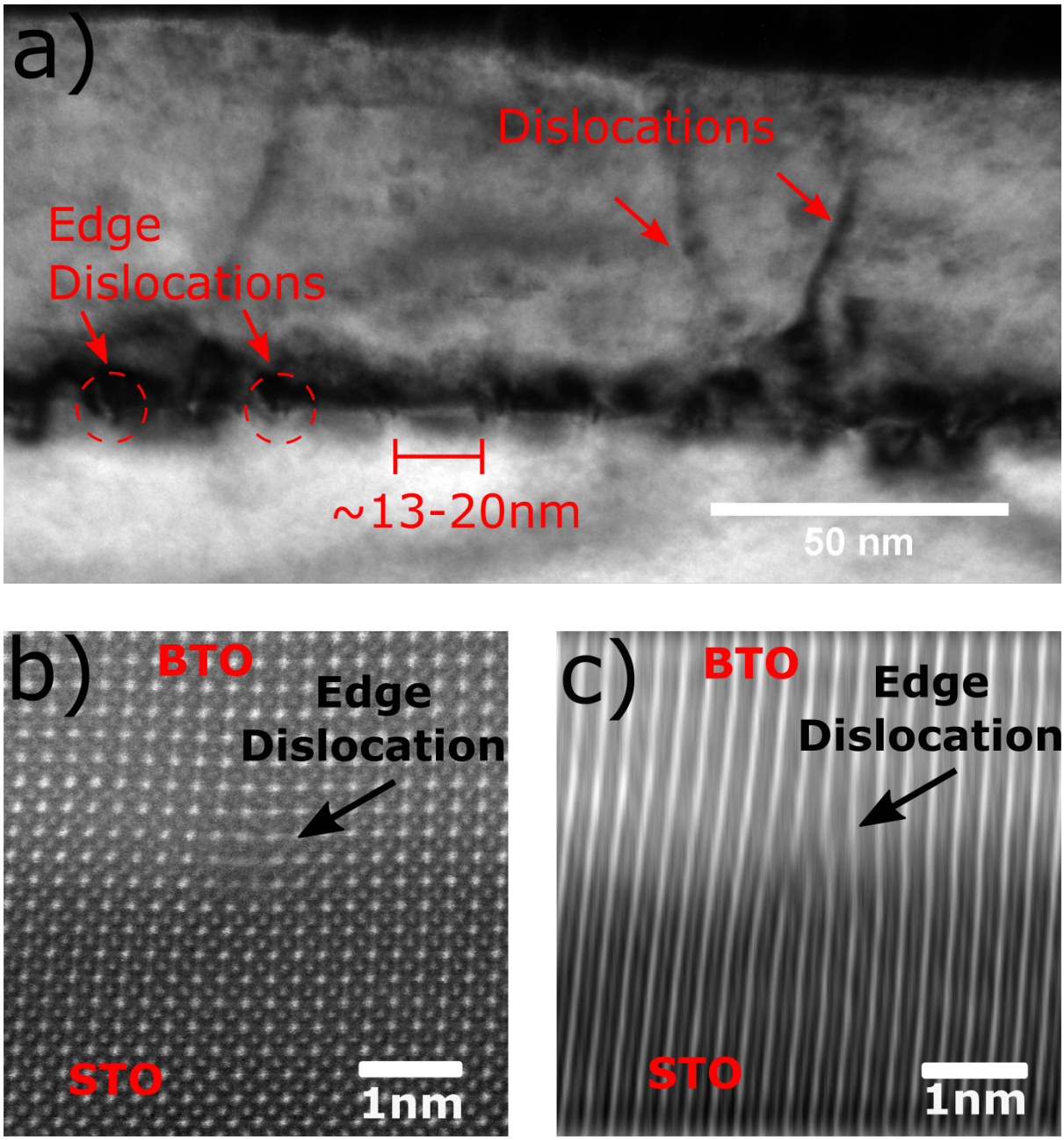

Figure 28: a) Magnified BF image of the epitaxial thin film. Dislocations are indicated with arrows. Edge dislocations and strain fields are visible at the interface. b) HAADF-STEM image of the film-substrate interface from a different BTO film on a STO substrate. An edge dislocation is visible on the interface. The film synthesis was similar to the synthesis of the films studied in this thesis, and the images therefore likely also represent how the edge dislocations in a) look in HAADF-STEM. Image courtesy of PhD Candidate Inger Emma Nylund. c) The edge dislocation becomes more visible after applying a mask in Fourier space.

4.2 Selected Area Diffraction Patterns

The areas of SADP measurement are marked in Figure 29 a). The lattice parameters calculated from the diffraction patterns are presented in Figure 29 b) with the nominal lattice parameters of tetragonal BTO indicated. The in-plane lattice parameter from these data ranges between 3.99 Å to 4.02 Å and the out-of-plane lattice parameter ranges from 4.00 Å to 4.03 Å. Figure 29 b) shows:

- The lattice parameters vary across the film.
- Both in-plane and out-of-plane lattice parameters lie between the expected lattice parameters of tetragonal BTO.
- The out-of-plane lattice parameter tends to be longer than the in-plane lattice parameter.

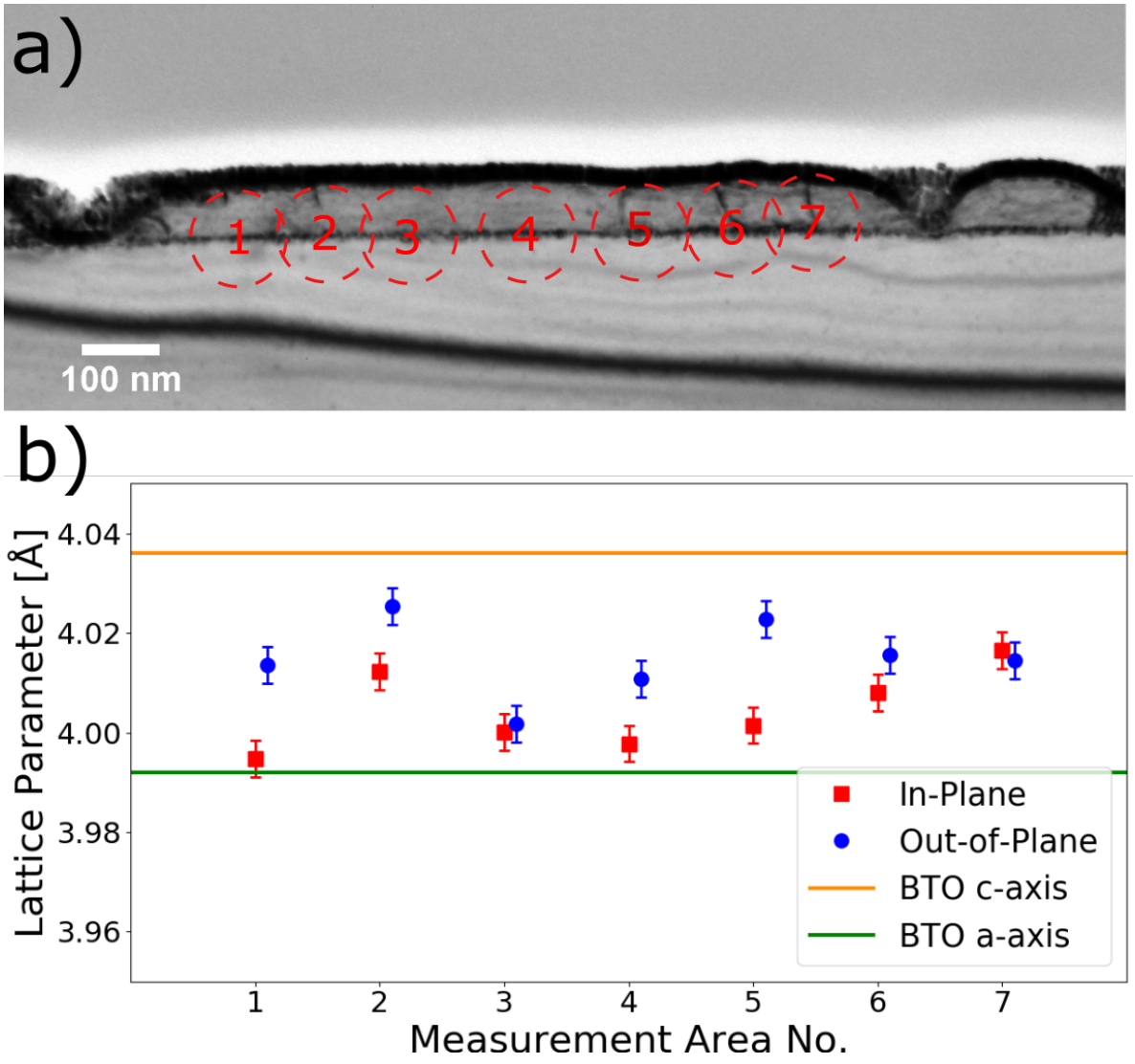

Figure 29: a) BF image of the thin film with the areas where SADPs were acquired indicated. b) Lattice parameters calculated from the SADPs of the areas shown in a). The SADP was calibrated using SADPs from the bulk STO substrate. The nominal lattice parameters of tetragonal BTO are indicated.

Figure 30 a) shows the SADP from area 7 in Figure 29 a). Figure 30 b) and c) show the BTO and STO peaks of the 034 and 040 reflections, respectively. From Figure 30 b) and c) we can conclude that:

- The BTO peaks are broader than the STO peaks.
- The BTO peaks are made up of multiple smaller peaks.
- The BTO peaks have different distances from the 000 peak, corresponding to different lattice parameters.
- Some BTO peaks do not lie on a straight line between the STO peaks and the 000 disc, corresponding to deviations from epitaxial growth.

Figure 30 is representative of the SADPs collected, as multiple and/or broad BTO peaks were found in most of the acquired SADPs.

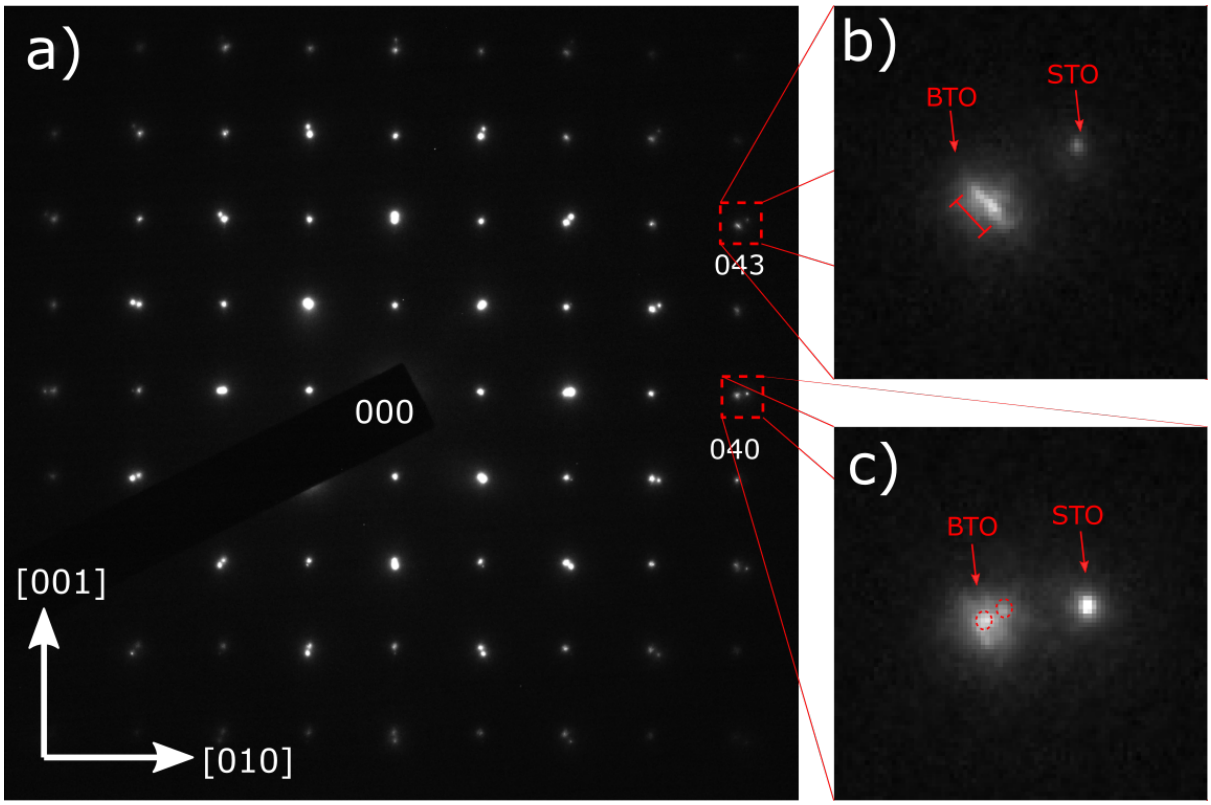

Figure 30: a) Figure showing an SADP obtained from the film. b) The 043 reflection shows that the BTO peak is extended, likely due to multiple orientations of BTO with respect to the substrate. c) The 040 reflection shows that BTO peaks have different distances from the 000 peak, corresponding to different lattice parameters.

4.3 Evaluation of Symmetry Quantification

This section presents CBED patterns acquired from the single crystal STO substrate and simulated STO CBED patterns that were used to evaluate the symmetry quantification program. Figure 31 a) shows a simulated CBED pattern from a 150 nm thick STO crystal along the [001] ZA. The symmetry quantification program finds perfect symmetry along the horizontal and vertical axes, $\gamma_{\perp} = \gamma_{=} = 1$, as expected. The C-metric is 0.98, which means slightly off center. Figure 31 b) shows an experimental STO pattern obtained from the substrate along the [001], with $\gamma_{\perp}$ and $\gamma_{=}$ = 0.99, and a C of 0.92.

To test the robustness of the symmetry quantification for experimental patterns, γ and C values were measured from 9 different experimental STO patterns aligned on the [001] ZA. The average γ value was found to be 0.95 ± 0.05. The average C was 0.91 ± 0.04.

To estimate the uncertainty associated with manual disc selection, five measurements of $\gamma_{\perp}$ and the C were performed on the same pattern (see Figure 31 b). The measurements resulted in a C of 0.929 ± 0.006 and a $\gamma_{\perp}$ of 0.985 ± 0.005.

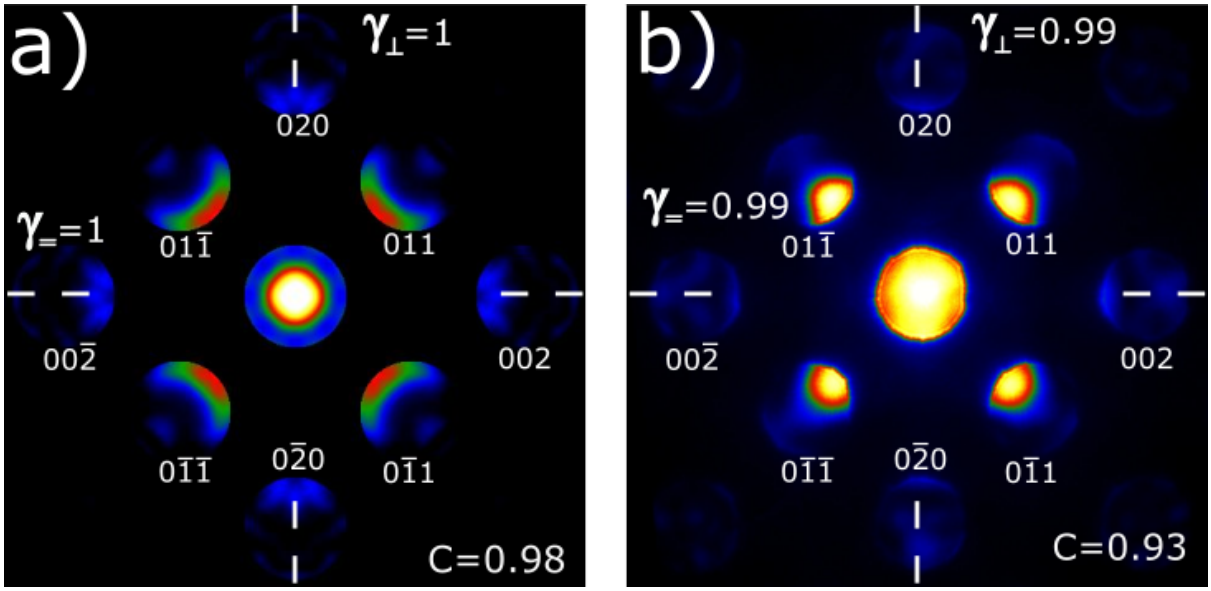

Figure 31: a) Simulated CBED pattern of STO with beam direction in the [100] ZA. The γ values indicate perfect mirror symmetry, while the C indicates the maximum intensity is close to the center of the 000 disc. This shows that the symmetry quantification program is able to detect symmetry. b) An experimental CBED pattern from STO with beam direction along the [100] ZA. The γ symmetry values show a high degree of mirror symmetry for the horizontal and vertical mirror planes. The C-metric indicates that the maximum intensity is close to the center of the 000 disc. This shows that the symmetry quantification program is able to detect symmetry in experimental patterns, and that alignment resulting in high symmetry CBED patterns is possible.

4.4 Simulated CBED

This section presents the simulated CBED patterns. Throughout this section out-of-plane and in-plane refer to the paper as the plane, as is visible from the figures. Throughout the section the 000 discs presented have a different image correction γ-factor (not to be confused with the $\gamma_=$ and $\gamma_\perp$ symmetry metrics) than the rest of the image to better highlight features of interest.

Figure 32 a) and b) show CBED patterns of BTO for out-of-plane and in-plane polarization, respectively. From Figure 32 we can learn that:

- From b) the asymmetry is most visible in the ±001 discs along the polarization direction.
- From b) the asymmetry introduced by in-plane polarization is very small. $\gamma_\perp$ = 0.99 corresponds to a high degree of symmetry.
- The center disc is highly centrosymmetric in both figures, with a single intensity maxima in the middle (C=0.99 for both a and b).

CBED patterns of BTO with in-plane polarization for different thicknesses are presented in Figure 33, with the asymmetry indicated. From Figure 33 we can learn that:

- The discs in which the asymmetry is most pronounced vary for differing thicknesses.
- The high $\gamma_\perp$ values indicate that the asymmetry introduced by polarization is very small for thicknesses between 50 - 150 nm.
- The intensity maxima of the 000 disc is in the disc center for specimen thicknesses 50, 75 and 100 nm, whereas it lies a bit off center for thickness 150 nm.

Further simulations show that the intensity maxima of the 000 disc remains in the disc center for specimen thicknesses up to 130 nm.

There will always be some amount of misalignment between the electron beam and the ZA of the BTO crystal, introducing an additional source of asymmetry in the CBED pattern. It is therefore important to be aware of how misalignment changes CBED patterns to distinguish between asymmetry caused by polarization and asymmetry caused by misalignment. Assuming the BTO has either in-plane or out-of-plane polarization, and the beam can be either on-zone or off-zone, there are 4 possibilities:

- The BTO is out-of-plane polarized and the beam is correctly aligned.
- The BTO is in-plane polarized and the beam is correctly aligned.
- The BTO is out-of-plane polarized and the beam is misaligned.
- The BTO is in-plane polarized and the beam is misaligned.

The first two instances were simulated in Figure 32 a) and b), and were shown to produce a symmetric and an asymmetric pattern, respectively. The following section will examine the two last cases, the effect of misalignment on CBED patterns for out-of-plane and in-plane polarization. Subsequent simulations are performed on specimens of thickness 75 nm, as this film thickness was found to be best suited for acquiring experimental CBED patterns.

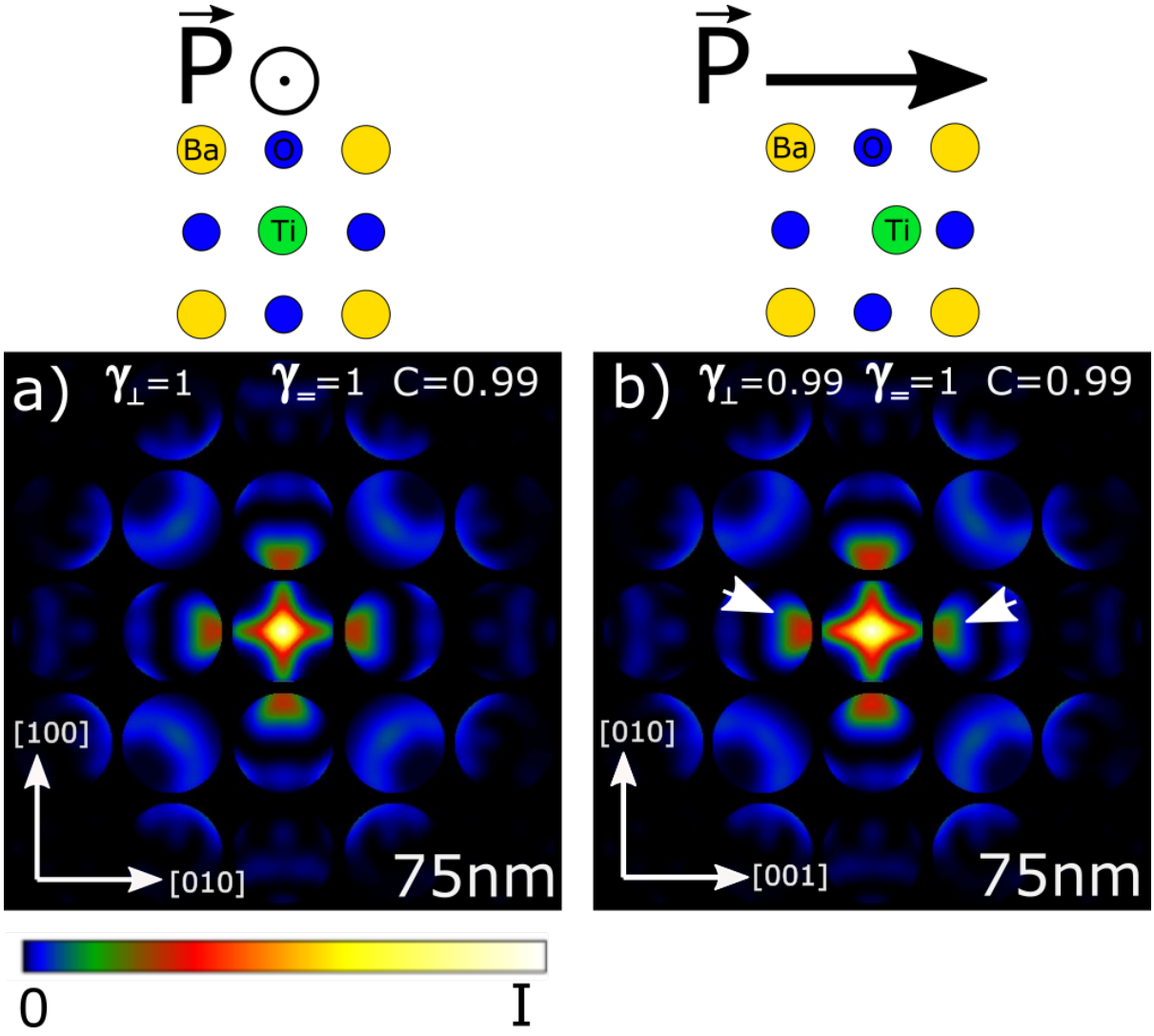

Figure 32: a) A Bloch wave simulation of a 75 nm thick BTO crystal, with the incident beam direction in the [001] ZA. The polarization direction is out-of-plane. The BTO crystal is symmetric in this direction, which is also reflected in the CBED pattern. b) A simulation with incident beam direction in the [100] ZA. The polarization direction is in-plane. This creates an asymmetry in the CBED discs, most visible in the ±001 discs. Visible asymmetry is indicated by arrows.

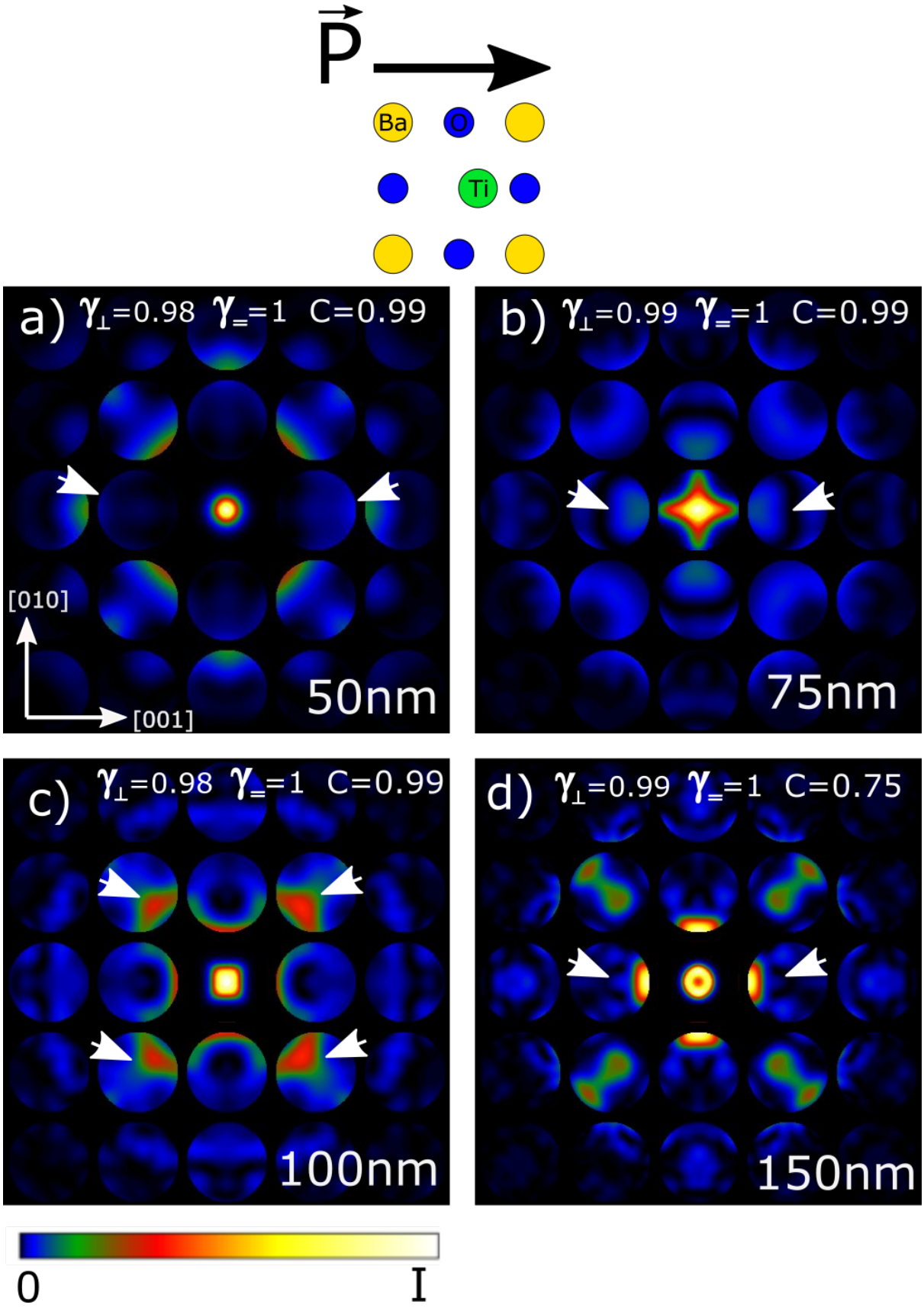

Figure 33: a), b), c) and d) show Bloch wave simulations of CBED patterns produced by an incident beam direction in the [100] ZA of the BTO, for different thicknesses. The thickness is presented in the bottom right corner of each pattern. The polarization direction is in-plane. The figures illustrate that discs which contain the most prominent asymmetry vary for different thicknesses. Visible asymmetry is indicated by arrows.

4.4.1 Effect of Beam Misalignment on CBED

Figure 34 a), b) and c) show CBED patterns acquired from BTO with out-of-plane polarization, with the beam tilted at 0.1°, 0.05° and 0.01° off the [001] ZA , respectively. From Figure 34 we can see that:

- Beam misalignment introduces asymmetry in the mirror planes that contain the axis of rotation, measured by $\gamma_{\perp}$.
- In a), beam misalignment introduces a large asymmetry in the center disc, indicated by the low *C* value.
- From a), b) and c) it is seen that the asymmetry increases for increasing misalignment.

From these observations it follows that the asymmetry induced by misalignment in can be distinguished from asymmetry induced by polarization by investigating whether the 000 disc is centrosymmetric or not.

Figure 35 b), c) and d) show CBED patterns from an area with in-plane polarization, for beam misalignment of 0.01° for three different rotations. The beam direction was either rotated away from the polarization vector, towards the polarization vector or perpendicular to the polarization vector. Figure 35 a) includes the CBED pattern for the beam being perfectly on-zone for quick reference. Inspecting Figure 35 it is seen that:

- From a) the ±010 and ±001 discs all have a mirror axis across.
- From b) and c), misalignment causes the mirror axes of the ±010 and ±001 discs to break.
- Beam misalignment causes asymmetry in the center disc.
- For an aligned beam and in-plane polarization the center disc is highly centrosymmetric.

From these observations it follows that it is theoretically possible to distinguish asymmetry induced by polarization from asymmetry induced by misalignment by investigating the mirror axes across the discs.

To clarify, the mirror axes indicated in Figure 35 refer to the mirror axes with respect to the single discs. As an example, the mirror axes in Figure 35 a) are meant to indicate that each individual disc could be flipped around its mirror axis and be virtually unchanged. This is not in conflict with the observation that the mirror axis of the whole pattern $\gamma_{\perp}$ is not equal to 1.

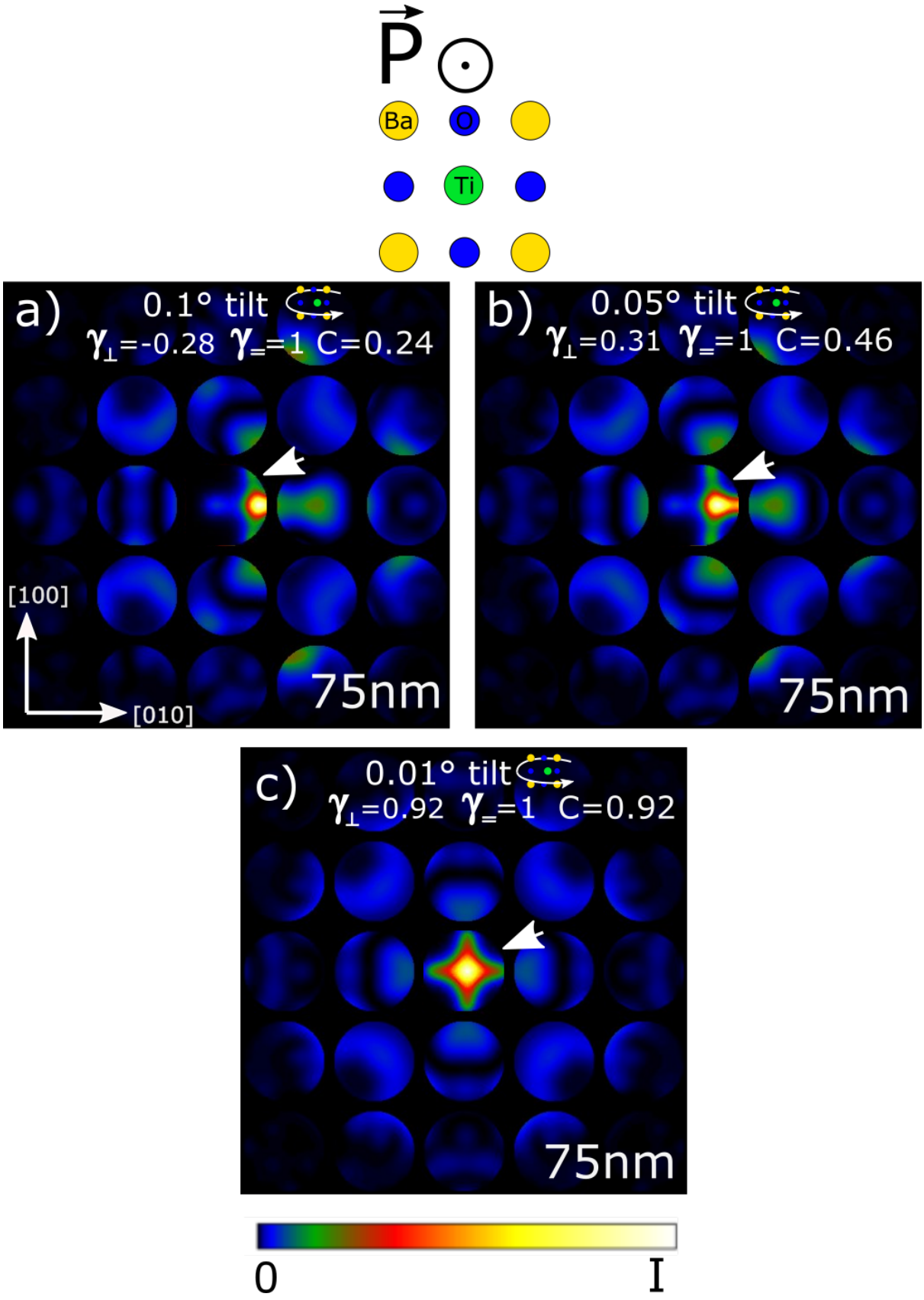

Figure 34: a), b) and c) show Bloch wave simulations of CBED patterns produced by a beam incident on the [001] ZA of the BTO crystal for different beam misalignment. The polarization is out-of-plane, which means the patterns would be symmetric if the beam was aligned perfectly on ZA. The figures illustrate that even small misalignment produces an asymmetry in the center disc, with the asymmetry becoming more pronounced for larger deviations from the ZA. The asymmetry is indicated by arrows.

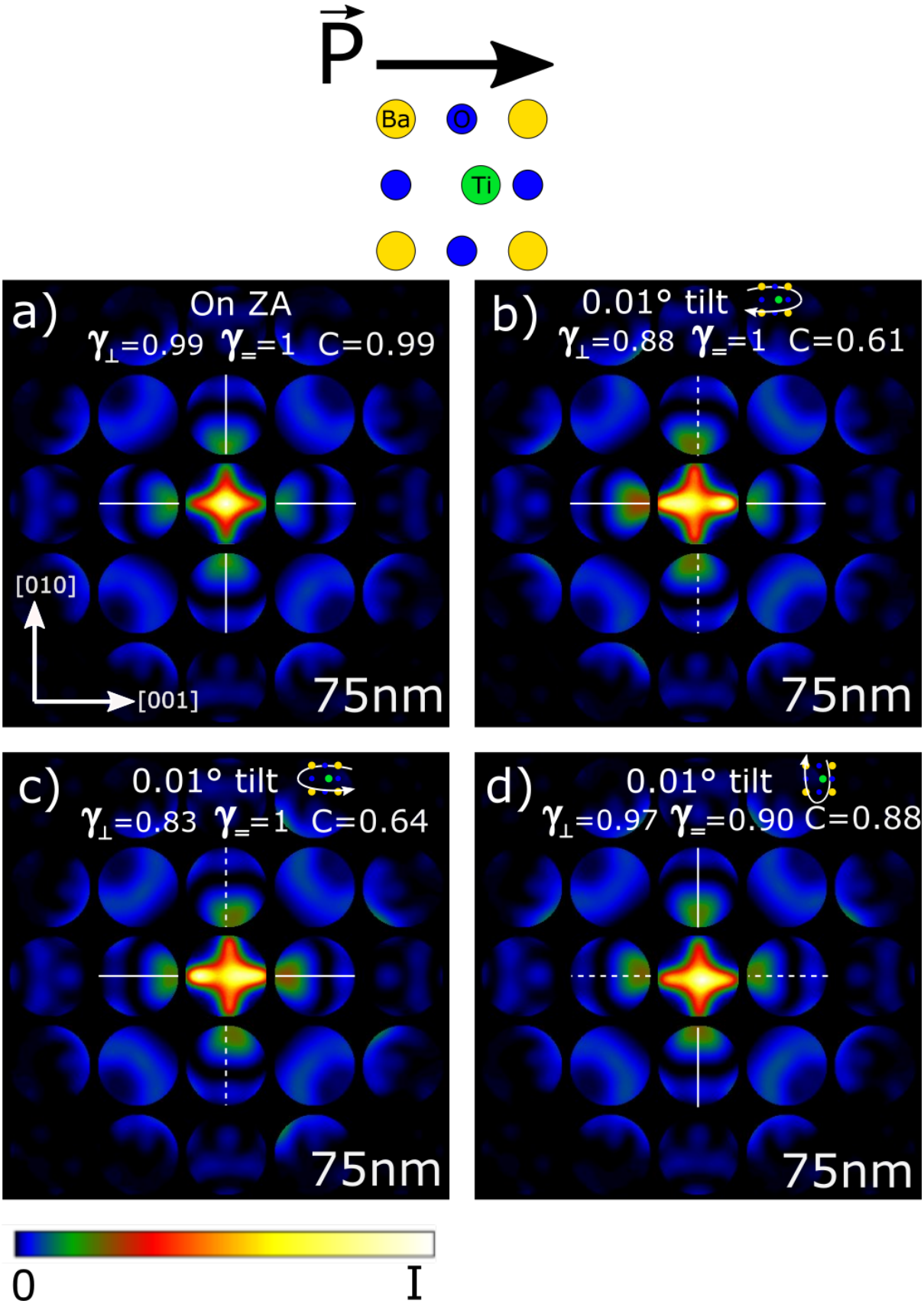

Figure 35: Simulations with the beam incident on the [100] ZA of BTO. a) The beam is aligned on zone. The ±010 and ±001 discs have mirror axes across, as indicated. b), c) and d) show simulations of the same system as a) but with a 0.01° misalignment along the axes indicated in the figures. The mirror axes in the ±010 and ±001 discs are broken upon misalignment, as indicated in the figures. This can be used to distinguish asymmetry induced by misalignment from asymmetry induced by polarization.

4.5 CBED from the BTO Film

The following results were acquired from the BTO specimen section of thickness ≈75 nm. Figure 36 a) shows a representative CBED pattern acquired from the middle of the film, approximately 30 nm from the film-substrate interface. The conclusions drawn from Figure 36 a) are:

- The maximum intensity of the 000 disc is located in the middle of the disc, indicated by C=0.95.
- The intensity distribution in the 000 disc is not centrosymmetric.
- The surrounding discs do not have as high symmetry as expected from the simulations, indicated by the low $\gamma_{=}$ and $\gamma_{\perp}$ values.

CBED patterns where the 000 disc has non-centrosymmetric intensity distributions are representative for all CBED patterns acquired from the BTO-film. In these areas no beam alignment was found where the patterns had the degree of symmetry expected from the simulations.

Figure 36 b) shows another class of representative CBED patterns, found predominantly in the thicker sections of the specimen and at the film-substrate interface. These are more disordered than the patterns in Figure 36 a). In these areas it was not possible to align the beam such that the pattern resembled something symmetric.

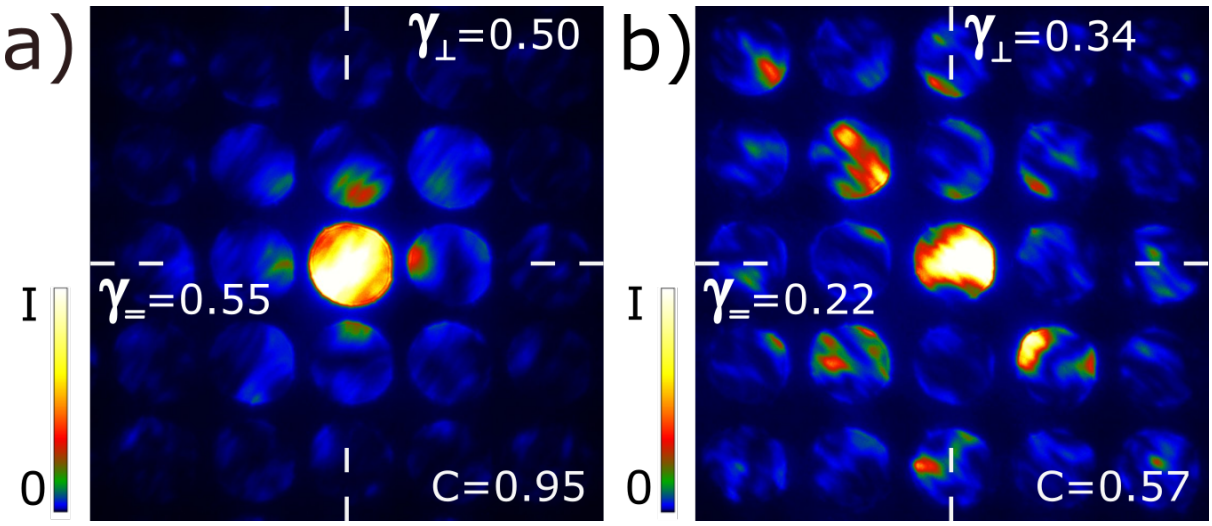

Figure 36: a) A representative CBED pattern from the middle of the film. The highest intensity maxima is located in the middle of the 000 disc. The intensity distribution in the 000 disc is not symmetric. b) A CBED pattern representative of the patterns found close to the film-substrate interface and thicker film regions. The pattern is highly disordered and no alignment was found that increased the symmetry of the pattern.

4.6 SCBED from the STO Substrate

Section 4.6.1 presents the symmetry maps computed from SCBED datasets acquired from the STO substrate. These were used to evaluate the scanning procedure. Section 4.6.2 presents lattice parameters computed by the algorithm from SCBED datasets, acquired from the STO substrate. These were used to evaluate the algorithm. Throughout the section the term out-of-plane and in-plane refer to the film-substrate interface as the plane.

4.6.1 Symmetry Maps

The scanning procedure was evaluated on SCBED datasets from the single crystal STO substrate oriented in the [001] ZA. The scanning CBED patterns tested were acquired from two areas of dimension 200 nm x 15 nm. Figure 37 a) shows a BF of STO with the scan areas and scan start position indicated. A CBED pattern is inlaid showing the substrate orientation. From Figure 37 it can be seen that:

- From b) and d) it is seen that the C-metric decays towards zero for patterns taken far away from the scan start position.
- From c) and e) it is seen that the γ metrics decay when the scan moves in the direction perpendicular to their symmetry axis.
- An area of about 20 nm x 20 nm around the scan start position has both high C-metric and high γ values.

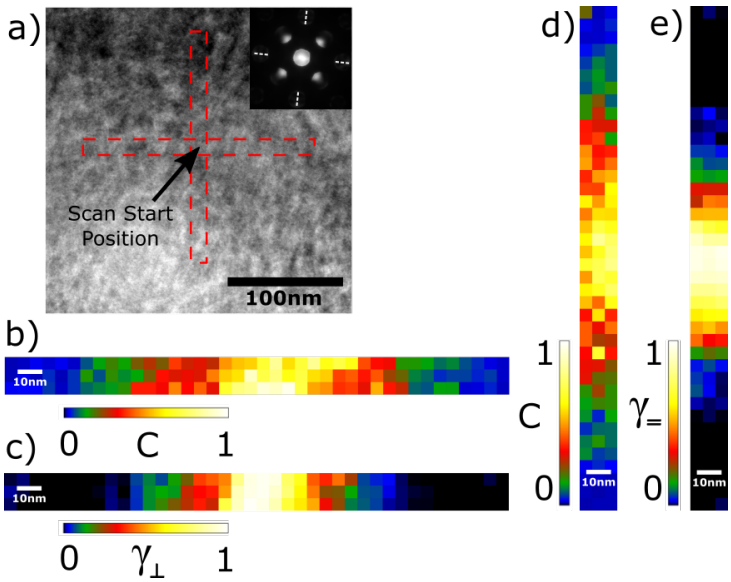

Figure 37: SCBED scans from the substrate were used to evaluate the scanning procedure. a) A BF of STO with the scan areas and the scan start position indicated. The scan areas have dimensions 200 nm x 15 nm. A CBED pattern is inlaid to show the specimen orientation. b), c), d) and e) show symmetry maps of $\gamma_\perp$, $\gamma_=$ and the C-metric. The maps show that the symmetry of the outer and center discs deteriorates as the beam moves away from the scan start position. These maps show that a feasible area to perform scans is about 20 nm x 20 nm around the scan start position, as this reduces beam-specimen misalignment caused by the scanning procedure to a minimum.

The STO in the substrate is manufactured as a single crystal, and the STO unit cells are therefore assumed to be cubic with mirror planes such that $\gamma_{=}$=1 and $\gamma_{\perp}$=1. Any asymmetry in CBED patterns acquired from the substrate is therefore expected to be caused by beam-specimen misalignment. Figure 38 a) and b) show a simulated STO CBED pattern with 0.05° misalignment and a CBED pattern acquired 60 nm from the scan start position. Considering the resemblance of the patterns, it seems likely that the cause of the asymmetry is beam-specimen misalignment. Within an area of 20 nm x 20 nm around the scan start position the patterns exhibit strong symmetry, that is the γ values are over 0.90 and the *C*-metrics are over 0.75. To avoid excessive beam-specimen misalignment, scans for symmetry quantification should therefore be performed in a maximum area of 20 nm x 20 nm with this setup.

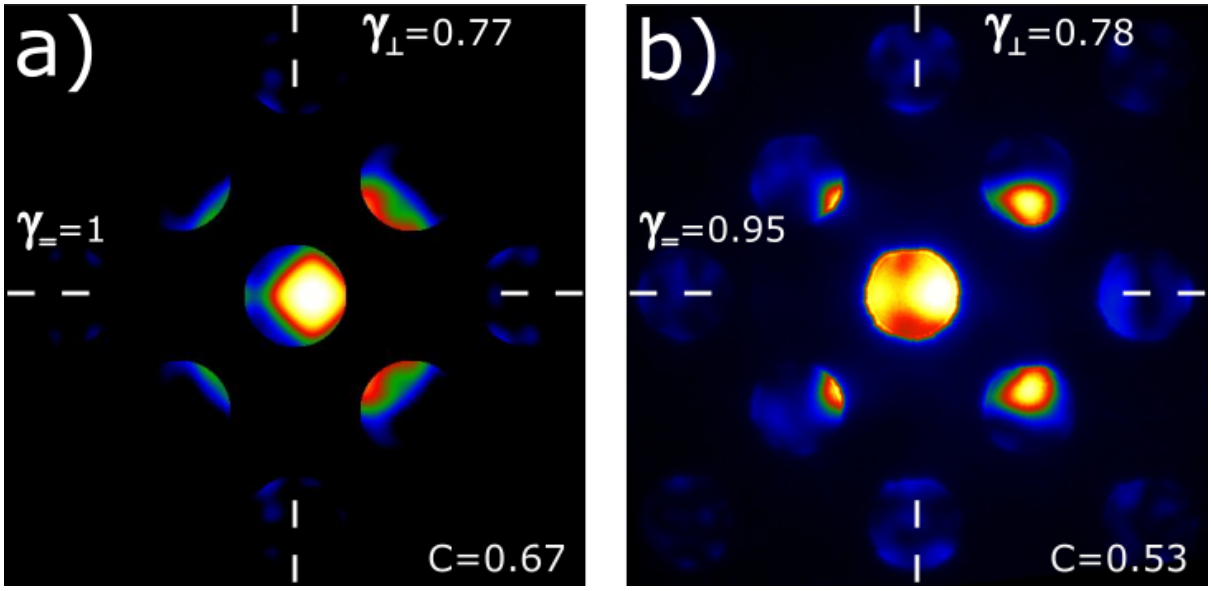

Figure 38: a) Simulated CBED pattern of STO with beam direction along the [100] ZA and a beam misalignment of 0.05°. The intensity distribution of the center-disc is not centrosymmetric, and the symmetry of the outer discs is broken in the direction of misalignment. b) An experimental CBED pattern from STO taken from a scanning set. The pattern was acquired 60 nm away from the scan start position. The observed asymmetry resembles the asymmetry induced by misalignment in a). This suggests that the scanning procedure induces beam-specimen misalignment.

4.6.2 Lattice Parameter Maps

The lattice parameter algorithm was tested on the STO single crystal substrate aligned on the [001] ZA. Figure 39 a) and b) show in-plane and out-of-plane lattice parameters, respectively, of an 8 nm x 8 nm scan as measured by the template-matching algorithm. From a) and b) it is seen that the measured lattice parameters vary within a range of ±1.5 pm. The cause of this variation may be inaccuracies associated with the algorithm, or inhomogeneity in the substrate. Figure 39 c) and d) show the standard deviation of the measurements of the in-plane and out-of-plane lattice parameters, respectively. From c) and d) it is seen that the standard deviation of the lattice parameters ranges from 0-2 pm. c) and d) are representative of multiple datasets in that the out-of-plane lattice parameter has a higher standard deviation than the in-plane lattice parameter. Figure 39 shows that the algorithm can determine lattice parameters with picometer precision. As the algorithms STO measurements were deemed more precise than the manual measurements, the STO lattice parameter measurements were used for calibration.

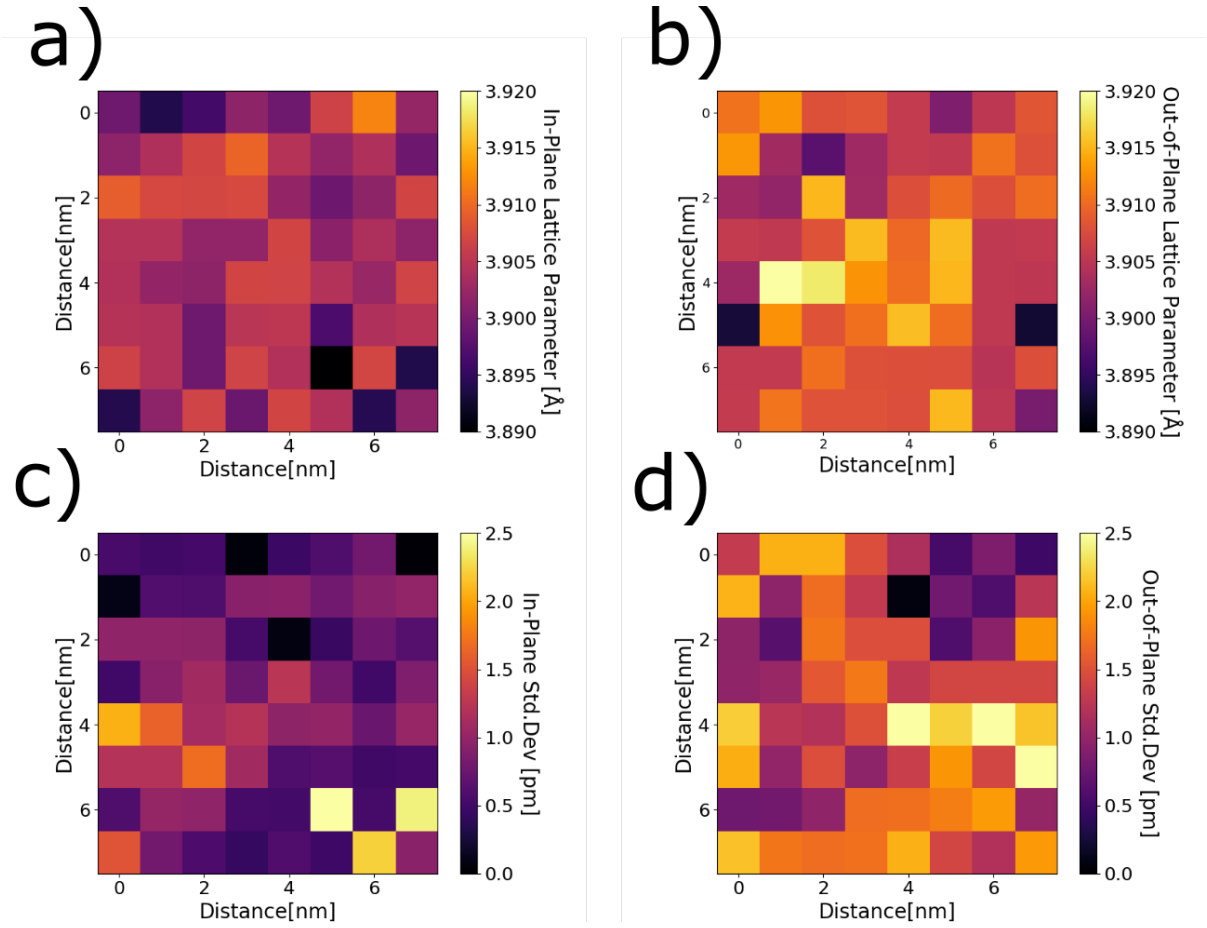

Figure 39: SCBED results from an 8 nm x 8 nm scan in the STO substrate. a) and b) show maps of the in-plane and out-of-plane lattice parameters as measured by the algorithm, respectively. c) and d) show maps of the standard deviations associated with the measurements. From c) and d) we see that the algorithm can measure the lattice parameter with picometer precision in the single crystal STO substrate.

4.7 SCBED from the BTO Film

Section 4.7.1 presents the symmetry maps computed from SCBED datasets from the BTO film. Section 4.7.2 presents the lattice parameter measurements computed from SCBED datasets from the film. The datasets from the 20 nm x 20 nm scans are presented first, followed by the datasets from the 80 nm x 3 nm scans. Throughout the section the term out-of-plane and in-plane refer to the film-substrate interface as the plane. In some figures datapoints with high uncertainty are not presented (see section 5.2.4 for justification).

4.7.1 Symmetry Maps

Figure 40 shows data produced from one of the 20 nm x 20 nm scans, acquired in the BTO film approximately 30 nm from the film-substrate interface. See Figure 20 a) for a representation of the scan position. Figure 40 a) , b) and c) show the maps of C, $\gamma_{=}$ and $\gamma_{\perp}$ respectively. Figure 40 d) shows the manually measured lattice parameter from the areas indicated in a), b) and c).

Figure 40 shows:

- Areas 1 to 3 have similar lattice parameters, but different symmetry metrics C and γ.
- Areas 3 and 6 have similar symmetry metrics C and γ, but different lattice parameters.

From these observations it follows that the symmetry metrics are not correlated with the lattice parameters. This is representative for what was found when comparing symmetry metrics and lattice parameters of the five 20 nm x 20 nm scans.

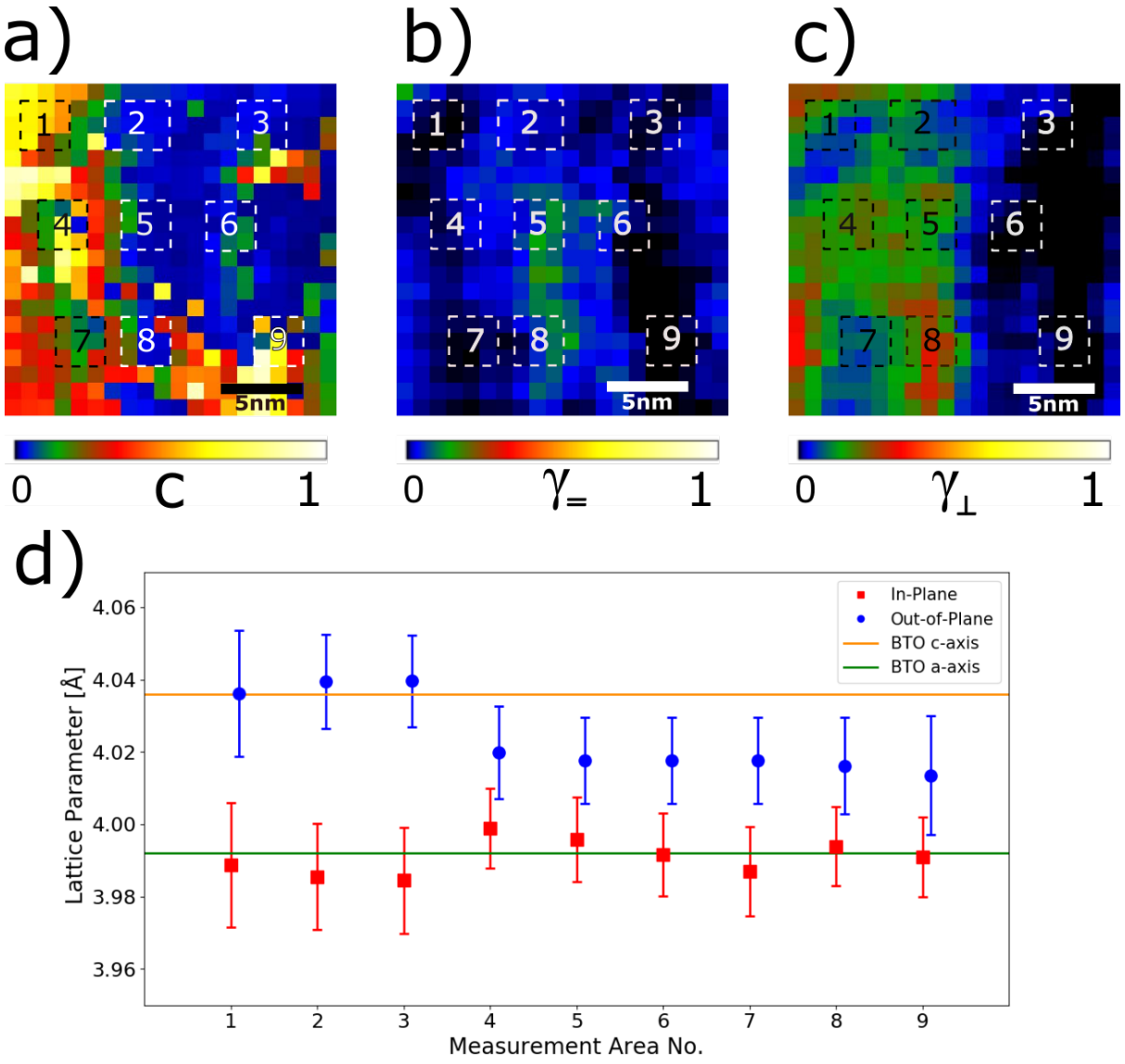

Figure 40: SCBED results from a 20 nm x 20 nm scan in BTO. a) A map of the C-metric for all CBED patterns in the scan. b) A map of $\gamma_{=}$ for all CBED patterns in the scan. c) A map of $\gamma_{\perp}$ for all the CBED patterns in the scan. The areas marked in a), b) and c) were used for manual measurements of the lattice parameter. d) The lattice parameters measured manually from the CBED patterns of the marked areas. From this we see that the lattice parameter, and thereby the polarization, is not correlated with the symmetry metrics.

4.7.2 Lattice Parameter Maps

Figure 41 shows data produced from one of the 20 nm x 20 nm scans, taken approximately 30 nm from the film-substrate interface (See Figure 20 a for a representation of the scan position). The lattice parameter measurements of the algorithm in STO were used for calibration. Figure 41 a) and b) show the in-plane and out-of plane lattice parameter measurements, respectively, as calculated by the algorithm. Figure 41 c) and d) show the corresponding maps of the standard deviation associated with each measurement. From Figure 41 it can be seen that:

- From a) and b), the measured lattice parameters are placed between the nominal axes of tetragonal BTO (a = 3.992 Å , c = 4.036).
- From a) and b) the measured in-plane and out-of-plane lattice parameters vary in the scanned area.
- From c) and d), the standard deviation is observed to vary between 0-5 pm.

The algorithm measurements were compared to the manual lattice parameter measurements to see if the results were coherent. Figure 42 a) and b) again show the in-plane and out-of-plane lattice parameters as calculated by the algorithm. Areas where manual measurements were performed are indicated with numbered squares. Figure 42 c) and d) show the out-of-plane and in-plane lattice parameters in the indicated areas, as obtained from manual measurements and from the algorithm. The algorithm measurements presented in c) and d) are the mean measurements of the algorithm measurements in the marked areas. The standard deviations of the algorithm data presented are the mean standard deviations of the individual measurements, not the standard deviation of the mean. From Figure 42 c) and d) the manual measurements and algorithm measurements are not observed to correlate perfectly. Both measurements have considerable uncertainties, which may be the cause of the deviations.

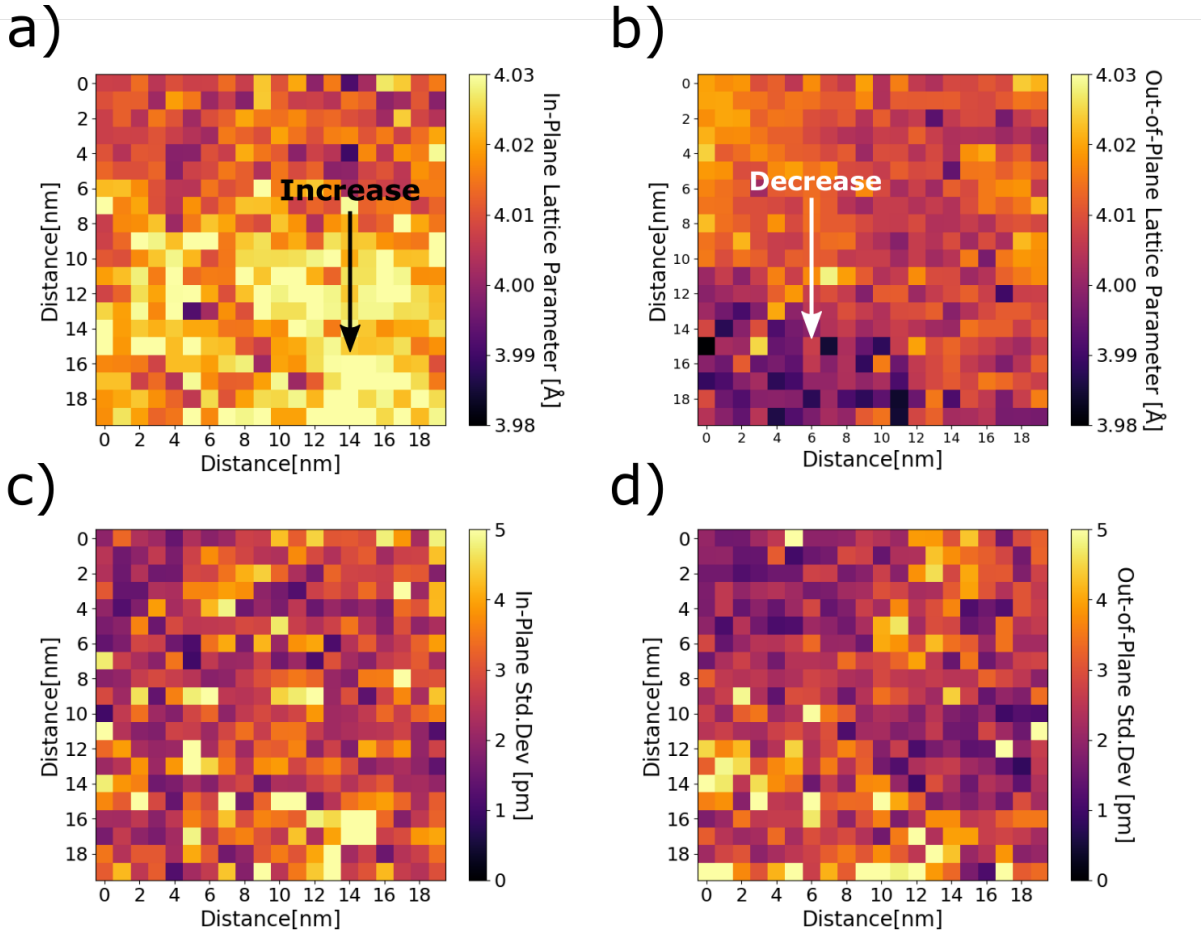

Figure 41: SCBED results from a 20 nm x 20 nm scan in BTO. a) and b) present the in-plane and out-of-plane lattice parameters as measured by the lattice parameter algorithm, respectively. In both maps the measured lattice parameter is observed to vary within the plot. c) and d) show the standard deviations associated with the in-plane and out-of-plane lattice parameters, respectively. The standard deviations also vary within the plot, indicating that the algorithm performs better in some regions than others.

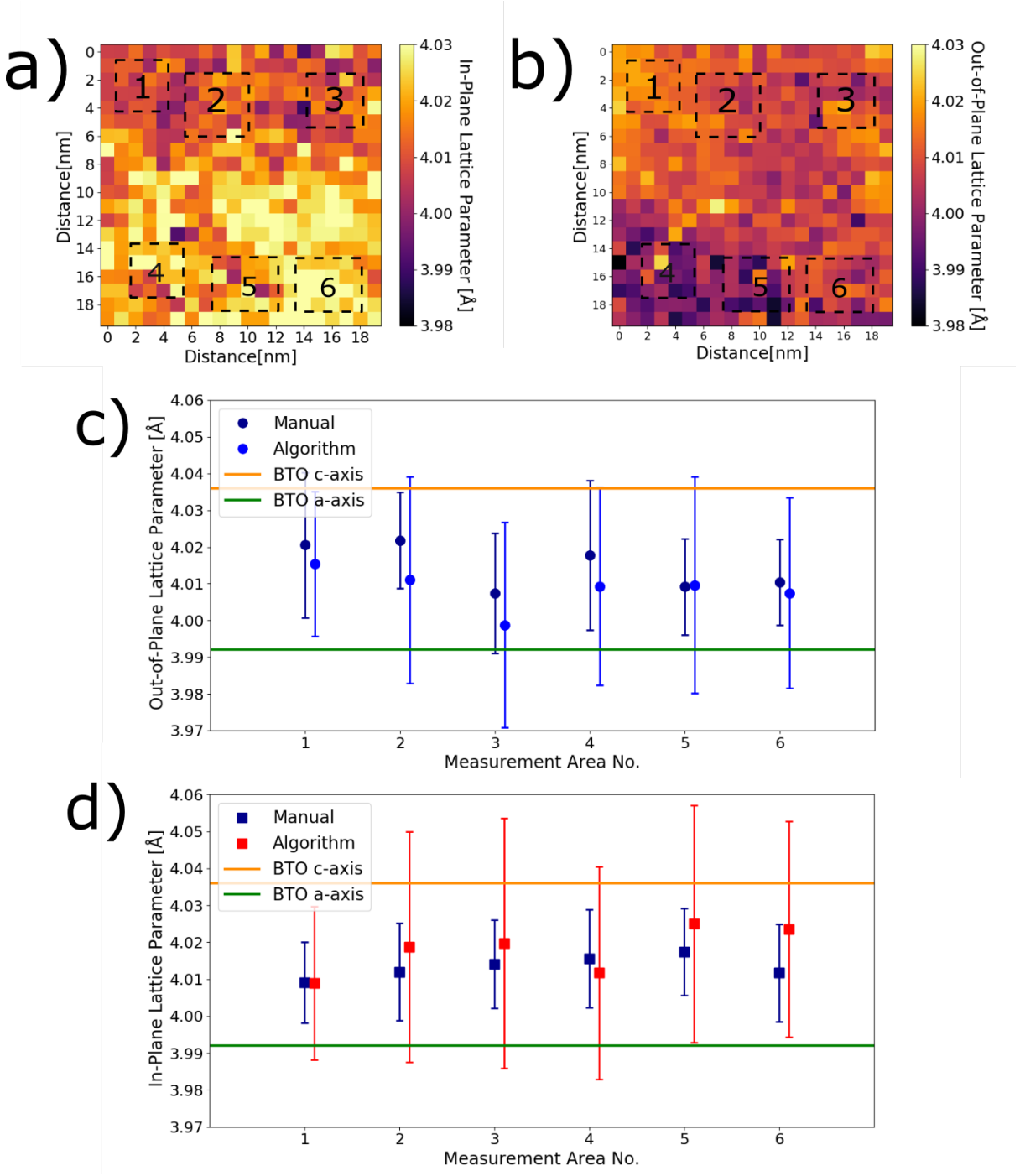

Figure 42: Lattice parameters measured in BTO manually and by algorithm. a) and b) present the in-plane and out-of-plane lattice parameters as measured by the lattice parameter algorithm, respectively. Areas where manual measurements were performed are indicated. c) and d) show the out-of-plane and in-plane lattice parameters in the indicated areas, as obtained from manual measurements and from the algorithm. The algorithm values presented are the mean values of the marked areas. The standard deviations of the algorithm data presented are the mean standard deviations of the individual measurements, not the standard deviation of the mean. The manual and algorithm measurements do not correlate perfectly, but their variations fall within the uncertainties.

Figure 43 shows a scatter plot of all lattice parameter measurements from the five 20 nm x 20 nm scans. Only datapoints with standard deviation lower than 3 pm are plotted. The expected positions corresponding to in-plane and out-of-plane polarization have been indicated in the plot. The average in-plane lattice parameter from these datasets is 4.011±0.021 Å and the average out-of-plane lattice parameter is 4.017±0.021 Å. The total sampling area was 2000 nm^2. From figure 43 it is visible that most measurements place the lattice parameters between the nominal c and a lattice parameters for tetragonal BTO.

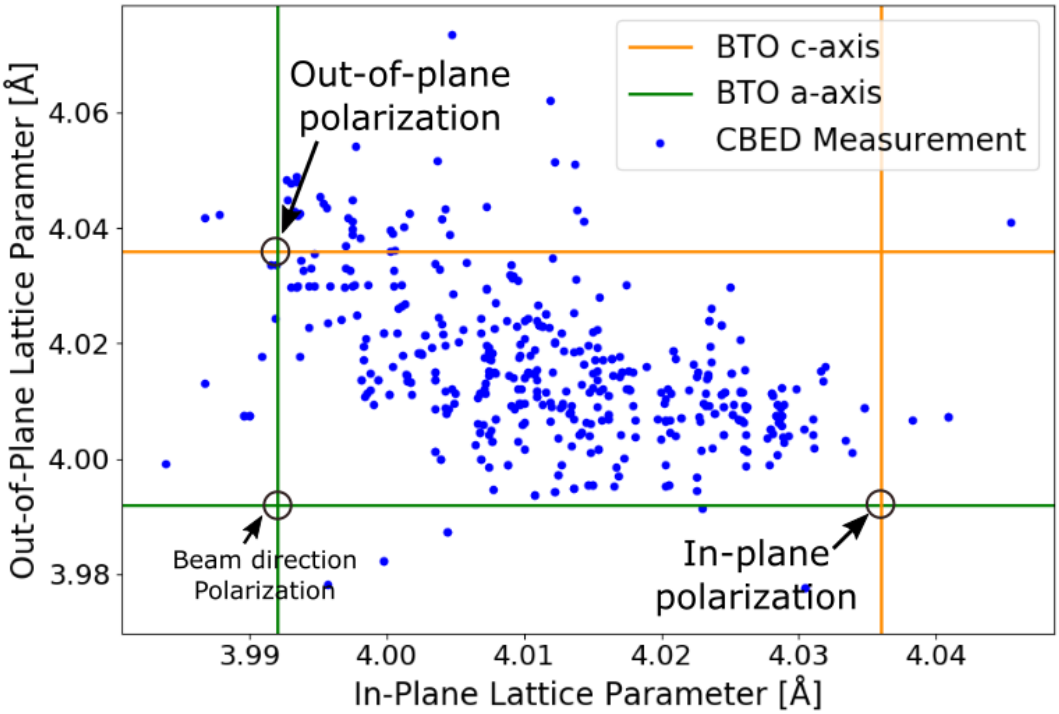

Figure 43: A scatter plot presenting all lattice parameter measurements by algorithm for the five 20 nm x 20 nm scans in the BTO films. The lattice parameters of tetragonal BTO are indicated. The measured lattice parameters are between the nominal values of tetragonal BTO. Only datapoints where the standard deviation of both lattice parameters is less than 3 pm are presented.

The rest of the section presents the data acquired from the 80 nm x 3 nm scans across the thickness of the film (see Figure 20 a for a representation of the scan position).

Figure 44 a) and b) show the measured lattice parameters by the algorithm and by the manual measurement for one of the scans, respectively. The lattice parameters are plotted against the length of the scan. The left side of the plot corresponds to the area close to the top of the film, and the right side corresponds to the area close to the substrate. For each unit of length of the scan, the median of the 3 measurements is presented. The standard deviation has not been included in the algorithm plot to avoid cluttering, however all measurements with standard deviations over 4 pm have been removed. Figure 44 b) shows manual measurements from the same scan. The measurements were made from areas of size 3 nm x 3 nm. From Figure 44 it can be seen that:

- The manual and algorithm measurements correspond well in the film.
- The measurements do not correspond in the substrate, with the manual measurements being several picometers higher than values found by the algorithm.
- Both a) and b) show slight variations in lattice parameter across the thickness of the film.
- The algorithm is not able to produce measurements with standard deviation less than 4 pm around the film-substrate interface.

Figure 44 is representative of the 5 interface measurements taken over the thickness of the film. All scans, with error bars included, are presented in appendix A.

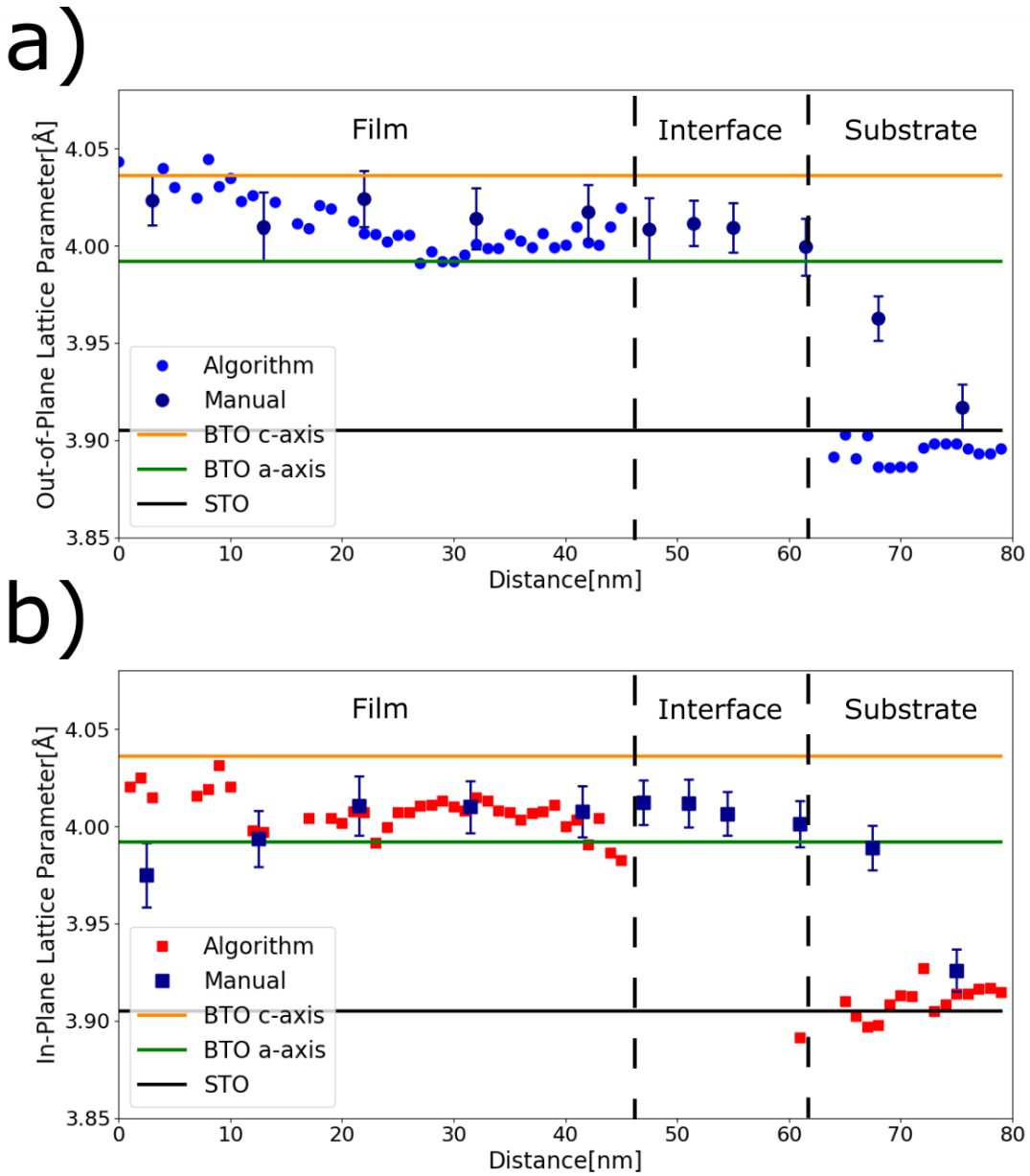

Figure 44: Lattice parameter measurements from a 80 nm x 3 nm SCBED scan across the BTO film. a) and b) present the out-of-plane and in-plane lattice parameter as measured manually and by the algorithm. The manual measurements were acquired from summed 3 nm x 3 nm areas. All algorithm measurements with standard deviation above 4 pm have been excluded, resulting in a gap in the measurements at the interface between the film and the substrate. This shows that the algorithm is not able to produce reliable measurements in an area close to the film-substrate interface, likely due to the strain and disorder present there. In the film the manual and algorithm measurements correspond well, whereas they differ in the substrate.

5 Discussion

The first aim of this thesis was to study the microstructure of chemical solution deposited BTO thin films by TEM in order to determine polarization direction and domain structure. The second aim of this thesis was to test the feasibility of the SCBED technique for determining domain structures. Section 5.1 discusses the acquired results and how they relate to the film microstructure of the film annealed at 1000°C. Section 5.2 discusses the data acquisition and processing.

5.1 Microstructure

First, section 5.1.1 discusses the BF images acquired from the specimens. Section 5.1.2 discusses the SADPs acquired from the film annealed at 1000°C. Section 5.1.3 discusses the symmetry of the simulated and experimental CBED patterns. Finally, section 5.1.4 discusses the lattice parameter measurements by algorithm and SADP, and how they relate to the domain structure of the film annealed at 1000°C.

5.1.1 Bright Field Images

From Figures 26 and 27 it is observed that the annealing temperature of 700° produced polycrystalline thin films, whereas the annealing temperature of 1000° produced epitaxial thin films. The average thickness of the epitaxial film was 60 ± 5 nm. At higher magnifications arrays of edge dislocations in the film-substrate interface of the epitaxial film are revealed, as can be seen in Figure 28. These coherency dislocations relax the strain fields caused by film-substrate lattice parameter mismatch [37]. The formation of the dislocations was expected, as the film thickness is an order of magnitude larger than the critical thickness for dislocation formation observed in comparable BTO thin films [42]. No domain structure was visible from BF images.

Dislocations lines inclined at angles ≈45° to the substrate are visible in Figures 27 a) and b). The lines of contrast likely indicate misfit dislocations along the $\{101\}\langle 10\bar{1}\rangle$ slip-system, which have been shown to be a preferential slip-system in perovskites by a limited number of TEM studies [67][68].

5.1.2 Selected Area Diffraction Patterns

The observation of multiple distinct BTO peaks in the SADPs, exemplified in Figure 30, show that the film consists of multiple distinct crystal domains. Each peak corresponds to a BTO domain, with different lattice parameter and orientation with respect to the substrate. Previous work on ferroelectric epitaxial films has shown that domain patterns with rotated domains can form in order to relieve stresses caused by the transformation from the paraelectric to the ferroelectric phase [69][37]. However, these studies show an ordered domain structure, which should cause the SADP peaks to split into two clearly distinct peaks, corresponding to two domain types [37]. In violation of expectations, the results from the present work show that there is almost a continuum of BTO peaks, which changes depending on where in the film the measurement is taken. This indicates a complex disordered structure with multiple domain orientations with respect to the substrate. Non-uniform strain and small crystal volumes are also possible factors contributing to diffraction peak broadening

[70].

Lattice parameter measurements from SADP presented in Figure 29 indicate that both the in-plane and out-of-plane lattice parameters vary between the nominal a and c lattice parameters for tetragonal BTO. On comparison with X-ray diffraction measurements by Raeder et al. [9] from similar films, it is observed that the range of the measured lattice parameters matches well. Raeder et al. measured that the in-plane lattice parameter was larger than the out-of-plane parameter [9]. The present work found that the average out-of-plane lattice parameter was larger than the in-plane lattice parameter, based on a limited number of SADP measurements.

The discrepancy between these two results may be attributed to the limited amount of data acquired in the present work, alteration of the specimen by FIB preparation [48][71] , exposure to the electron beam, or actual variation between the films investigated by Raeder [9] and the films investigated in the present work. The investigated film had 6 deposited layers and was heated from below during synthesis, whereas the films investigated by Raeder had 8 deposited layers and were heated from above. These variations are possible causes of the observed discrepancy.

5.1.3 Convergent Beam Electron Diffraction

Simulated CBED patterns in Figures 34 and 35 show that the asymmetry induced by misalignment is large compared to the asymmetry induced by polarization. However, it was found that the intensity distribution of the 000 disc is very sensitive to beam-specimen misalignment, making it a useful measure of whether the beam is aligned on the ZA. Misalignment also breaks the mirror symmetry planes in some CBED discs, which gives another measure of whether the beam is aligned on the ZA. From observing the simulated patterns it seems theoretically possible to distinguish asymmetry induced by misalignment from asymmetry induced by polarization.

Experimental CBED patterns acquired from the film are disordered and asymmetrical when compared to the simulated patterns of single crystal BTO. Patterns acquired near the interface and thicker film sections show the highest degree of disorder, as seen from Figure 36.

As polarization is expected to produce only little asymmetry (see Figure 32), the observed asymmetry likely has other sources than polarization. A possible source of asymmetry is that the beam traverses multiple domains with different orientations, such that it is impossible to align all the domains at once. From Figure 35 it was shown that even beam-specimen misalignment of 0.01° produces a relatively high degree of asymmetry. From SADP the maximum rotation between domains was observed to be 0.4°. Furthermore, a first estimate of the domain widths would be approximately 30 nm, based on the observed film thickness and the model of Luk'yanchuk et al. [48]. By this estimate the electron beam traversing the $\approx$ 75 nm specimen thickness would encounter multiple domains. An argument for using Luk'yanchuks model is that it conforms well with measurements by Raeder on similar BTO thin films [50]. An argument against using the domain width estimate is that Luk'yanchuks model was developed for ordered BTO domain patterns.

Domain walls are another sources of local asymmetry [45]. Other possible sources of the observed asymmetry are strain and dislocations, which were observed in the film in BF

images. From Figure 40 the processed SCBED data show no correlation between lattice parameters and symmetry metrics, and thereby no correlation with the polarization, which is expected as the asymmetry likely has other sources than the polarization.

5.1.4 Domain Structure

The lattice parameter measurements performed on the SCBED datasets place the lattice parameter between the tetragonal BTO a and c lattice parameters, in agreement with SADP measurements. From Figure 44 the SCBED scans from the top of the film to the substrate indicate variations in lattice parameter. This observation stands in contrast to the model proposed by Raeder et al. [9], where the domains extend from the substrate to the top of the film.

The acquired data from SADP and SCBED indicate a disordered domain structure, where domains can take on a whole range of lattice parameters and orientations. However, the uncertainty associated with the lattice parameter measurements, both manually and by the algorithm, are too large to make more conclusive statements about the domain structure.

5.2 Data Acquisition and Processing

First, section 5.2.1 discusses the symmetry quantification program. Section 5.2.2 discusses the quality of the SCBED acquisition routine. Section 5.2.3 discusses the validity of measuring distances in CBED patterns to obtain lattice parameters. Finally, section 5.2.4 discusses the precision of the algorithm for lattice parameter measurements.

5.2.1 Quality of Symmetry Quantification

Figure 31 a) shows that the program processes simulated patterns correctly. Figure 31 b) shows that the program also gives the expected results when evaluating the symmetry of experimental single crystal patterns, with a small deviation in the C-metric. The source of this deviation may come from the manual selection of the disc positions or the beam being slightly off ZA.

Repeated measurements of symmetry metrics from the same pattern give similar values, indicating that manual selection of discs can be used to determine symmetry. The quality of the symmetry quantification algorithm is therefore not considered a significant source of error in the measurements. However, to achieve an even better algorithm, disc positions could be determined semi-automatically using normalized cross-correlation [13].

5.2.2 Quality of SCBED Acquisition

The quality of the scanning procedure was evaluated by examining scanning sets from the STO substrate. From Figure 38 a) and b) it was observed that the beam-specimen misaligned was about 0.05° from the [001] ZA 60 nm from the scan start position, which caused significant asymmetry. It was found that areas of 20 nm x 20 nm around the scan start position had a sufficiently good beam-specimen alignment.

Previous work by Kim and Zuo [13] shows that good beam-specimen alignment is possible for scanning areas larger than 200 nm x 200 nm. The two main differences identified between the present work and the work by Kim and Zuo are the instrument alignment and the specimen studied. When aligning the instrument a procedure inspired by Hsiao [63] and Shao [64] was followed. However, due to instrument limitations the proposed alignment procedures were not followed completely. Specifically, not all TEM lenses were used in the instrument alignment. A more rigorous alignment procedure would be required if SCBED were to be used to determine the domain structure of a film using symmetry metrics.

When moving the converged beam across the specimen, slight specimen bending was observed. A possible source of this bending could be that the specimen was clamped in the FIB TEM grid. To minimize the bending, a specimen could instead be mounted on only one side of the TEM grid.

5.2.3 Quality of Manual Measurements

The asymmetry of the CBED patterns acquired from the film was partially attributed to the beam electrons traversing multiple domains when going through the specimen. From SADPs the domains are expected to vary in rotational orientation and in lattice parameter. Multiple overlaid domains may change CBED disc shape and position in non-trivial ways. As the centers of the observed CBED discs were used for lattice parameter measurements, it is of interest to see how the beam traversing multiple domains would affect the measurements.

A first approximation to a CBED pattern from multiple domains is produced by overlapping the CBED patterns of single domains with different lattice parameters and orientations. Figure 45 a) shows the pattern produced when superimposing two CBED patterns from domains with different lattice parameters. Figure 45 b) shows Figure 45 a) after application of the edge detection algorithm. In real CBED patterns the outermost edge is often the most prominent, and upon inspection of b) it is seen that this would cause the observed discs to take on a slightly elliptical form. The center of this ellipse would fall between the centers of the discs corresponding to the individual domains. As the edges of the ellipse are defined by the domains with the longest and the shortest lattice parameters, the measured lattice parameter would be the average of the largest and smallest lattice parameter.

Figure 45 c) shows the CBED patterns of two domains rotated with respect to each other, superimposed. This also causes the discs to take on an elliptical form. The center of the ellipses lie between the centers of the discs corresponding to domain A and B. From Figure 46 it is seen that the center of an ellipse is closer to the 000 disc by a factor of $\cos\theta/2$, resulting in an overestimation of the lattice parameter by a factor of $(\cos\theta/2)^{-1}$. From SADPs it was measured that the maximal rotation between two BTO domains was about 0.4°, which results in a correction of $\cos 0.2^\circ = 0.999994$, which has virtually no impact on the measured results. To summarize:

- When multiple domains of different lattice parameters are traversed, the measured lattice parameter is the average of the largest and smallest lattice parameter of the domains traversed, in the direction measured.
- Whereas small domain rotations have a large impact on the CBED patterns intensity distribution (see section 4.4.1), they have little impact on the distances between disc centers.

The above results indicate that measurements between disc centers may give an estimate of the lattice parameters even if multiple domains are traversed. For further validation of how the traversal of multiple domains affects the beam, simulations taking into account dynamical effects should be performed.

A differential between the lattice parameter measurements by the algorithm and by the manual method is observed in some scans, as in Figure 44. A possible cause for the observed deviations is that the manual measurements are taken from several CBED patterns summed together, whereas the algorithm measures from only one pattern at a time. Based on the algorithm performance in the STO substrate, it is likely that the error lies in the manual measurements.

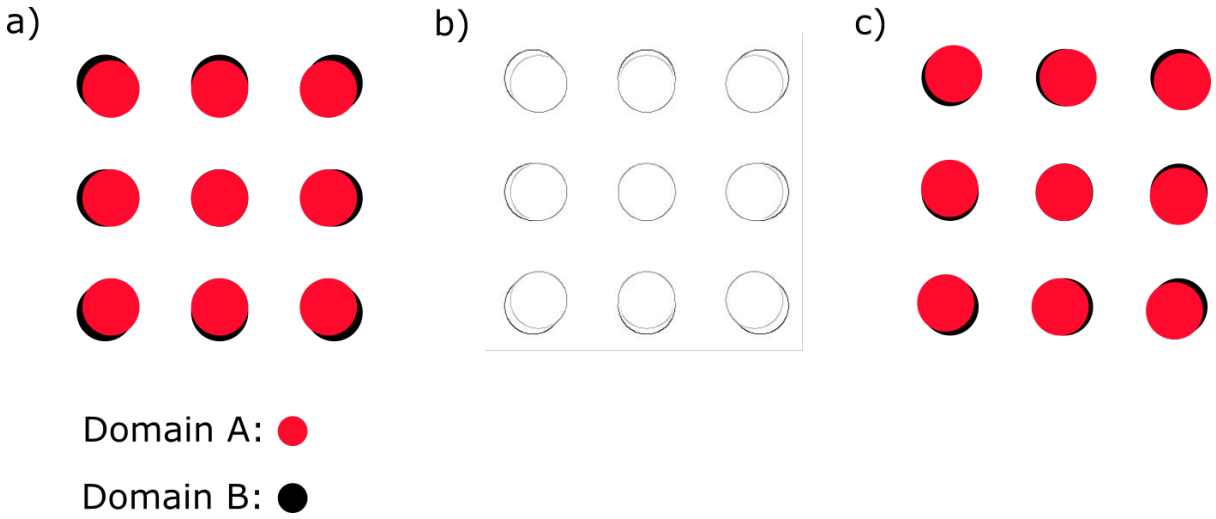

Figure 45: When a convergent electron beam traverses multiple domains, the resulting CBED patterns will to a first approximation consists of several individual CBED patterns superimposed. a) shows two CBED patterns of domains with different lattice parameters superimposed. Domain A has larger lattice parameter than domain B in both the horizontal and vertical direction. b) After applying edge detection to a), it is seen that the discs now resemble ellipses. c) Domain A is rotated with respect to domain B. Again the outline of the discs trace out ellipses.

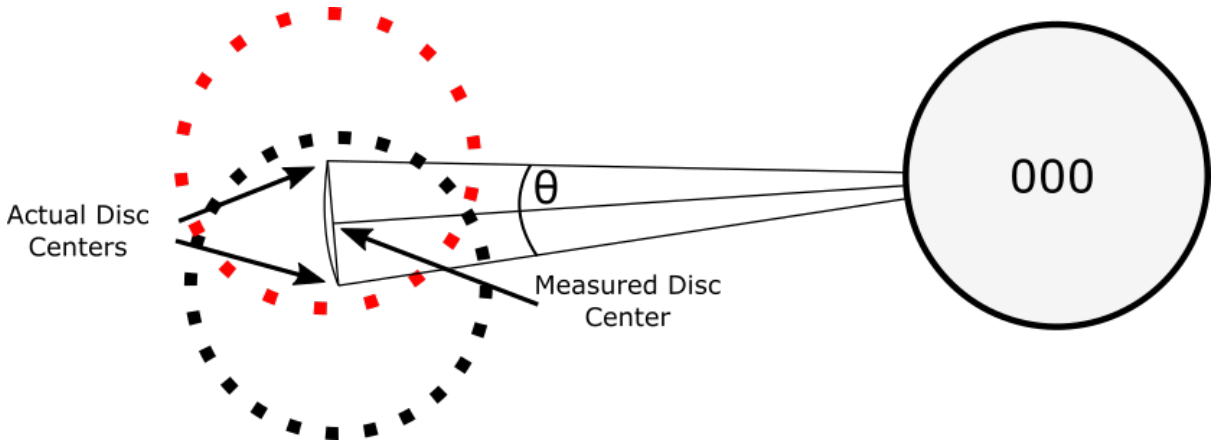

Figure 46: When two CBED patterns with a small relative rotation are superimposed, the resulting discs resemble ellipses. The center of the ellipse is closer to the 000 disc than the centers of the individual discs. This would cause an overestimation of the lattice parameter by a factor of $(\cos\theta/2)^{-1}$, which is insignificant considering that largest observed rotation between BTO crystal volumes in this work was 0.4°. The rotation between domains is exaggerated in this figure for clarity.

5.2.4 Quality of Measurements by Algorithm

The lattice parameter algorithm was tested on the STO single crystal substrate aligned on the [001] ZA. From the lattice parameter maps in Figure 39 the measured lattice parameter is observed to vary slightly with position, around ±1.5 pm. The cause of this variation may be associated with the algorithm or inhomogeneity in the substrate. It is observed that the out-of-plane lattice parameter has a larger standard deviation than the in-plane lattice parameter. As the algorithm is symmetric with respect to the in-plane and out-of-plane direction, this is likely due to asymmetry in the CBED patterns. A possible source of asymmetry that could influence these measurements is lens astigmatism.

The relative uncertainty of the measurements in the film was higher than in the substrates, as can be seen from Figure 41 c) and d). A reason for this increase in uncertainty may be that the algorithm detects discs from several different domains. Figure 47 a) shows a cross-correlation map produced from template matching an experimental BTO CBED pattern. The maxima correspond to positions where the template matched well. Figure 47 b) shows an excerpt of a). From b) two maxima are visible for one disc position. A regular CBED pattern would produce only one maxima per disc position. Figure 47 c) shows the cross-correlation map produced from a simulated CBED pattern with two domains overlapped (see Figure 45 c). Figure 47 d) shows an excerpt from one disc position. From d) it can be seen that the overlapping of two domains creates multiple maxima in the cross-correlation map. Comparing this to the experimental result in 47 b), the resemblance indicates that overlapping domains might be the cause of the observed multiple maxima. In the film sections where the algorithm has a large measurement uncertainty, the algorithm likely selects maxima corresponding to different domains. This leads to larger variations in lattice parameter measurements than expected. Lattice parameter measurements with large uncertainties have therefore been removed from the data presented in section 4, as they are a result of the algorithm not working as intended.

It was found that varying program parameters changed the uncertainty of the measurements in nontrivial ways. The program parameters influencing the uncertainty are:

- Size and position of template
- Parameters relating to edge detection
- Parameters relating to maxima-selection

Program parameters were varied by trial and error to identify which combinations gave rise to low measurement uncertainties.

Possible parameters relating to the experimental setup that influence the program output were identified as:

- Intensity distribution in the CBED pattern, as this influences edge detection
- Intensity distribution in the 000 disc, as this influences the template

To summarize, collected data indicate that the algorithm can produce lattice parameter measurements with picometer precision in single crystals.

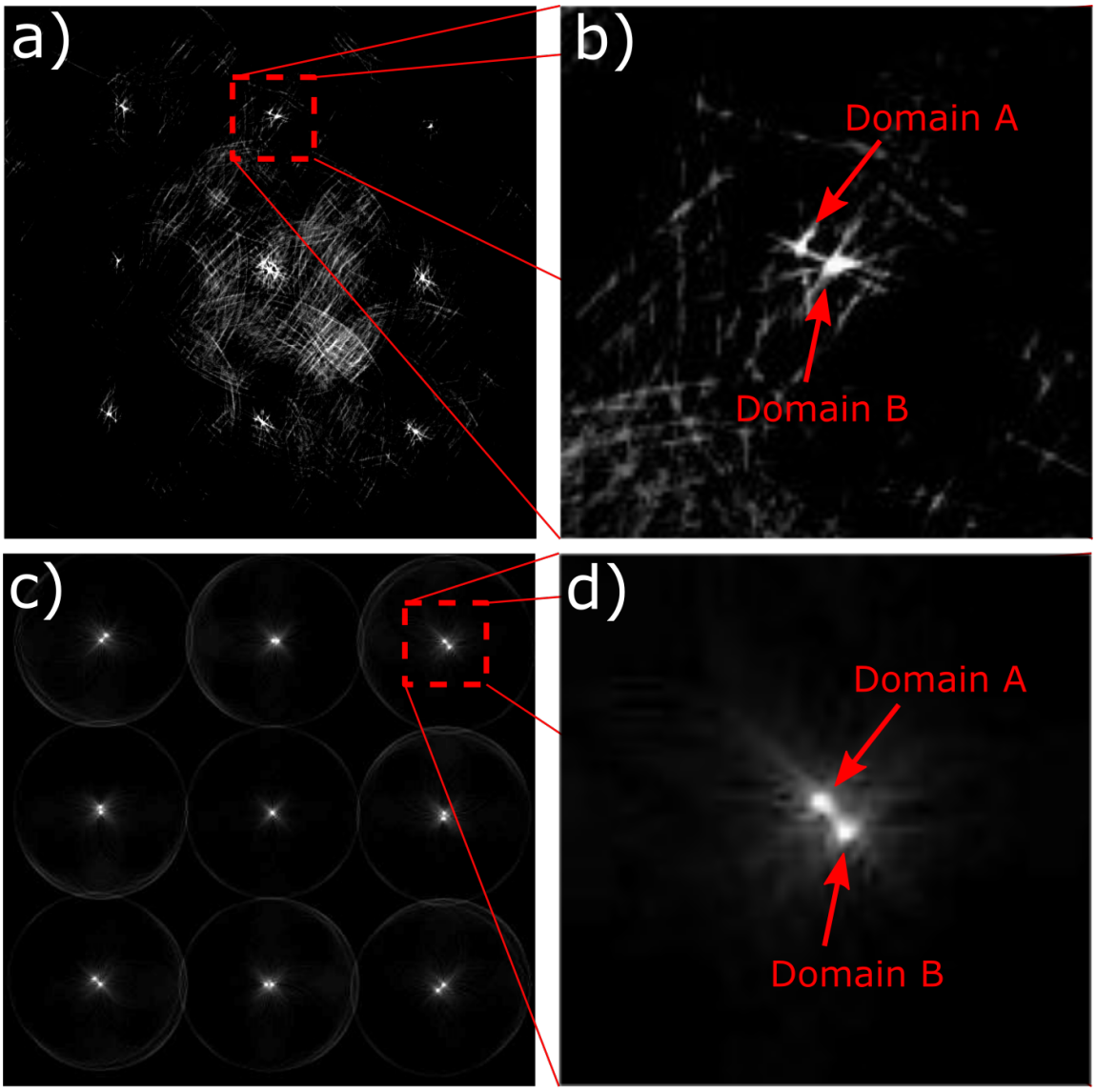

Figure 47: a) A cross-correlation map from an experimental BTO CBED pattern. The bright points signify where the template matched well with the pattern. b) Multiple maxima are visible at each disc position. c) A cross-correlation map of two simulated CBED patterns superimposed (see Figure 45 c)). d) Multiple maxima are visible at each disc position. The similarity of the experimental and simulated pattern suggests that electron beam traversed multiple domains with different orientations.

6 Conclusion

Two BTO thin films were studied by BF imaging, SAED and SCBED. The films were chemically solution deposited on a STO substrate, with annealing temperatures 700°C and 1000°C. Conclusions about the film annealed at 700°C were:

- The film thickness is 55 ± 3 nm.
- The film is polycrystalline.
- The film structure is dominated by columnar growth, where grains range from the substrate to the top of the film.

Conclusions about the film annealed at 1000°C were:

- The film thickness is 60 ± 5 nm.
- The film does not completely cover the substrate, leaving some areas exposed.
- Arrays of edge dislocations are formed at the film-substrate interface.
- Misfit dislocations are formed at angles approximately 45° to the interface.
- The film consists of multiple domains, with differing lattice parameters and orientations. The largest observed rotation between domains was 0.4°.
- The in-plane and out-of-plane lattice parameters of the BTO thin film are between the lengths of the nominal c and a lattice parameters of bulk tetragonal BTO.

Conclusions about the SCBED technique applied to the epitaxial film were:

- Asymmetry induced by polarization in CBED patterns is significantly less pronounced than asymmetry induced by small beam-specimen misalignment.
- It was not possible to produce highly symmetric CBED patterns in the film, likely due to overlapping domains, strain and dislocations.
- Symmetry metrics of the CBED patterns did not correlate with lattice parameter measurements for the film, which renders symmetry metrics not viable for measuring polarization in this specimen.
- The beam-specimen misalignment introduced by the scanning procedure limited the scan size to an area of 20 nm x 20 nm around the scan start position.

Conclusions about the automated lattice parameter algorithm were:

- Combining edge detection and template matching, lattice parameter measurements from SCBED datasets were automated with picometer precision.
- The precision of the algorithm is higher for single crystal substrate than for the film produced by CSD.
- The algorithm did not have good enough precision to decisively determine the domain structure in the epitaxial thin film.

7 Further Work

By SAED it was shown that there are multiple domains in the epitaxial film. However, by SAED it is not possible to achieve the spatial resolution required to determine the domain structure in these films. It is therefore of interest to investigate the film with a high-spatial-resolution low-uncertainty lattice parameter measurement technique.

Lattice parameter measurements by algorithm from SCBED datasets have the possibility to meet these requirements. Although the present work concluded that the measurements produced by the algorithm in the BTO film had too high uncertainty to resolve the domain structure, it was also shown that the desired measurement precision was achieved in single crystal STO. Thinner film specimens, energy filtering, modifications to the scanning acquisition technique, and more precise edge detection could make the automated measurements sufficiently precise to determine the domain structure. If a specimen is found in which symmetry metrics are correlated with polarization, a single SCBED dataset could yield both lattice parameters and polarization directions.

Further work on the experimental acquisition procedure and the CBED pattern processing is required to determine the full potential of the SCBED technique.

Other more established TEM techniques, such as quantitative HAADF-STEM [72][73] and scanning precession electron diffraction [74][75] could also meet the requirements to characterize the domain structure of the BTO thin films.

References

[1] W. P. Mason. Piezoelectricity, its history and applications. *The Journal of the Acoustical Society of America*, 70(6):1561–1566, 1981.

[2] L.E. Cross and R.E. Newnham. History of ferroelectrics. *Ceramics and Civilization*, 3:289–305, 1987.

[3] C.A. Randall, R.E. Newnham, and L.E. Cross. History of the first ferroelectric oxide, BaTiO3. *Materials Research Institute, The Pennsylvania State University, University Park, Pa, USA*, 2004.

[4] N. Setter et al. Ferroelectric thin films: Review of materials, properties, and applications. *Journal of Applied Physics*, 100(5):051606, 2006.

[5] P. Tang, D. J. Towner, T. Hamano, A. L. Meier, and B. W. Wessels. Electrooptic modulation up to 40 GHz in a barium titanate thin film waveguide modulator. *Optics Express*, 12(24):5962, 2004.

[6] J. F. Scott and C. A. Paz de Araujo. Ferroelectric memories. *Science*, 246(4936):1400–1405, 1989.

[7] R. W. Schwartz, T. Schneller, and R. Waser. Chemical solution deposition of electronic oxide films. *Comptes Rendus Chimie*, 7(5):433–461, 2004.

[8] N. Bassiri-Gharb, Y. Bastani, and A. Bernal. Chemical solution growth of ferroelectric oxide thin films and nanostructures. *Chem. Soc. Rev.*, 43(7):2125–2140, 2014.

[9] T. M. Raeder, K. Bakken, J. Glaum, M. A. Einarsrud, and T. Grande. Enhanced in-plane ferroelectricity in BaTiO3 thin films fabricated by aqueous chemical solution deposition. *AIP Advances*, 8(10):105228, 2018.

[10] Z. H. Zhang, X. Y. Qi, and X. F. Duan. Direct determination of the polarization direction of domains in BaTiO3 single crystal. *Applied Physics Letters*, 89(24):242905, 2006.

[11] K. Tsuda, A. Yasuhara, and M. Tanaka. Two-dimensional mapping of polarizations of rhombohedral nanostructures in the tetragonal phase of BaTiO3 by the combined use of the scanning transmission electron microscopy and convergent-beam electron diffraction methods. *Applied Physics Letters*, 103(8):082908, 2013.

[12] Y. Shao and J. Zuo. Nanoscale symmetry fluctuations in ferroelectric barium titanate, BaTiO3. *Acta Crystallographica Section B Structural Science, Crystal Engineering and Materials*, 73(4):708–714, 2017.

[13] K. Kim and J. Zuo. Symmetry quantification and mapping using convergent beam electron diffraction. *Ultramicroscopy*, 124:71–76, 2013.

[14] D. Schwarzenbach. *Crystallography*. John Wiley & Sons, 1996.

[15] K. J. Choi. Enhancement of ferroelectricity in strained BaTiO3 thin films. *Science*, 306(5698):1005–1009, 2004.

[16] W. D. Callister, D. G. Rethwisch, et al. *Materials science and engineering: an introduction*. John Wiley & Sons New York, 2007.

[17] D. B. Williams and C. B. Carter. *Transmission Electron Microscopy: Spectrometry. IV*. Plenum Press New York, 1996.

[18] J. M. Zuo and J. C. H. Spence. *Kinematical Theory of Electron Diffraction*. Springer New York, 2017.

[19] G. Friedel. Sur les symétries cristallines que peut révéler la diffraction des rayons röntgen. *CR Acad. Sci. Paris*, 157:1533–1536, 1913.

[20] C. J. Humphreys. The scattering of fast electrons by crystals. *Reports on Progress in Physics*, 42(11):1825, 1979.

[21] J. M. Cowley and A. F. Moodie. The scattering of electrons by atoms and crystals. i. a new theoretical approach. *Acta Crystallographica*, 10(10):609–619, 1957.

[22] H. Bethe. Theorie der beugung von elektronen an kristallen. *Annalen der Physik*, 392(17):55–129, 1928.

[23] User: Gringr. Scheme tem wikimedia commons. URL:*https* : *//commons.wikimedia.org/wiki/File* : *Scheme_TEM_en.svg*, Accessed: 16.12.2018.

[24] J. M. Zuo and J. C. H. Spence. *Electron microdiffraction*. Springer Science & Business Media, 2013.

[25] P. Goodman and G. Lehmpfuhl. Observation of the breakdown of friedel's law in electron diffraction and symmetry determination from zero-layer interactions. *Acta Crystallographica Section A*, 24(3):339–347, 1968.

[26] A. Eades. Educational article: when to use selected-area diffraction and when to use convergent-beam diffraction. *Acta Microscopica*, 17(1):101–105, 2008.

[27] K. Tsuda, R. Sano, and M. Tanaka. Nanoscale local structures of rhombohedral symmetry in the orthorhombic and tetragonal phases of BaTiO3 studied by convergent-beam electron diffraction. *Physical Review B*, 86(21), 2012.

[28] SrTiO3 crystal structure - springer database. https://materials.springer.com/isp/crystallographic/doc 2012. Accessed: 2019-06-23.

[29] BaTiO3 tetragonal crystal structure - springer database. https://materials.springer.com/isp/crystallographic/docs/sd_1626717, 2012. Accessed: 2019-06-23.

[30] X. Deng, X. Wang, H. Wen, A. Kang, Z. Gui, and L. Li. Phase transitions in nanocrystalline barium titanate ceramics prepared by spark plasma sintering. *Journal of the American Ceramic Society*, 89(3):1059–1064, 2006.

[31] K. Sakayori, Y. Matsui, H. Abe, E. Nakamura, M. Kenmoku, T. Hara, D. Ishikawa, A. Kokubu, K. Hirota, and T. Ikeda. Curie temperature of BaTiO3. *Japanese Journal of Applied Physics*, 34(Part 1, No. 9B):5443–5445, 1995.

[32] J. F. Scott. Applications of modern ferroelectrics. *Science*, 315(5814):954–959, 2007.

[33] K. Chen, Y. Chen, Z. Chen, C. Yang, and T. Chang. Temperature and frequency dependence of the ferroelectric characteristics of BaTiO3 thin films for nonvolatile memory applications. *Applied Physics A*, 89(2):533–536, 2007.

[34] G. A. Samara. Pressure and temperature dependences of the dielectric properties of the perovskites BaTiO3 and SrTiO3. *Physical Review*, 151(2):378–386, 1966.

[35] T. Ishidate, S. Abe, H. Takahashi, and N. Môri. Phase diagram of BaTiO3. *Physical Review Letters*, 78(12):2397–2400, 1997.

[36] W. D. Nix. Mechanical properties of thin films. *Metallurgical Transactions A*, 20(11):2217–2245, 1989.

[37] J. S. Speck, A. C. Daykin, A. Seifert, A. E. Romanov, and W. Pompe. Domain configurations due to multiple misfit relaxation mechanisms in epitaxial ferroelectric thin films. III. interfacial defects and domain misorientations. *Journal of Applied Physics*, 78(3):1696–1706, 1995.

[38] J. S. Speck and W. Pompe. Domain configurations due to multiple misfit relaxation mechanisms in epitaxial ferroelectric thin films. i. theory. *Journal of Applied Physics*, 76(1):466–476, 1994.

[39] V. Mehrotra, S. Kaplan, A. J. Sievers, and E. P. Giannelis. Ferroelectric behavior of pulsed laser deposited BaxSr1-xTiO3 thin films. *Journal of Materials Research*, 8(6):1209–1212, 1993.

[40] S. Kobayashi, K. Inoue, T. Kato, Y. Ikuhara, and T. Yamamoto. Multiphase nanodomains in a strained BaTiO3 film on a GdScO3 substrate. *Journal of Applied Physics*, 123(6):064102, 2018.

[41] J. S. Speck, A. Seifert, W. Pompe, and R. Ramesh. Domain configurations due to multiple misfit relaxation mechanisms in epitaxial ferroelectric thin films. II. experimental verification and implications. *Journal of Applied Physics*, 76(1):477–483, 1994.

[42] T. Suzuki, Y. Nishi, and M. Fujimoto. Analysis of misfit relaxation in heteroepitaxial BaTiO3 thin films. *Philosophical Magazine A*, 79(10):2461–2483, 1999.

[43] J. W. Matthews. Defects associated with the accommodation of misfit between crystals. *Journal of Vacuum Science and Technology*, 12(1):126–133, 1975.

[44] R. E. Smallman. *Modern physical metallurgy*. Elsevier, 2016.

[45] J. Guyonnet. *Ferroelectric Domain Walls: Statics, Dynamics, and Functionalities Revealed by Atomic Force Microscopy*. PhD thesis, 2014.

[46] D. Lee et al. Mixed bloch-néel-ising character of180°ferroelectric domain walls. *Physical Review B*, 80(6), 2009.

[47] W. Pompe, X. Gong, Z. Suo, and J. S. Speck. Elastic energy release due to domain formation in the strained epitaxy of ferroelectric and ferroelastic films. *Journal of Applied Physics*, 74(10):6012–6019, 1993.

[48] I.A. Luk'yanchuk, A. Schilling, J.M. Gregg, G. Catalan, and J.F. Scott. Origin of ferroelastic domains in free-standing single-crystal ferroelectric films. *Physical Review B*, 79(14), 2009.

[49] A. L. Roitburd. Equilibrium structure of epitaxial layers. *Physica Status Solidi (a)*, 37(1):329–339, 1976.

[50] T. M. Raeder. Private communication, 2019.

[51] J. Canny. A computational approach to edge detection. In *Readings in Computer Vision*, pages 184–203. Elsevier, 1987.

[52] W. Gao et al. An improved sobel edge detection. In *2010 3rd International Conference on Computer Science and Information Technology*. IEEE, 2010.

[53] C. Deng et al. Image edge detection algorithm based on improved canny operator. In *2013 International Conference on Wavelet Analysis and Pattern Recognition*. IEEE, 2013.

[54] W. Rong et al. An improved canny edge detection algorithm. In *2014 IEEE International Conference on Mechatronics and Automation*. IEEE, 2014.

[55] M. Parris. How a grumpy llama became the third person in our relationship. Web 2019 https://www.spectator.co.uk/2016/05/how-a-grumpy-llama-became-the-third-person-in-our-relationship/. Accessed: 15.6.2019.

[56] E. Jansen, W. Schäfer, and G. Will. R values in analysis of powder diffraction data using rietveld refinement. *Journal of Applied Crystallography*, 27(4):492–496, 1994.

[57] J. P. Lewis. Fast template matching. 95(120123):15–19, 1995.

[58] K. Briechle and U. D. Hanebeck. Template matching using fast normalized cross correlation. In David P. Casasent and Tien-Hsin Chao, editors, *Optical Pattern Recognition XII*. SPIE, 2001.

[59] K. Bakken. Private Communication, 2019.

[60] A. Toresen. Transmission electron microscopy characterisation of lead-free knn thin films. Master's thesis, Norwegian University of Science and Technology, 2018.

[61] P. A. Doyle and P. S. Turner. Relativistic hartree–fock x-ray and electron scattering factors. *Acta Crystallographica Section A*, 24(3):390–397, 1968.

[62] Pierre Stadelmann. Electron microscopy software-java version (jems). *CIME—EPFL: Lausanne, Switzerland*, 2011, 1999.

[63] H.W. Hsiao. Nbd and send operation manual on jeol. Private Communcation, 2019.

[64] Y. Shao. Scanning electron nanodiffraction(send). Private Communication, 2019.

[65] D. Johnstone. Scanning electron diffraction (sed) (program). Electron Microscopy Group Cambridge.

[66] Inkscape Team. Inkscape: A vector drawing tool. *URL http://www. inkscape. org*, 2004.

[67] Y. Wang, J. Poirier, and R. C. Liebermann. Dislocation dissociation in CaGeO3 perovskite. *Physics and Chemistry of Minerals*, 16(7), 1989.

[68] N. Doukhan and J. C. Doukhan. Dislocations in perovskites BaTiO3 and CaTiO3. *Physics and chemistry of minerals*, 13(6):403–410, 1986.

[69] R. C. Pond. Crystallographic analysis of domain formation in epitaxial films. *Journal of Crystal Growth*, 79(1-3):946–950, 1986.

[70] T. C. Lubensky et al. Distortion and peak broadening in quasicrystal diffraction patterns. *Physical Review Letters*, 57(12):1440–1443, 1986.

[71] W. Siemons, C. Beekman, J. D. Fowlkes, N. Balke, J. Z. Tischler, R. Xu, W. Liu, C. M. Gonzales, J. D. Budai, and H. M. Christen. Focused-ion-beam induced damage in thin films of complex oxide BiFeO3. *APL Materials*, 2(2), 2014.

[72] D. Park et al. Study of the ultrathin ferroelectric BaTiO3 film using scanning transmission electron microscopy. *Microscopy and Microanalysis*, 20(S3):138–139, 2014.

[73] A. B. Yankovich et al. Picometre-precision analysis of scanning transmission electron microscopy images of platinum nanocatalysts. *Nature Communications*, 5(1), 2014.

[74] P. A. Midgley and A. S. Eggeman. Precession electron diffraction – a topical review. *IUCrJ*, 2(1):126–136, 2015.

[75] J. Rouviere et al. Improved strain precision with high spatial resolution using nanobeam precession electron diffraction. *Applied Physics Letters*, 103(24):241913, 2013.

A Additional SCBED Data

The symmetry maps and lattice parameter maps generated from the five 20 nm x 20 nm SCBED datasets from the BTO thin film are presented in Figure A.1. The symmetry maps show that the symmetry of the CBED patterns is not as high as expected from simulations. Thus, the asymmetry is likely caused by other factors than polarization, and the symmetry maps can therefore not be used to determine polarization. The lattice parameter maps show that that there are local variations in measured lattice parameters. The measurement uncertainty varies for different areas of the scan.

The lattice parameter maps from the five 80 nm x 3 nm SCBED scans across the length of the BTO film are shown in Figure A.2. The lattice parameters are plotted against the length of the scan. The left side of the plot corresponds to the area close to the top of the film, and the right side corresponds to the side close to the substrate. For each unit of length of the scan, the median of the 3 measurements is presented. All measurements with standard deviations over 4 pm have been removed. The trends observed from the figures is that the measurement uncertainty in the film is larger than the measurement uncertainty in the substrate. The algorithm is not able to produce precise measurements in an area of length 10-20 nm between the film and the substrate. This is likely due to disorder introduced by the film-substrate interface. The lattice parameters vary slightly across the film. This could be an indication of the domain-structure. However, the associated uncertainties prohibit conclusive statements.

Figure A.3 shows lattice parameter maps generated from 8 nm x 8 nm SCBED datasets from the single crystal STO substrate. The measurement uncertainty is observed to be significantly less than in the film. As the algorithms STO measurements were deemed more precise than the manual measurements, they were used for calibration.

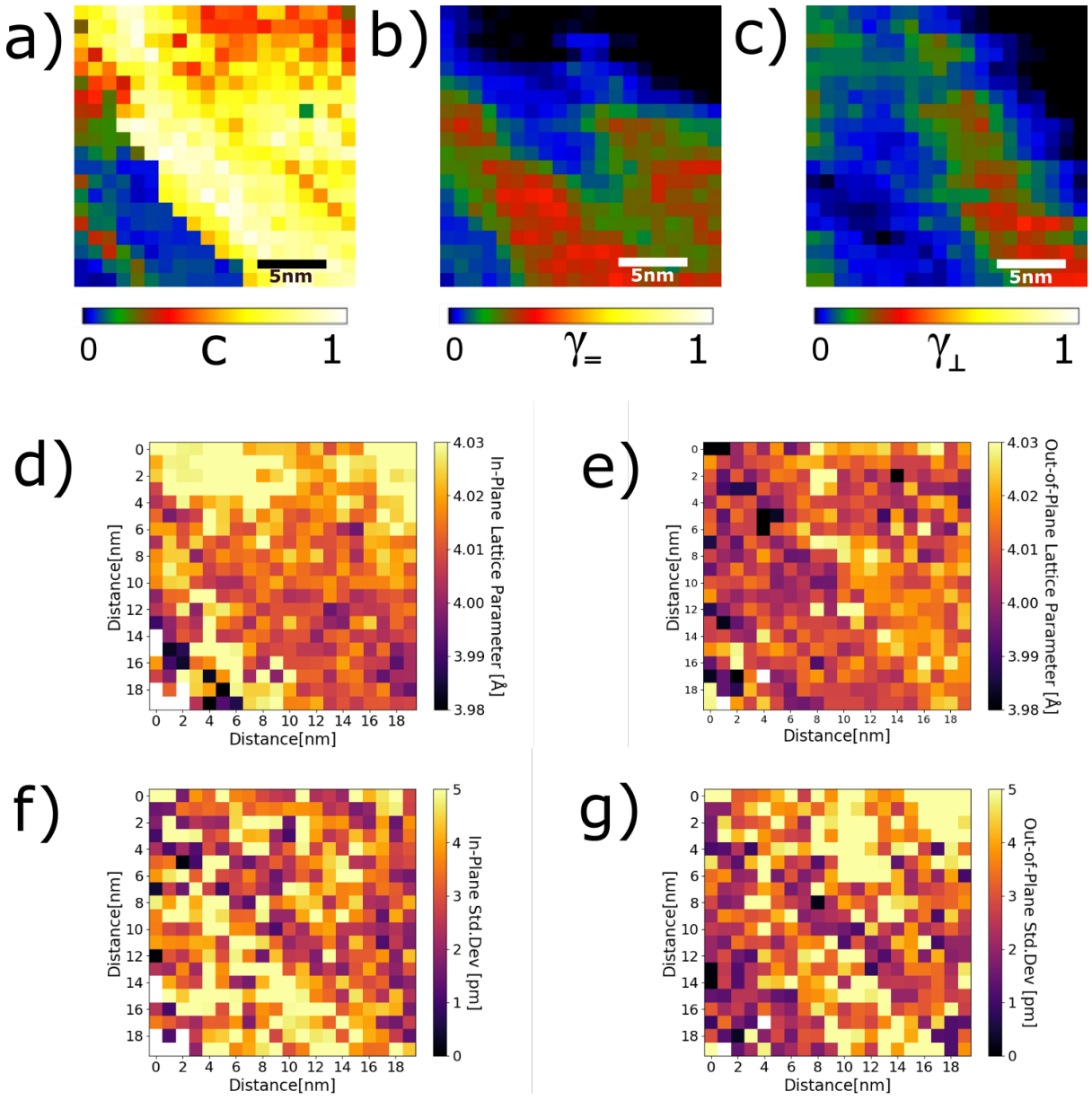

(a)

Figure A.1: The data generated from a 20 nm x 20 nm SCBED scan in the BTO thin film is shown in each subfigure. a), b) and c) show the symmetry maps of C, $\gamma_=$ and $\gamma_\perp$, respectively. From the low values of the γ metrics in b) and c) it is seen that the CBED pattern is asymmetrical. The asymmetry is therefore not an expression of polarization, but of other sources of asymmetry in the film. d) and e) show maps of the in-plane and out-of-plane lattice parameters as measured by the algorithm, respectively. f) and g) show maps of the standard deviation associated with each lattice parameter measurement.

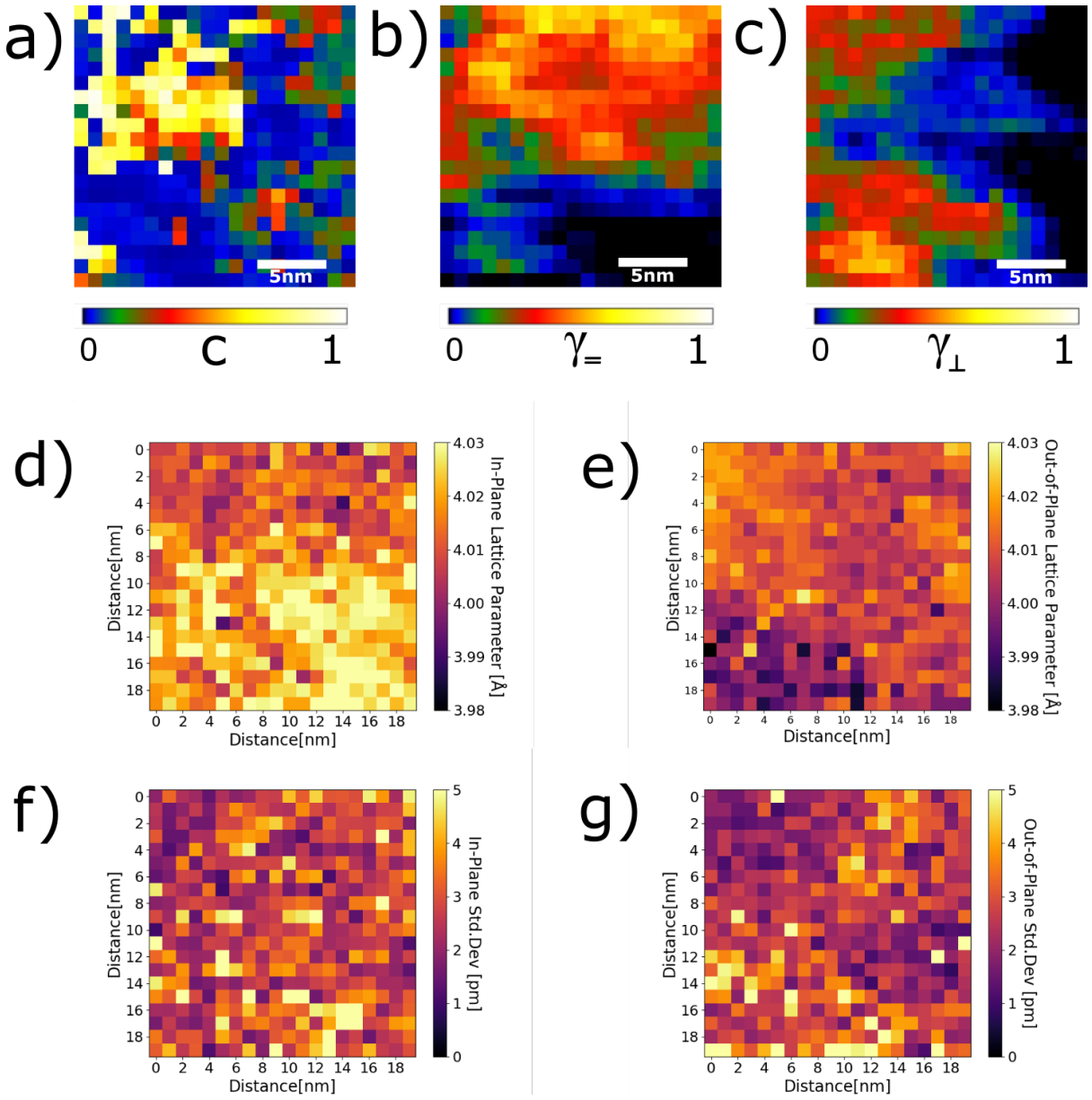
a)
b)
c)
5nm
5nm
5nm
0
c
1
0
γ=
1
0
γ⊥
1
d)
e)
f)
g)
Distance[nm]
Distance[nm]
In-Plane Lattice Parameter [Å]
Out-of-Plane Lattice Parameter [Å]
In-Plane Std.Dev [pm]
Out-of-Plane Std.Dev [pm]

(b)

Figure A.1

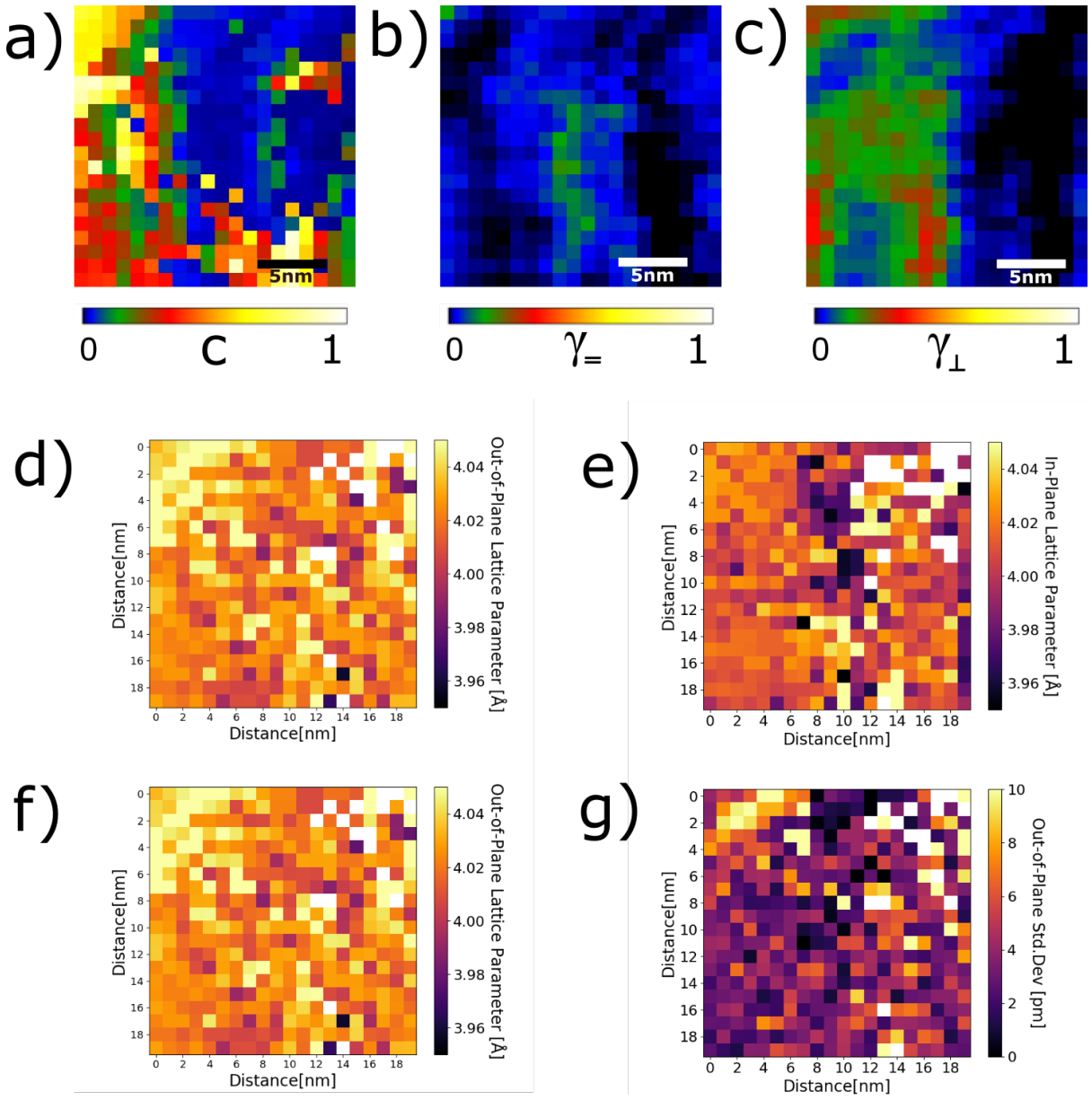
a)
b)
c)
5nm
5nm
5nm
0
c
1
0
γ=
1
0
γ⊥
1
d)
e)
f)
g)
Distance[nm]
Distance[nm]
Out-of-Plane Lattice Parameter [Å]
In-Plane Lattice Parameter [Å]
Out-of-Plane Std.Dev [pm]

(c)

Figure A.1

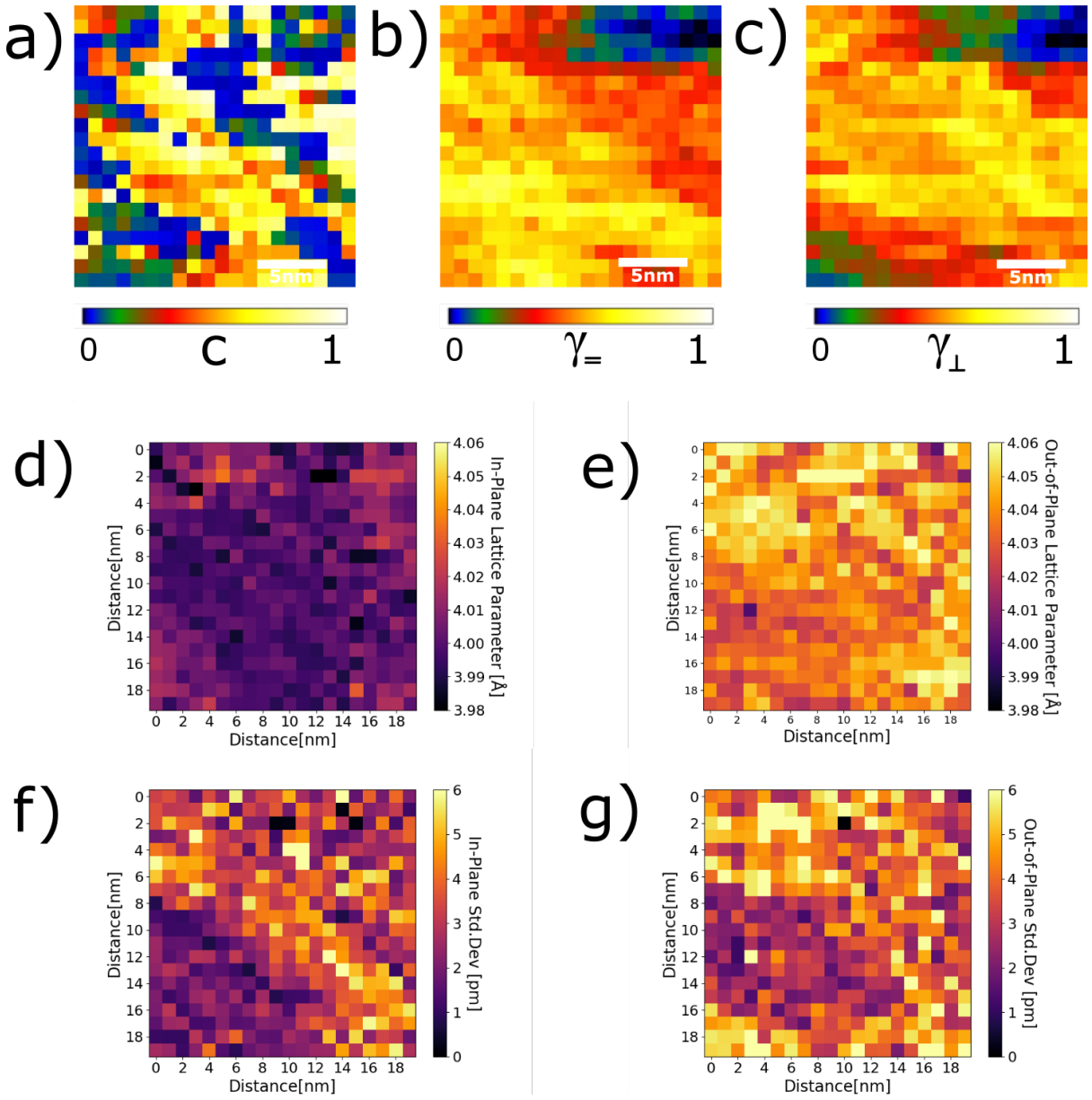
a)
b)
c)
5nm
5nm
5nm
0
c
1
0
γ=
1
0
γ⊥
1
d)
e)
f)
g)
Distance[nm]
Distance[nm]
In-Plane Lattice Parameter [Å]
Out-of-Plane Lattice Parameter [Å]
In-Plane Std.Dev [pm]
Out-of-Plane Std.Dev [pm]

(d)

Figure A.1

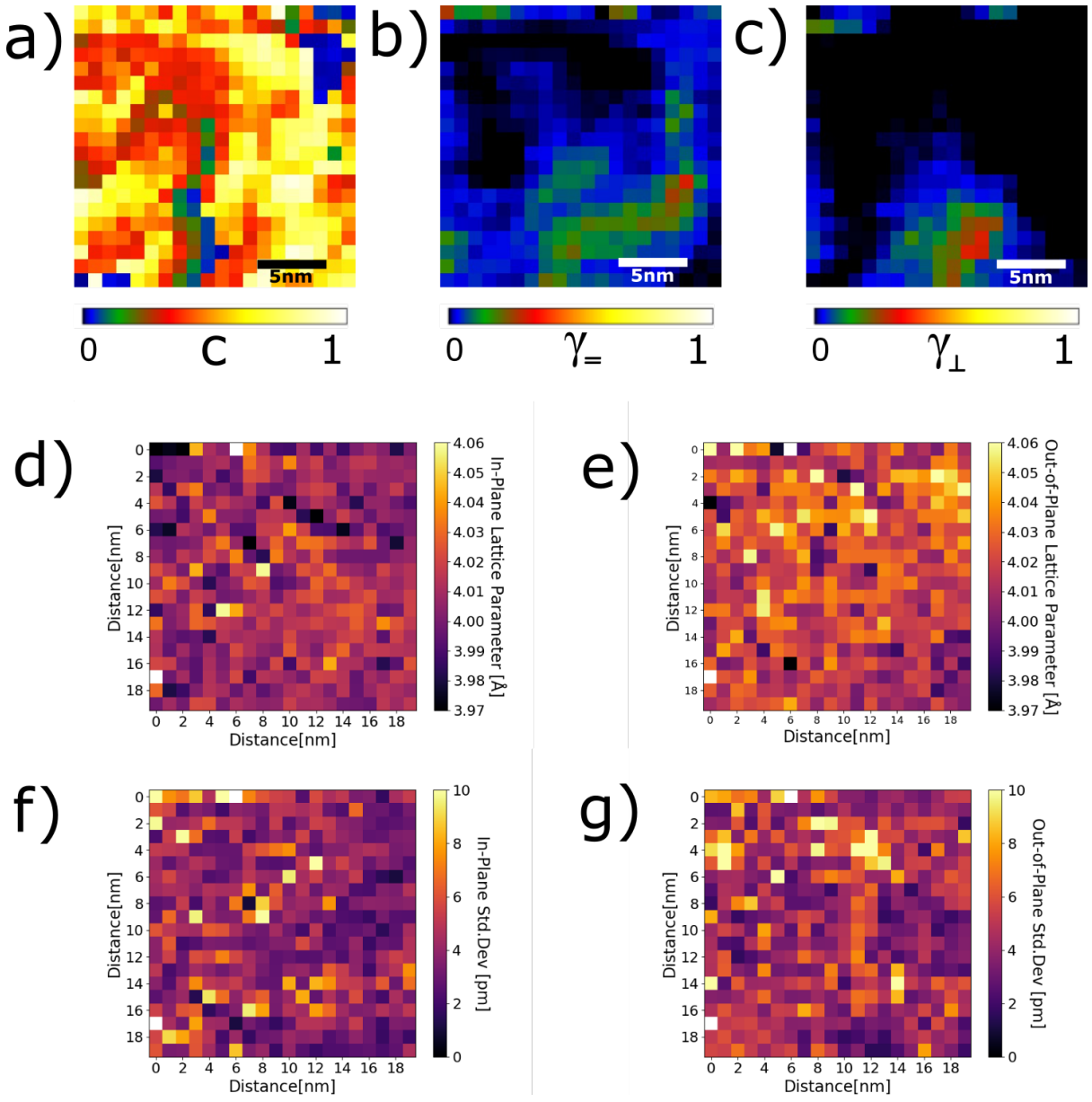
a)
b)
c)
5nm
5nm
5nm
0
c
1
0
γ=
1
0
γ⊥
1
d)
e)
f)
g)
Distance[nm]
Distance[nm]
In-Plane Lattice Parameter [Å]
Out-of-Plane Lattice Parameter [Å]
In-Plane Std.Dev [pm]
Out-of-Plane Std.Dev [pm]

(e)

Figure A.1

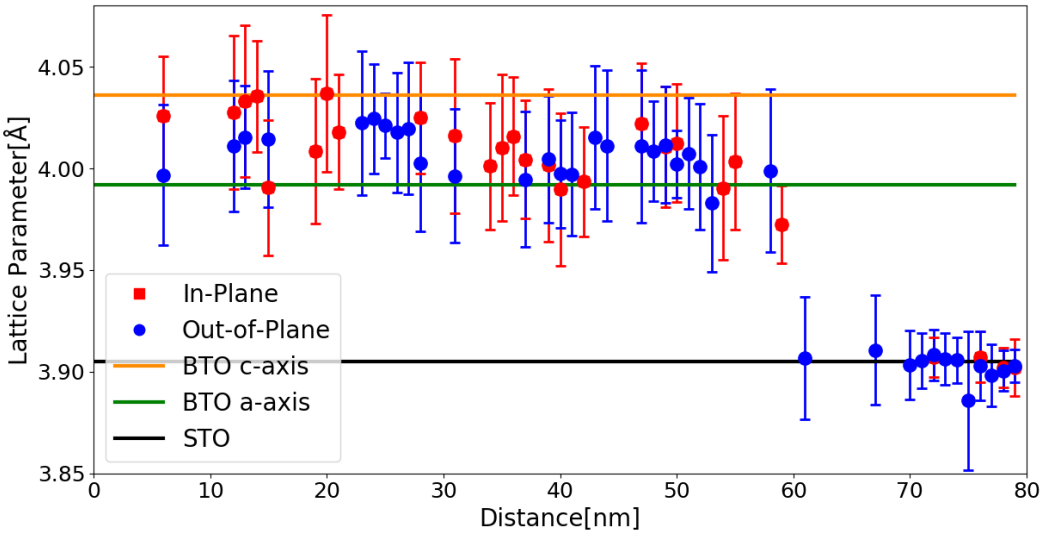

(a)

Figure A.2: The lattice parameter measurements from a 80 nm x 3 nm SCBED scan across the BTO film is shown in each subfigure. All measurements with standard deviation over 4 pm have been removed. The multiple gaps in the graph show that the algorithm struggles to produce accurate measurements in the BTO film. The measurements from the STO substrate, seen on the right, have better precision.

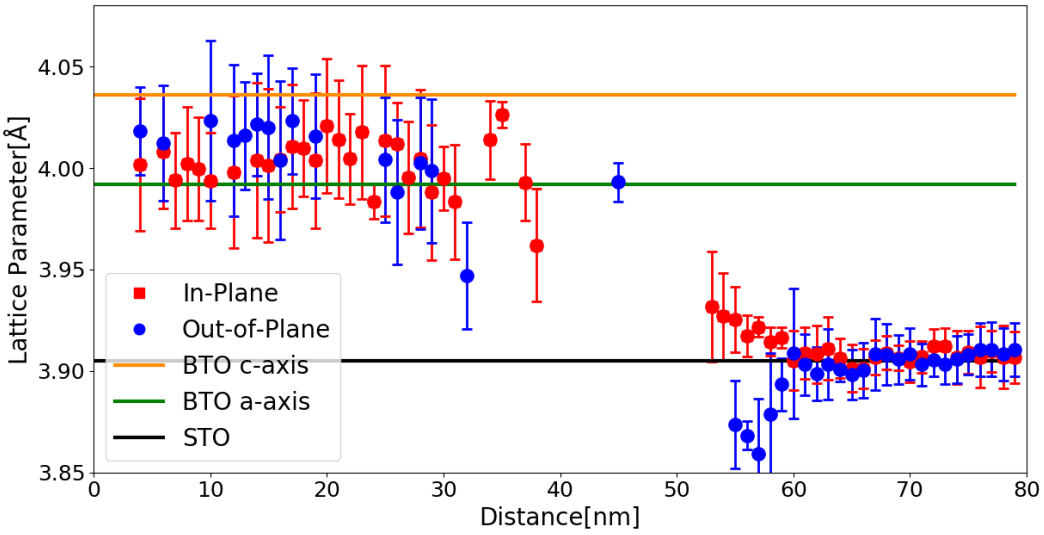

(b)

Figure A.2

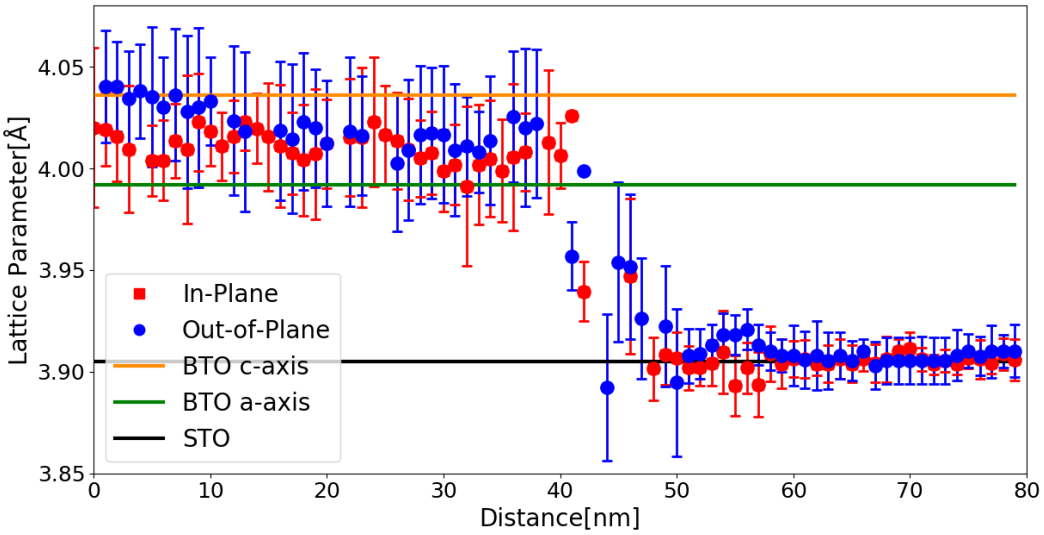

(c)

Figure A.2

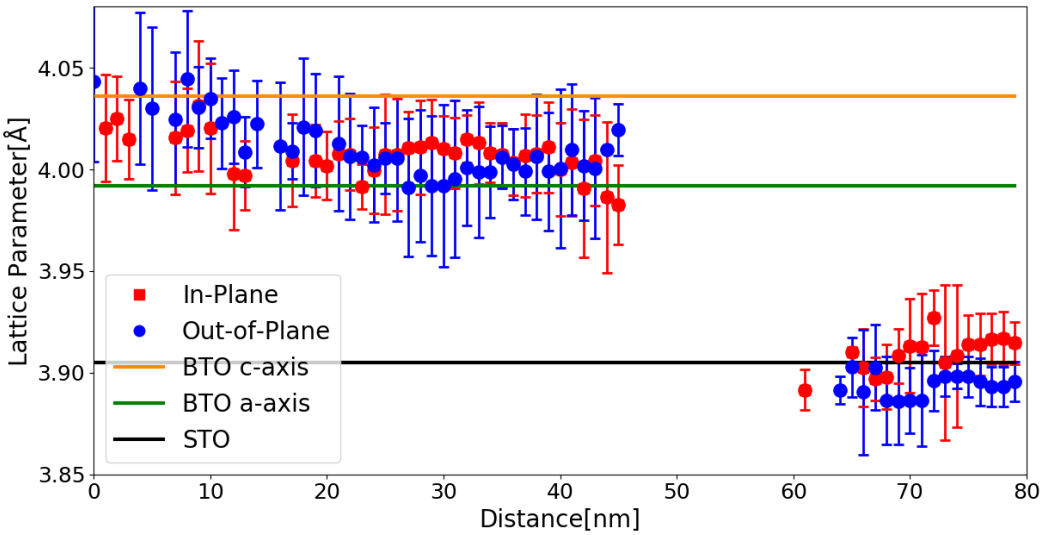

(d)

Figure A.2

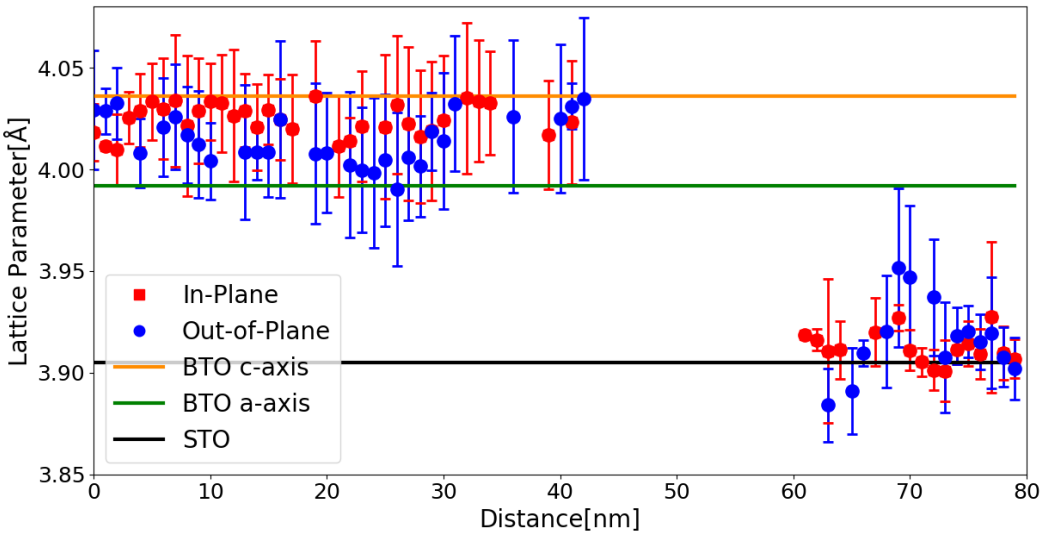
Lattice Parameter[Å]
Distance[nm]
In-Plane
Out-of-Plane
BTO c-axis
BTO a-axis
STO
4.05
4.00
3.95
3.90
3.85
0
10
20
30
40
50
60
70
80

(e)

Figure A.2

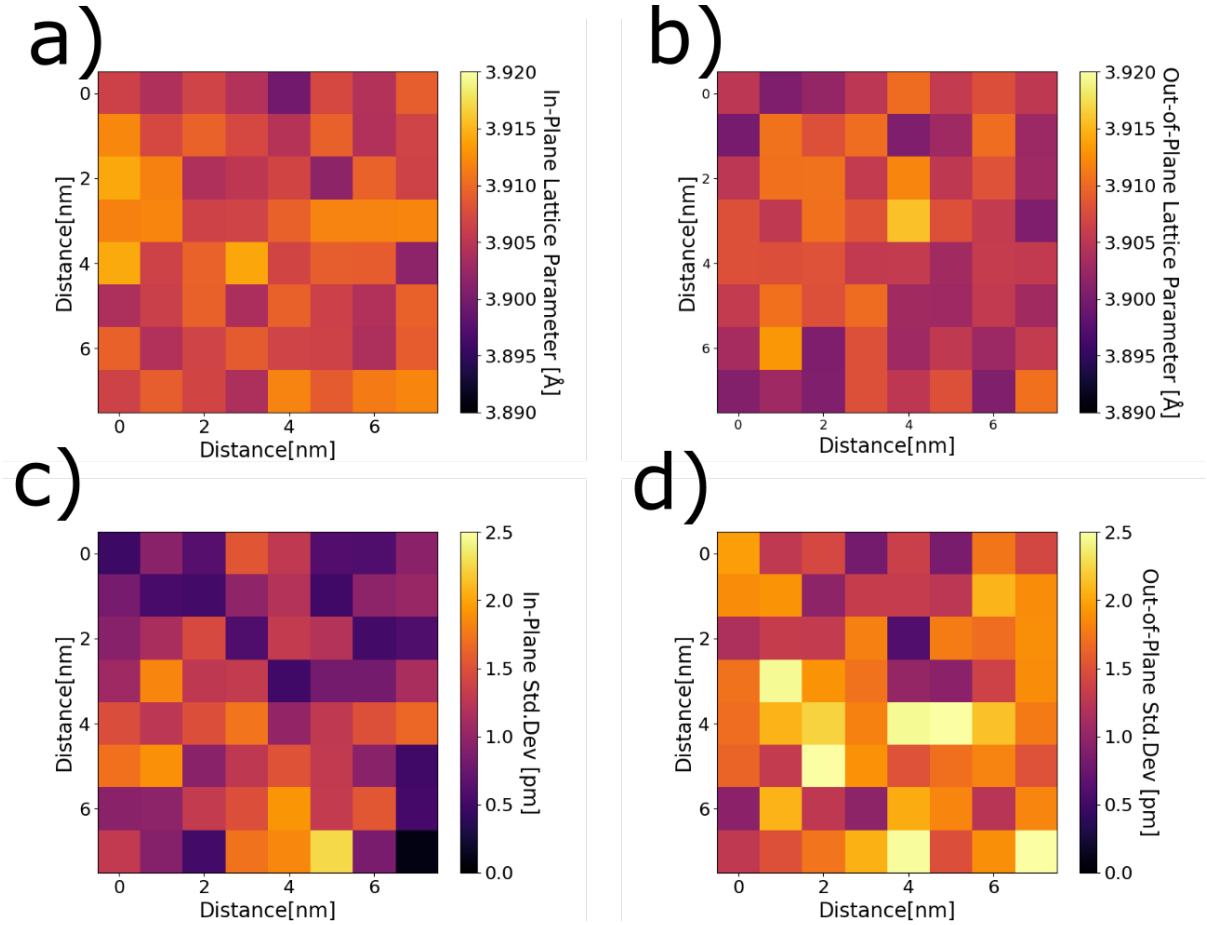

(a)

Figure A.3: The data generated from a 8 nm x 8 nm SCBED scan in the STO single crystal substrate is shown in each subfigure. a) and b) show maps of the in-plane and out-of-plane lattice parameters as measured by the algorithm, respectively. c) and d) show maps of the standard deviation associated with each lattice parameter measurement.

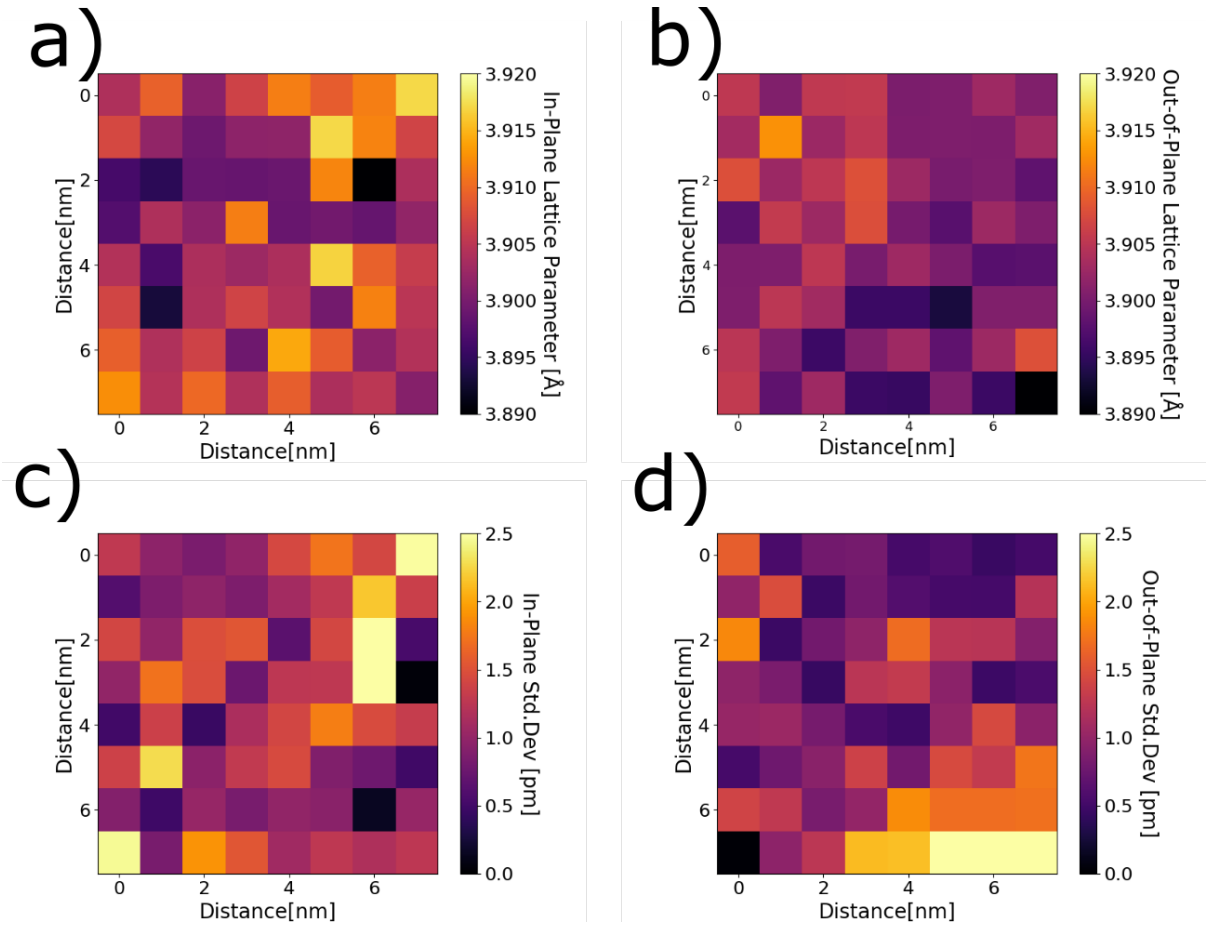
a)
b)
c)
d)
Distance[nm]
In-Plane Lattice Parameter [Å]
Out-of-Plane Lattice Parameter [Å]
In-Plane Std.Dev [pm]
Out-of-Plane Std.Dev [pm]

(b)

Figure A.3

B Digital Micrograph Scripts

Symmetry Quantification Script

```
// $BACKGROUND$

//The Above statement has to be included for the function ContinueBackgroundDialog to function

// Symmetry Quantification Program.

//This program takes a series of CBED images as input (stack) , and evaluates the symmetry of the CBED disc
//pattern along a chosen symmetry axis. The program does this by comparing CBED discs that lie on each side of a symmetry axis.
//The user is required to select the discs for comparison. The program then proceeds to evaluate the symmetries and produces symmetry maps,
//using the profile R and gamma factor to quantify symmetry.


//The functions written by Bernhard Schaffer can be found on the following website
//*****************************************************************************/
//*    Author: Bernhard Schaffer
//*    Date: 19.08.2015
//*    Availability: http://digitalmicrograph-scripting.tavernmaker.de/HowToScript_index.htm
//*
//*****************************************************************************/


//Function to Crop make Image out of ROI. Function Written by Bernhard Schaffer.
Image CropImageToSelection( Image img, string name)
{
  if ( !img.ImageIsValid() )
    Throw( "Invalid image in CropImageToSelection()" )
  number nDim = img.ImageGetNumDimensions()
  if ( 3 < nDim )
    Throw( "Dimensionality above 3D is not supported by CropImageToSelection()" )
  number sx, sy, t, l, b, r
  number sz=1, first, last
  img.GetSize(sx,sy)
  img.GetSelection(t,l,b,r)
  if ( 3 == nDIm )
  {
    sz = img.ImageGetDimensionSize(2)
    img.ImageGetImageDisplay(0).ImageDisplayGetDisplayedLayers(first,last)
    if ( first == last )
    {
      first = 0
      last = sz-1
    }

  }

  last++      // displayed slices use slice index, not limit
  l = max(0,min(l,sx))
  r = min(sx,max(r,0))
  t = max(0,min(t,sy))
  b = min(sy,max(b,0))
  first = max(0,min(first,sz))
  last  = min(sz,max(last ,0))
  if ( ! ( (l-r)&&(b-t)&&(first-last) ) )
    Throw( "Invalid cropping size in CropImageToSelection().\nCan not crop ["+l+","+t+","+first+";"+r+","+b+","+last+"]." )
  Image cut
  if ( (3 == nDim) && l<(last-first) )
    cut := img.Slice3(l,t,first,0,(r-l),1,1,(b-t),1,2,(last-first),1).ImageClone()
  else
    cut := img.Slice2(l,t,first,0,(r-l),1,1,(b-t),1).ImageClone()


  cut.SetName( img.GetName()+ "_" + name )

  return cut
}

//Function to display message while letting user select an ROI. Function written by Bernhard Schaffer.
Number ContinueBackgroundDialog(string message, number floating)
{
Number sema = NewSemaPhore()
If (floating) floatingModelessDialog(message,"continue",sema)
else ModelessDialog(message,"continue",sema)
Try GrabSemaphore(sema)
Catch return 0
return 1
}

//Function to convert a ROI to a mask. Function written by Bernhard Schaffer.
Image convert_ROItoMask(Image in)
{
ImageDisplay disp
Number nr_roi, count, size_x, size_y
ROI c_roi
Image mask
in.GetSize(size_x,size_y)
mask := IntegerImage("mask", 1, 0, size_x, size_y)
mask = 0
disp = in.ImageGetImageDisplay(0)
nr_roi = disp.ImageDisplayCountROIs()
For (count=0; count<nr_roi; count++)
{
c_roi = disp.ImageDisplayGetROI(count)
```

```
If (ImageDisplayIsROISelected(disp, c_roi)) c_roi.ROISetRegionToValue(mask, 1, 0, 0 , size_y, size_x)
}
return mask
}

// Function Gaussian Convolution can be found from the following website
//*****************************************************************************/
//*     Title: Canny Edge Filter
//*     Author: Mitchell, D.R.G. , Petersen, T.C.
//*     Date: 24.08.2013
//*     Code version: v1.1
//*     Availability: http://www.dmscripting.com/canny_edge_filter.html
//*
//*****************************************************************************/

//Creates a Gaussian Convolution of an Image
Image GaussianConvolution( image sourceimg, number standarddev)
  {
    // get the size of the source image. If it is not a power of 2 in dimension
    // warp it so that it is

    number xsize, ysize, div2size, expandx, expandy, logsize
    getsize(sourceimg, xsize, ysize)
    expandx=xsize
    expandy=ysize


    // Check the x axis for power of 2 dimension - if it is not, round up to the next size
    // eg if it is 257 pixels round it up to 512.

    logsize=log2(xsize)
    if(mod(logsize,1)!=0) logsize=logsize-mod(logsize,1)+1
    expandx=2**logsize


    // Check the y axis for power of 2 dimension - if it is not, round up to the next size
    // eg if it is 257 pixels round it up to 512.

    logsize=log2(ysize)
    if(mod(logsize,1)!=0) logsize=logsize-mod(logsize,1)+1
    expandy=2**logsize


    // Use the Warp function to stretch the image to fit into the revised dimensions

    image warpimg=realimage("",4,expandx, expandy)
    warpimg=warp(sourceimg, icol*xsize/expandx, irow*ysize/expandy)


    // Create the gaussian kernel using the same dimensions as the expanded image

    image kernelimg:=realimage("",4,expandx,expandy)
    number xmidpoint=xsize/2
    number ymidpoint=ysize/2
    kernelimg=1/(2*pi()*standarddev**2)*exp(-1*(((icol-xmidpoint)**2+(irow-ymidpoint)**2)/(2*standarddev**2)))


    // Carry out the convolution in Fourier space

    compleximage fftkernelimg:=realFFT(kernelimg)
    compleximage FFTSource:=realfft(warpimg)
    compleximage FFTProduct:=FFTSource*fftkernelimg.modulus().sqrt()
    realimage invFFT:=realIFFT(FFTProduct)


    // Warp the convoluted image back to the original size

    image filter=realimage("",4,xsize, ysize)
    filter=warp(invFFT,icol/xsize*expandx,irow/ysize*expandy)
    return filter
  }


// Dialogue boxes to find the size of the scan.
TagGroup DialogTG = DLGCreateDialog( "Number of scanning steps." )
TagGroup xField,xFieldItems
xField = DLGCreateBox("No. of X steps",xFieldItems)
TagGroup MyIntFieldx = DLGCreateIntegerField(3,5)
xFieldItems.DLGAddElement(MyIntFieldx)
DialogTG.DLGAddElement(xField)
TagGroup yField,yFieldItems
yField = DLGCreateBox("No. of Y steps",yFieldItems)
TagGroup MyIntFieldy = DLGCreateIntegerField(3,5)
yFieldItems.DLGAddElement(MyIntFieldy)
DialogTG.DLGAddElement(yField)
Object DialogOBJ = Alloc(UIFrame)
DialogOBJ.Init(DialogTG)
DialogObj.Pose()
// End of dialogue boxes

// Symmetry maps are created
Number ScanX, ScanY
ScanX = MyIntFieldx.DLGGetValue()
ScanY = MyIntFieldy.DLGGetValue()

Image SymMapGamma := RealImage("Gamma",4,ScanX,ScanY)
Image SymMapDistance := RealImage("C-Factor",4,ScanX,ScanY)

// Retrieves the scanning data-set and finds its dimensions
```

```
Number stackx, stacky, stackz
Image stack := GetFrontImage()
Get3DSize( stack , stackx, stacky, stackz)


// Below the user is asked to fit ROIs around the CBED discs of interest.

SetColorMode(stack, 4) // Sets the colour to temperature for easier selection of ROI
stack.ShowImage()

//Variables for storing disk positions
Number angle, x1, y1, x2, y2, x3, y3
Number x4, y4, x5, y5, x6, y6

//Images for storing selected disks
Image mask ,disk_c, disk_c2, disk_1, disk_2, disk_3, disk_4, disk_5, disk_6


//First the center disc is selected
ContinueBackgroundDialog("Please place an ROI around the 000 disc.",0)

disk_c = stack.CropImageToSelection("Disk_1")
disk_c2 = disk_c

// Select the surrounding discs
ContinueBackgroundDialog("You will now be asked to select 3 pairs of CBED discs."+\
             "Each pair should contain a disc and its symmetric disc." +\
             "Please draw the first ROI of the first pair.",0)
disk_1 = stack.CropImageToSelection("Disk_1")
mask = stack.convert_ROItoMask() //Convert the ROI to a mask
max(mask,x1,y1) //Find position of mask

//This selection process repeats for all the remaining discs.

ContinueBackgroundDialog("Draw the second ROI of the first pair.",0)
disk_2 = stack.CropImageToSelection("Disk_2")
mask = stack.convert_ROItoMask()
max(mask,x2,y2)

ContinueBackgroundDialog("Draw the first ROI of the second pair.",0)
disk_3 = stack.CropImageToSelection("Disk_3")
mask = stack.convert_ROItoMask()
max(mask,x3,y3)

ContinueBackgroundDialog("Draw the second ROI of the second pair.",0)
disk_4 = stack.CropImageToSelection("Disk_4")
mask = stack.convert_ROItoMask()
max(mask,x4,y4)

ContinueBackgroundDialog("Draw the first ROI of the third pair.",0)
disk_5 = stack.CropImageToSelection("Disk_5")
mask = stack.convert_ROItoMask()
max(mask,x5,y5)


ContinueBackgroundDialog("Draw the second ROI of the third pair.",0)
disk_6 = stack.CropImageToSelection("Disk_6")
mask = stack.convert_ROItoMask()
max(mask,x6,y6)

mask.DeleteImage()
// User selection of ROIs is now finished. ROI position have been stored in x,y variables.


//In the following the discs will be rotated, masked and flipped, to enable direct comparison.

// Finds angle needed for rotating mirror plane to the vertical axis
//The average of the angle between mirrored discs is used.
angle = (atan((y2 - y1) / (x2 - x1)) + atan((y4 - y3) / \
    (x4 - x3)) + atan((y6 - y5)/(x6 - x5))) / 3

//Variables to store the size of the discs before and after rotation.
number sx, sy, sz, sx2, sy2

// Store size before rotation
Get3DSize( disk_1, sx, sy, sz)

//Rotate and flip discs
disk_c := disk_c.Rotate(angle)
disk_c2 := disk_c2.Rotate(angle)
disk_c2.FlipHorizontal()

disk_1 := disk_1.Rotate(angle)
disk_2 := disk_2.Rotate(angle)
disk_2.FlipHorizontal()
disk_3 := disk_3.Rotate(angle)
disk_4 := disk_4.Rotate(angle)
disk_4.FlipHorizontal()
disk_5 := disk_5.Rotate(angle)
disk_6 := disk_6.Rotate(angle)
disk_6.FlipHorizontal()

// Update size values after rotation
Get3DSize( disk_1, sx2, sy2, sz )



//Radial mask is used to eliminate noise on the disc edges.

```

```
//Generate a radial mask for single images.
Image radialMaskSingle := IntegerImage("Radial Mask Single", 1, 0, sx2, sy2) = Tert(iradius < sx * 0.48, 1, 0)
//Generate a radial mask for stacks.
Image radialMask := IntegerImage("Radial Mask", 1, 0, sx2, sy2, sz) = Tert(iradius < sx * 0.48, 1, 0)
Number MaskPixels = sum(radialMask) / sz

//Apply a radial mask to all discs
disk_c = disk_c * radialMask
disk_c2 = disk_c2 * radialMask
disk_1 = disk_1 * radialMask
disk_2 = disk_2 * radialMask
disk_3 = disk_3 * radialMask
disk_4 = disk_4 * radialMask
disk_5 = disk_5 * radialMask
disk_6 = disk_6 * radialMask

////The discs have been processed and can be compared.


// The symmetry coefficients Gamma and C are calculated.

//Numbers for calculation of C
Number xmax, ymax

//Images and variables for calculation of R
Number numerator, denominator, R

Image img_numerator := RealImage("Numerator",4,sx2,sy2)
Image img_denominator := RealImage("Denominator",4,sx2,sy2)

Image slice_1 := RealImage("Slice",4,sx2,sy2)
Image slice_2 := RealImage("Slice",4,sx2,sy2)
Image slice_3 := RealImage("Slice",4,sx2,sy2)

//Images and variables for calculation of Gamma
Number gamma, mean_c, mean_1, mean_2, gamma_denominator_1, gamma_denominator_2, gamma_numerator

Image img_gamma_numerator := RealImage("Gamma_Numerator", 4, sx2, sy2)
Image img_gamma_denominator_1 := RealImage("Gamma_denominator_1", 4, sx2, sy2)
Image img_gamma_denominator_2 := RealImage("Gamma_denominator_2", 4, sx2, sy2)
result("\n Calculation Start \n")

//This loops calculates Gamma and C for all the images in the dataset

Number x,y //Indexes to keep track of position

for (number i=0 ; i<sz ; i++)
{
  x = i%ScanX
  y = floor(i/ScanX)
  result("\n x: "+ x + " y: " + y)

  //Calculation of C - metric

  //Select the center disc
  slice_1 = disk_c[icol,irow,i]
  //Do Gaussian Convolution
  slice_1 = GaussianConvolution(slice_1, 6)
  //Find maximum pixel position
  max(slice_1, xmax, ymax)

  //Store C-metric
  SymMapDistance[x,y] = 1 - Sqrt((xmax - sx2 / 2)**2 + (ymax - sy2 / 2)**2) / (sx / 2)


  //Calculation of Normalized Correlation Factor

  //In the following calculation we treat the all the images on one side of the symmetry
  //axis as if they were one image, comprised of the 3 images laid side by side


  // Mean intensity is calculated for one side of mirror plane
  slice_1 = disk_1[icol,irow,i]
  slice_2 = disk_3[icol,irow,i]
  slice_3 = disk_5[icol,irow,i]
  mean_1 = ((sum(slice_1) + sum(slice_2) + sum(slice_3)) / MaskPixels) / 3
  //Above we divide by mask pixels to find the mean, as that are the number of pixels that fall inside the mask

  // Mean intensity is calculated for other side of mirror plane
  slice_1 = disk_2[icol,irow,i]
  slice_2 = disk_4[icol,irow,i]
  slice_3 = disk_6[icol,irow,i]
  mean_2 = ((sum(slice_1) + sum(slice_2) + sum(slice_3)) / MaskPixels) / 3

  img_gamma_numerator = (disk_1[icol,irow,i] - mean_1) * (disk_2[icol,irow,i] - mean_2) +\
  (disk_3[icol,irow,i] - mean_1) * (disk_4[icol,irow,i] - mean_2)+\
  (disk_5[icol,irow,i] - mean_1)*(disk_6[icol,irow,i] - mean_2)

  gamma_numerator = sum(img_gamma_numerator*RadialMaskSingle)

  img_gamma_denominator_1 = (disk_1[icol,irow,i]-mean_1)*(disk_1[icol,irow,i]-mean_1) +\
  (disk_3[icol,irow,i]-mean_1)*(disk_3[icol,irow,i]-mean_1) +\
  (disk_5[icol,irow,i]-mean_1)*(disk_5[icol,irow,i]-mean_1)

  img_gamma_denominator_2 = (disk_2[icol,irow,i]-mean_2)*(disk_2[icol,irow,i]-mean_2) +\
  (disk_4[icol,irow,i]-mean_2)*(disk_4[icol,irow,i]-mean_2) +\
  (disk_6[icol,irow,i]-mean_2)*(disk_6[icol,irow,i]-mean_2)

  gamma_denominator_1 = sum(img_gamma_denominator_1*RadialMaskSingle)
```

```
  gamma_denominator_2 = sum(img_gamma_denominator_2*RadialMaskSingle)
  gamma=gamma_numerator/sqrt(gamma_denominator_1*gamma_denominator_2)

  //Normalized cross-correlation coefficient is stored
  SymMapGamma[x,y]=gamma


  //Now a condition to check whether the user wants to abort
  if ( ShiftDown() && ControlDown())
  {
    OKDialog(" Script aborted by user.")
    Exit( 0 )
  }

}

result("\n Calculation Stop \n")


//Display the Symmetry Maps
SetColorMode(SymMapGamma, 4)
SymMapGamma.ShowImage()
SetColorMode(SymMapDistance, 4)
SymMapDistance.ShowImage()
```

Listing 1: Program for quantification of symmetry in CBED patterns.

Lattice Parameter Measurement Algorithm

```
// $BACKGROUND$

//The Above statement has to be included for the function ContinueBackgroundDialog to work

// Lattice Parameter Algorithm

//This program finds the distances between CBED-disc to calculate lattice parameters.
//The program takes a stack of CBED patterns as input.
//Edge detection is performed on each pattern, and a template is created out of the center disc.
//The template is used for template matching, and the disc positions are found.
//The relevant inter-disc positions are identified and outputted with the standard deviation associated with the measurements.

//NB the program only finds inter-disc distances of the discs lie in a grid of vertical and horizontal lines.
// If that is not the case, rotate the pattern before starting the program.


//The functions written by Bernhard Schaffer can be found on the following website
//*****************************************************************************/
//*    Author: Bernhard Schaffer
//*    Date: 19.08.2015
//*    Availability: http://digitalmicrograph-scripting.tavernmaker.de/HowToScript_index.htm
//*
//*****************************************************************************/

//Function to display message while letting user select an ROI. Function written by Bernhard Schaffer.
Number ContinueBackgroundDialog(string message, number floating)
  {
  Number sema = NewSemaPhore()
  If (floating) floatingModelessDialog(message,"continue",sema)
  else ModelessDialog(message,"continue",sema)
  Try GrabSemaphore(sema)
  Catch return 0
  return 1
  }


//The functions GaussianConvolution, creategradientintensitymap,
//normaliseimageintensity and CannyEdge are based upon the work of D.R.G. Mitchell
//*****************************************************************************/
/*    Title: Canny Edge Filter
/*    Author: Mitchell, D.R.G. , Petersen, T.C.
/*    Date: 24.08.2013
/*    Code version: v1.1
/*    Availability: http://www.dmscripting.com/canny_edge_filter.html
/*
/*****************************************************************************/


// Applies a gaussian convolution to an image
Image GaussianConvolution( image sourceimg, number standarddev)
  {
    // get the size of the source image. If it is not a power of 2 in dimension
    // warp it so that it is

    number xsize, ysize, div2size, expandx, expandy, logsize
    getsize(sourceimg, xsize, ysize)
    expandx=xsize
    expandy=ysize

    // Check the x axis for power of 2 dimension - if it is not, round up to the next size
    // eg if it is 257 pixels round it up to 512.

    logsize=log2(xsize)
    if(mod(logsize,1)!=0) logsize=logsize-mod(logsize,1)+1
    expandx=2**logsize


```

```
    // Check the y axis for power of 2 dimension - if it is not, round up to the next size
    // eg if it is 257 pixels round it up to 512.

    logsize=log2(ysize)
    if(mod(logsize,1)!=0) logsize=logsize-mod(logsize,1)+1
    expandy=2**logsize


    // Use the Warp function to stretch the image to fit into the revised dimensions

    image warpimg=realimage("",4,expandx, expandy)
    warpimg=warp(sourceimg, icol*xsize/expandx, irow*ysize/expandy)


    // Create the gaussian kernel using the same dimensions as the expanded image

    image kernelimg:=realimage("",4,expandx,expandy)
    number xmidpoint=xsize/2
    number ymidpoint=ysize/2
    kernelimg=1/(2*pi()*standarddev**2)*exp(-1*(((icol-xmidpoint)**2+(irow-ymidpoint)**2)/(2*standarddev**2)))


    // Carry out the convolution in Fourier space

    compleximage fftkernelimg:=realFFT(kernelimg)
    compleximage FFTSource:=realfft(warpimg)
    compleximage FFTProduct:=FFTSource*fftkernelimg.modulus().sqrt()
    realimage invFFT:=realIFFT(FFTProduct)


    // Warp the convoluted image back to the original size

    image filter=realimage("",4,xsize, ysize)
    filter=warp(invFFT,icol/xsize*expandx,irow/ysize*expandy)
    return filter
  }

// Computes the directional gradients of an image
image creategradientintensitymap(image sourceimg)
  {

  // use the Sobel filter to compute the horizontal (dy) and vertical (dx) derivatives
  // use this again compute the horizontal (dydy) and vertical (dxdx) 2nd order and cross (dxdy) derivatives

  number scalex, scaley, xsize, ysize
  string unitstring
  getscale(sourceimg,scalex, scaley)
  getunitstring(sourceimg, unitstring)
  getsize(sourceimg, xsize, ysize)

  realimage edgegradient=exprsize(xsize,ysize,1)
  realimage edgedirection=exprsize(xsize,ysize,1)
  realimage dx=exprsize(xsize,ysize,1)
  realimage dy=exprsize(xsize,ysize,1)

  realimage dxdx=exprsize(xsize,ysize,1)
  realimage dydy=exprsize(xsize,ysize,1)
  realimage dxdy=exprsize(xsize,ysize,1)
  realimage dydx=exprsize(xsize,ysize,1)

  realimage cosbeta=exprsize(xsize,ysize,1)
  realimage sinbeta=exprsize(xsize,ysize,1)


  // compute the directions differences

  dx= offset(sourceimg,-1,-1) - offset(sourceimg,1,-1)  + \
    2*(offset(sourceimg,-1,0) - offset(sourceimg,1,0)) + \
    offset(sourceimg,-1,1) - offset(sourceimg,1,1)

  dy= offset(sourceimg,-1,-1) - offset(sourceimg,-1,1)  + \
    2*(offset(sourceimg,0,-1) - offset(sourceimg,0,1)) + \
    offset(sourceimg,1,-1) - offset(sourceimg,1,1)

  dxdx= offset(dx,-1,-1) - offset(dx,1,-1)  + \
  2*(offset(dx,-1,0) - offset(dx,1,0)) + \
    offset(dx,-1,1) - offset(dx,1,1)

  dydy= offset(dy,-1,-1) - offset(dy,-1,1)  + \
    2*(offset(dy,0,-1) - offset(dy,0,1)) + \
    offset(dy,1,-1) - offset(dy,1,1)

  dxdy= offset(dx,-1,-1) - offset(dx,-1,1)  + \
    2*(offset(dx,0,-1) - offset(dx,0,1)) + \
    offset(dx,1,-1) - offset(dx,1,1)


  // The gradient and directions images, defined by the eigendirections of the
    // Hessian matrix.  Ridge strength for elongated structures is 2nd order.

      sinbeta = (dxdy/(abs(dxdy)+1e-10)*sqrt(1.0/2*(1-(dxdx-dydy)/sqrt(1e-10+(dxdx-dydy)**2+4*dxdy**2))));
      cosbeta =                         sqrt(1.0/2*(1+(dxdx-dydy)/sqrt(1e-10+(dxdx-dydy)**2+4*dxdy**2)));

  number filtervalue= 1 //We force it to Sobel

  if(filtervalue==0) // use the Ridge detector
  {
    edgegradient = (dxdx+dydy)**2*((dxdx-dydy)**2+4*dxdy**2);
        //normalise by the mean to avoid very large gradient values:
```

```
        edgegradient/=average(edgegradient)+1e-10;
    edgedirection=atan(sinbeta/tert(abs(cosbeta)>1e-6,cosbeta,1e-6))+pi()/2;
      }
  else // The filter radio is set to Sobel
    {
      edgegradient=sqrt(dx**2+dy**2)
      edgedirection=atan2(dy, dx)
    }




// Convert the -3.142 to +3.142 image into degrees running 0 to 360 (easier to work with)

edgedirection=(edgedirection+pi())*(180/pi())


// round the edgedirectionimage up/down to 0, 45, 90, 135 degree angles.
// ie any point lying between 337.5 and 22.5 degs is rounded to 0 (angles
// run from 0 to 360 degrees

edgedirection=tert(edgedirection>337.5 || edgedirection<=22.5, 0, edgedirection)
edgedirection=tert(edgedirection>22.5 && edgedirection<=67.5, 45, edgedirection)
edgedirection=tert(edgedirection>67.5 && edgedirection<=112.5, 90, edgedirection)
edgedirection=tert(edgedirection>112.5 && edgedirection<=157.5, 135, edgedirection)

edgedirection=tert(edgedirection>157.5 && edgedirection<=202.5, 0, edgedirection)
edgedirection=tert(edgedirection>202.5 && edgedirection<=247.5, 45, edgedirection)
edgedirection=tert(edgedirection>247.5 && edgedirection<=292.5, 90, edgedirection)
edgedirection=tert(edgedirection>292.5 && edgedirection<=337.5, 135, edgedirection)

// update the progress bar in the dialog


// Create a thresholded image on the basis of the Sobel image - thresholded at the mean value
// then colour it according the direction

// define the colours for the various angles

rgbnumber red=rgb(255,0,0) // 0 degs
rgbnumber green=rgb(0,255,0) // 45 degs
rgbnumber blue=rgb(0,0,255) // 90 degs
rgbnumber yellow=rgb(255,255,0) // 134 degs


// Threshold the gradient image on the mean and then colour the threshold
// according to the direction. But if the Ridge detector is used, set the mean to zero

number edgemean=mean(edgegradient)
number filterradiovalue= 1
if(filterradiovalue==0) edgemean = 0


rgbimage thresholdimg:=rgbimage("",4,xsize, ysize)

thresholdimg=tert(edgegradient>=edgemean && edgedirection==0, red, thresholdimg) // 0 degs are red
thresholdimg=tert(edgegradient>=edgemean && edgedirection==45, green, thresholdimg) // 45 degs are green
thresholdimg=tert(edgegradient>=edgemean && edgedirection==90, blue, thresholdimg) // 90 degs are blue
thresholdimg=tert(edgegradient>=edgemean && edgedirection==135, yellow, thresholdimg) // 135 degs are yellow


// Do the non-maximum supression by testing to see if the magnitude of the gradient perpendicular to
// the direction of the line is less than that the line. If it is, the point is considered to lie
// on the line. If not, it is set to zero

image maxsupressimg:=binaryimage("",xsize, ysize)
maxsupressimg=tert(thresholdimg==red && edgegradient>offset(edgegradient,-1,0) && edgegradient>offset(edgegradient,1,0),1,maxsupressimg) // red=0 degs Nrth/Sth
maxsupressimg=tert(thresholdimg==green && edgegradient>offset(edgegradient,-1,-1) && edgegradient>offset(edgegradient,1,1),1,maxsupressimg) // green =45 degs NE/SW
maxsupressimg=tert(thresholdimg==blue && edgegradient>offset(edgegradient,0,-1) && edgegradient>offset(edgegradient,0,1),1,maxsupressimg) // blue = 90 degs E/W
maxsupressimg=tert(thresholdimg==yellow && edgegradient>offset(edgegradient,1,-1) && edgegradient>offset(edgegradient,-1,1),1,maxsupressimg) // yellow =135 degs NW/SE



// Use the binary image created above to extract the equivalent gradient image
// This has the same form as the binary maxsuppressimg, but the values of 1 are exchanged for the actual
// gradient values

maxsupressimg:=maxsupressimg*edgegradient


// Update the dialog progress bar to show the task has completed.


return maxsupressimg
}

// Function to normalise the intensity of the passed in image, so that
// its intensities run from 0 to the value shown in normalisation
image normaliseimageintensity(image displayimage, number normalisation)
  {
    image temp=imageclone(displayimage)
    number minval, maxval
    minmax(temp, minval, maxval)

```

```
    temp=temp-minval
    temp=temp/(maxval-minval)
    temp=temp*normalisation
    return temp
  }

// Combines the previous functions to give a canny edge detector.
image CannyEdge( Image img, number sigma, number normalisationfactor, number eflag,number upthresholdval)
  {
  result("\nCanny Edge Filter Calculations Started.\n")

  number size_x, size_y
  Getsize(img, size_x, size_y)

  img = GaussianConvolution(img, sigma)

  Image intensitygradientimage = creategradientintensitymap(img)

  // normalise the image to 100 so that threshold values are between 0 and 100

  intensitygradientimage = normaliseimageintensity(intensitygradientimage, normalisationfactor)

  // Threshold the edge intensity gradient image so that anything above the upper threshold is 100
  // these are the strong edges

  // This is raising pixels over uppertresholdval to 100

  //Pixels over a treshold are raised to eflag. The treshold value decreases when moving away from the image center.
  //This is done because edges have smaller gradients further away from the center of the diffraction pattern
  Image upperthreshold = tert(intensitygradientimage> upthresholdval*(1-iradius/size_x),eflag,0)

  result("Canny Edge Calculations Finished.\n")

  return upperthreshold
  }

// The functions butterworthfilter and CrossCorrROI are based the work of D.R.G. Mitchell:
//*******************************************************************************/
//*    Title: Cross Correlate ROI with Image
//*    Author: Mitchell, D.R.G.
//*    Date: 11.06.2016
//*    Code version: v1.1
//*    Availability: http://www.dmscripting.com/cross_correlate_roi_with_image.html
//*
//*******************************************************************************/


// Function to create a butterworth filter. Imgxsize and imgysize are the sizes of the filter image
// bworthorder is a numerical value (1-6 is good), which defines the rate at which the edge of the filter
// decays to zero. Low values give shallow slopes. zeroradius specifies the radius of the filter.
// Two radial filters have been added, to remove all edges which are not of interest in the template matching.
image butterworthfilter(number imgxsize, number imgysize, number bworthorder, number zeroradius)
  {
    // See John Russ Image Processing Handbook, 2nd Edn, p 31

    image butterworthimg=realimage("",4,imgxsize, imgysize)
    Image radialMask:= IntegerImage("Radial Mask",1,0,imgxsize,imgysize)= Tert(iradius<zeroradius*0.90,0,1)
    Image radialMask2:= IntegerImage("Radial Mask",1,0,imgxsize,imgysize)= Tert(iradius<zeroradius*1.1,1,0)
    butterworthimg=0

    // note the halfpointconst value sets the value of the filter at the halfway point
    // ie where the radius = zeroradius. A value of 0.414 sets this value to 0.5
    // a value of 1 sets this point to root(2)

    number halfpointconst=0.414
    butterworthimg=1/(1+halfpointconst*(iradius/zeroradius)**(2*bworthorder))

    return butterworthimg*radialMask*radialMask2
  }


number clipnegativevalues =1 // Set this to 0 (no) or 1 (yes) to clip out all negative values from the final image


//A motif is made out of the center-disc and is cross-correlated with the image.
//The output is a cross correlation map.

//front: Input Image. This is a CBED pattern after Canny edge detection.
//bwfilter: A filter to create the desired motif
//offsetx,offsety: Holds the position of the 000 disc, which is to be used as a motif.

Image CrossCorrROI( Image front, Image bwfilter, number offsetx, number offsety)
  {

  image markup = imageclone(front)*0
  markup = offset(front, offsetx, offsety)

  number minoffset, maxoffset
  minmax(markup, minoffset, maxoffset)
  markup=(markup-minoffset)/(maxoffset-minoffset)

  // Create a motif image and cross correlate it with the original image
  image motif = bwfilter*markup

  image frontscale = imageclone(front)
  number frontmin, frontmax
  minmax(frontscale, frontmin, frontmax)
  frontscale=(frontscale-frontmin)/(frontmax-frontmin) // Normalize image

```

```
  image crosscorr = crosscorrelate(motif, frontscale) // crosscorrelate motif with image

  imagecopycalibrationfrom(crosscorr, front)
  taggroup fronttags=front.imagegettaggroup()
  taggroup cctags=crosscorr.imagegettaggroup()
  taggroupcopytagsfrom(cctags, fronttags)

  // Rotate the image and display in temperature colour

  crosscorr=rotate(crosscorr, pi()) // the cross correlation is rotated with respect to the original

  if(clipnegativevalues!=0) crosscorr=tert(crosscorr<0,0,crosscorr) // clip out negatives if the flag is set to 1

  front.deleteImage()

  return crosscorr
  }


// Function that outputs the positions of local maxima of a cross-correlation map.
// The output is an image that contains the positions of a selection of local maxima.
// The positions are ordered such that the highest maxima is stored first, then the next-highest etc.

// img: Input Image, Cross-Correlation Map. Output of CrossCorrROI
// no_maxima: determines how many maxima will be stored
// limit: determines the threshold below which we do not store maxima
// radius: determines the radius around each maxima we mask.
//        This is done as we know we do not expect local maxima close to each other than radius
image Find_Maxima( Image img, number no_maxima, number limit, number radius)
{

  number size_x,size_y

  GetSize(img, size_x, size_y)

  // Images to store the maxima values and coordinates.
  Image MaximaValue:= RealImage("Maxima_Values",4,1,no_maxima)
  Image MaximaCoord:= RealImage("Maxima_Coord",4,2,no_maxima)

  number pos_x, pos_y // Temporarily holds the maxima positions
  number max_val= max(img,pos_x,pos_y) //Find the first maxima, likely the 000 disc.

  //Apply a mask to the image to filter out the outer edges.
  Image EdgeMask = IntegerImage("EdgeMask",1,0,size_x,size_y)= \
           Tert( (icol - pos_x)**2 + (irow - pos_y)**2 < (size_x / 4)**2 ,1,0)
  img=img*EdgeMask

  number counter=0  //Counts the number of local maxima found

  // The loop iterates as long as the maxima have a certain magnitude
  while(max_val > limit && counter < no_maxima)
  {
    MaximaValue.SetPixel(0,counter,max_val)
    MaximaCoord.SetPixel(0,counter,pos_x)
    MaximaCoord.SetPixel(1,counter,pos_y)
    counter=counter+1

    //Now create a mask around the selected maxima
    EdgeMask= Tert( (icol-pos_x)**2+(irow-pos_y)**2 > radius**2 ,1,0)
    img= img*EdgeMask

    //Find new maxima
    max_val= max(img,pos_x,pos_y)

    //A condition to check whether the user wants to abort
    if ( ShiftDown() && ControlDown())
    { OKDialog(" Script aborted by user.")
    Exit( 0 )
    }
  }

  result(" \n " + " Number of Maxima found : " + counter + "\n")

  return MaximaCoord
}



//Takes a list of positions as input, finds the nearest neighbour distances between points.
// Sorts the distances in horizontal and vertical distances.
// Calculates the averages and std.dev. of the horizontal and vertical distances
// Outputs the data in a 2x2 image.

//List: sorted list of maxima coordinates from a cross correlation image. Output of Find_Maxima
//no_lengths: maximal number of inter-maxima distances stored

Image FindLengths(Image List, Number no_lengths)
{
  //Note that this function only finds inter-maxima distances which are roughly
  //vertical or horizontal.

  number size_x, no_maxima
  GetSize(List, size_x, no_maxima)

  Image xlengths:= RealImage("xlengths",4,1,no_lengths)  //Stores all horizontal lengths
  Image ylengths:= RealImage("ylengths",4,1,no_lengths)  //Stores all vertical lengths


  // The number of distances found and the sum of the distances is stored for calculation of the average
```

```
number x_counter = 0
number y_counter = 0
number x_sum = 0
number y_sum = 0

number distance, deltax, deltay // temporarily stores the distance between two maxima
number pos_x, pos_y, pos_x2, pos_y2  // temporarily stores positions of maxima


//We first find the shortest vertical or horizontal inter-maxima distance
number Find_Shortest_Distance=0
number min_distance = 99999999 // Will be chosen as smallest distance inbetween spots. Large intital value to it will be replaced


// Each inter-maxima distance makes an angle given by the ratio deltay/deltax.
// By checking the angles of each distance we can distinguish between approximately horizontal and vertical distances.
// We therefore define the tan values which give the upper and lower bounds for the
// ratio of deltay to deltax. That is deltay/deltax should be lower than lower Tan or larger than uppertan for the distance to be stored.

number upperTan = tan(85/180 * pi())**2
number lowerTan = tan(5/180 * pi())**2

//This loop finds the shortest distance that satifies the given constraints.

// Retrieve the first maxima position. This corresponds to the 000 disc position.
pos_x = List.GetPixel(0,0)
pos_y = List.GetPixel(1,0)

//Iterate through all the other maxima to find smallest inter-maxima distance.
//This is needed to impose the proper constraints on inter-maxima distances
for (number j=1; j< no_maxima; j++)
{
  pos_x2 = List.GetPixel(0,j)
  pos_y2 = List.GetPixel(1,j)

  if (pos_x2*pos_y2 > 0 ) // Check that it is a valid entry
  {
    deltax = (pos_x - pos_x2)**2
    deltay = (pos_y-pos_y2)**2

    if (lowerTan > deltay/deltax || upperTan < deltay/deltax) // Check that it is aligned horizontally or verictally with respect to center
    spot
    {
      distance = deltax + deltay
      if (distance < min_distance)
      {
        min_distance = distance
      }
    }
  }
}

// Define the maximum distance the spots can be separated by.
// This is done so we do not count spots that are 2 reflections away

number max_distance = 1.2**2 * min_distance

// This loop finds all inter-maxima distances that satifies the given constraints,
for (number i=0; i< no_maxima; i++)
{
  pos_x = List.GetPixel(0,i)
  pos_y = List.GetPixel(1,i)

  for (number j=i+1; j< no_maxima; j++)
  {
    pos_x2 = List.GetPixel(0,j)
    pos_y2 = List.GetPixel(1,j)

    if (pos_x2*pos_y2 > 0) // check if valid position
    {
      deltax = (pos_x - pos_x2)**2
      deltay = (pos_y-pos_y2)**2
      distance = deltax + deltay


      //Now a condition to check whether the user wants to abort
      if ( ShiftDown() && ControlDown())
      {
        OKDialog(" Script aborted by user.")
        Exit( 0 )
      }


      if (distance < max_distance )//Check to see if they are close enough , and not obvious outlier
      {
        if (lowerTan > deltay/deltax) // Then this is an x-distance because it lies in the right angle
        {
          xlengths.SetPixel(0,x_counter,sqrt(distance))

          x_counter = x_counter+1

          x_sum= sqrt(distance) + x_sum
        }
        else if(upperTan < deltay/deltax)  // it is a y-distance
        {
          ylengths.SetPixel(0,y_counter,sqrt(distance))

          y_counter = y_counter+1

```

```
            y_sum = sqrt(distance) + y_sum
          }
        }
      }
    }
  }

  //Calculate the average distance
  number x_average = x_sum / x_counter
  number  y_average = y_sum / y_counter

  //Calculate the standard deviation

  //These are used to hold sums
  number temp_x = 0
  number temp_y = 0
  number temp_x2
  number temp_y2
  //
  for (number i=0; i< no_lengths; i++)
  {
    temp_x2 = xlengths.GetPixel(0,i)
    if ( temp_x2 != 0)
    {
      temp_x = (xlengths.GetPixel(0,i) - x_average)**2 + temp_x
    }

    temp_y2 = ylengths.GetPixel(0,i)
    if ( temp_y2 != 0)
    {
      temp_y = (ylengths.GetPixel(0,i) - y_average)**2 + temp_y
    }
  }

  number x_deviation = sqrt(temp_x / (x_counter - 1))
  number y_deviation = sqrt(temp_y / (y_counter - 1))

  result("X Average :" + x_average + "  X std.av : " + x_deviation + "\n")
  result("Y Average :" + y_average + "  Y std.av : " + y_deviation + "\n")


  Image output:= RealImage("output",4,2,2)

  output.Setpixel(0,0,x_average)
  output.Setpixel(1,0,y_average)
  output.Setpixel(0,1,x_deviation)
  output.Setpixel(1,1,y_deviation)

  return output
}


result("\nProgram Start\n")

//Finds number of Images to process and the x length
TagGroup DialogTG = DLGCreateDialog( "Number of scanning steps." )
TagGroup xField,xFieldItems
xField = DLGCreateBox("No. of X steps",xFieldItems)
TagGroup MyIntFieldx = DLGCreateIntegerField(3,5)
xFieldItems.DLGAddElement(MyIntFieldx)
DialogTG.DLGAddElement(xField)
TagGroup yField,yFieldItems
yField = DLGCreateBox("No. of Y steps",yFieldItems)
TagGroup MyIntFieldy = DLGCreateIntegerField(3,5)
yFieldItems.DLGAddElement(MyIntFieldy)
DialogTG.DLGAddElement(yField)
Object DialogOBJ = Alloc(UIFrame)
DialogOBJ.Init(DialogTG)
DialogObj.Pose()
//// End of dialogue boxes

Number dimx, dimy
dimx = MyIntFieldx.DLGGetValue()
dimy = MyIntFieldy.DLGGetValue()
number x,y //keep track of the indices in the data-set


Image stack := GetFrontImage()

number stackx, stacky, stackz

Get3DSize( stack , stackx, stacky, stackz)

Image img := RealImage("img", 4, stackx, stacky)


Image Output:= RealImage("Output_data",4, dimx,dimy,4) //Stores Output data
Image tempOutput:=RealImage("Output_data",4, 2, 2) // Temporary stores output data
Number x_av, y_av, x_d, y_d // Temporary Storage for output values

// EdgeDetection

number sigma = 3

number normalisationfactor = 100

number eflag = 100

number upthresholdval = 5
```

```
657
658 //CrossCorrelation Parameters
659 Image front
660 Image bwfilter          // Filter for template
661 number offsetx,offsety  // Template position
662
663
664 // Length Calculation Parameters
665
666 number limit = 0.019 // Maximum treshold
667
668 number no_maxima = 25 // Number of maxima stored
669
670 number radius = 150 // minimum inter-maxima distance
671
672 number no_lengths = 50 // Number of inter-maxima lengths stored
673
674
675 //Loop over all images in stack
676 for( number k = 0; k < stackz; k++)
677 {
678   x = k % dimx
679   y = floor(k / dimx)
680
681   result("\n" + "Calculation of x: " + x + "   y:" + y + " \n")
682   img= stack[icol,irow,k]
683
684   //Edge Detection
685   img= CannyEdge(img, sigma, normalisationfactor, eflag, upthresholdval)
686
687   // Finds template position, creates template filter
688   if (k==0)
689   {
690     front= img
691     front.ShowImage()
692
693     ContinueBackgroundDialog(" Select the center 000 disc with an ROI.", 0)
694
695     // Check that an ROI is present on the image
696
697     imagedisplay frontdisp=front.imagegetimagedisplay(0)
698     number norois=frontdisp.imagedisplaycountrois()
699     if(norois<1)
700       {
701         showalert("Ensure a square ROI defines a region of typical structure.",2)
702         exit(0)
703       }
704     image roi:=getfrontimage()[]
705
706
707     //Get information from the ROI
708
709     roi theroi=frontdisp.imagedisplaygetroi(0)
710     number roit, roil, roib, roir
711     theroi.roigetrectangle(roit, roil, roib, roir)
712     number roicntrx=((roir-roil)/2)+roil
713     number roicntry=((roib-roit)/2)+roit
714
715     number imgx, imgy, roix, roiy
716     getsize(front, imgx, imgy)
717     getsize(roi, roix, roiy)
718
719     number imgcntrx=imgx/2
720     number imgcntry=imgy/2
721
722     //Offset the template so it is centered in an image
723
724     offsetx=roicntrx-imgcntrx
725     offsety=roicntry-imgcntry
726
727     // Create a butterworth mask for the above image
728
729     number butterworthorder=6 // values between 1 and 6 are sensible. 1 produces a very gentle slope to the
730     // feathering at the edge of the butterworth filter. 3 is a fairly steep roll off and 6 is a very abrupt edge
731
732     number roixradius=(roir-roil)/2
733     number roiyradius=(roib-roit)/2
734     number zeroradius=min(roixradius, roiyradius)
735     bwfilter=butterworthfilter(imgx, imgy,  butterworthorder,  zeroradius)
736
737     front.DeleteImage()
738   }
739
740   //Cross-Correlation
741   img = CrossCorrROI(img, bwfilter, offsetx, offsety)
742
743   //Maxima are identified
744   Image Sorted_Coord_List=Find_Maxima( img, no_maxima, limit, radius)
745
746   //Intermaxima distances calculated
747   tempOutput=FindLengths( Sorted_Coord_List, no_lengths)
748
749   //Distances and std. deviations stored
750   x_av = tempOutput.GetPixel(0,0)
751   y_av = tempOutput.GetPixel(1,0)
752   x_d = tempOutput.GetPixel(0,1)
753   y_d = tempOutput.GetPixel(1,1)
754
755   Output[x,y,0] = x_av
```

```
  Output[x,y,1] = y_av
  Output[x,y,2] = x_d
  Output[x,y,3] = y_d

  //Now a condition to check whether the user wants to abort
  if ( ShiftDown() && ControlDown())
  {
    OKDialog(" Script aborted by user.")
    Exit( 0 )
  }

}


Output.ShowImage()

result("\n" + "Script succesfully terminated" + "\n")
```

Listing 2: Program for measuring the inter-disc distances in CBED patterns.

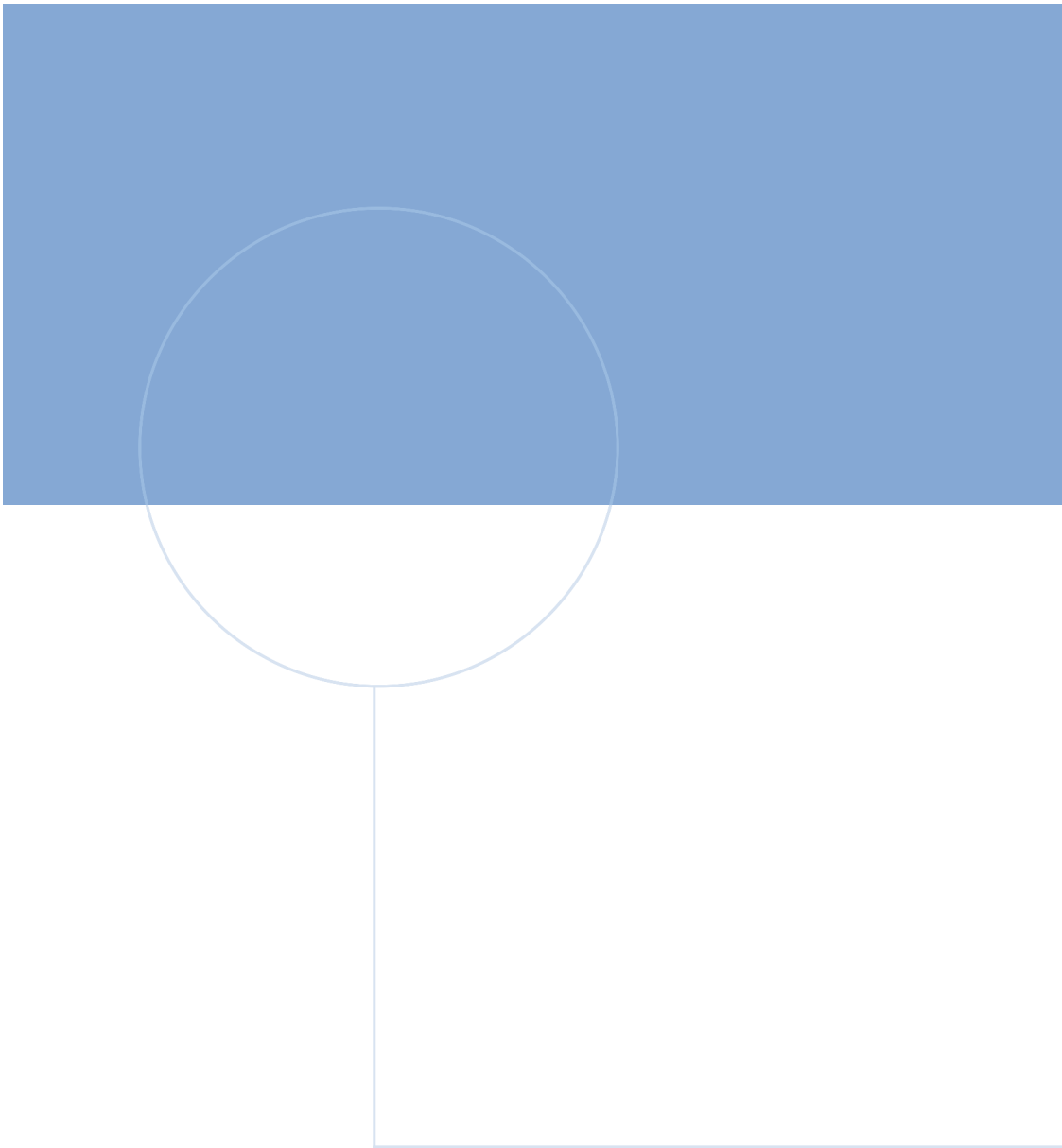

NTNU
Norwegian University of
Science and Technology